A contribution to nonlinear control of floating wind turbines

Cheng Zhang

THÈSE DE DOCTORAT DE

L'ÉCOLE CENTRALE DE NANTES

ÉCOLE DOCTORALE N° 601
Mathématiques et Sciences et Technologies de l'Information et de la Communication
Spécialité : *Automatique, Productique et Robotique*

Par

Cheng Zhang

A contribution to nonlinear control of floating wind turbines

Soutenance de thèse prévue à Nantes, le 9 Février, 2021
Unité de recherche : Le Laboratoire des Sciences du Numérique de Nantes (LS2N)
Thèse N° :

Rapporteurs avant soutenance :

Salah LAGHROUCHE	Maître de Conférences-HDR, UTBM, Belfort, France
Nacer K. M'SIRDI	Professeur des universités, Aix-Marseille Université, Marseille, France

Composition du Jury :
Attention, en cas d'absence d'un des membres du Jury le jour de la soutenance, la composition du jury doit être revue pour s'assurer qu'elle est conforme et devra être répercutée sur la couverture de thèse

Président :		
Examinateurs :	Xavier Brun	Professeur des universités, INSA de Lyon, Lyon, France
	Carolina EVANGELISTA	*Profesor Adjunto*, Universidad Nacional de La Plata, La Plata, Argentine
	Jean-christophe GILLOTEAUX	Ingénieur de recherche, École Centrale de Nantes, Nantes, France
	Salah LAGHROUCHE	Maître de conférences-HDR, UTBM, Belfort, France
	Nacer K. M'SIRDI	Professeur des universités, Aix-Marseille Université, Marseille, France
	Franck PLESTAN	Professeur des universités, École Centrale de Nantes, Nantes, France
Invité :	Sofien KERKENI	CEO, D-ICE Engineering, Nantes, France
Dir. de thèse :	Franck PLESTAN	Professeur des universités, École Centrale de Nantes, Nantes, France

ACKNOWLEDGEMENT

Table of Contents

List of Figures

List of Tables

General Introduction

Contents

In modern society, the development of industry and the daily life of residents are inseparable from energy. Coal, petroleum and other fossil energy sources have provided impetus for human development. However, the problems of energy crisis and environment pollution become now serious. On the one hand, the fossil energy sources are limited but human development requires more and more energy, and fossil energy resources will be exhausted someday in the near future; on the other hand, the overuse of fossil resources aggravates the emission of carbon dioxide and other toxic greenhouse gases, causing serious environment problem (Tiwari and Babu 2016). According to the report of International Energy Agency (IEA 2019a), driven by the increase in energy request in 2018, global energy-related carbon dioxide emission, reach a record high of 33.1 Gt of carbon dioxide that is one of the main contributors to greenhouse gases. Although the emissions of all fossil fuels have increased, the increase in emissions due to power sector accounts for nearly two-thirds. In order to tackle with the shortage of fossil energy and the environment problems cause by the greenhouse gases, it is imperative to switch to other means of power productions. Renewable energies such as solar, hydro and wind electricity are theoretically inexhaustible and environmental friendly. For these reasons, they have been quickly promoted and widely used all over the world.

Among those renewable energy solutions, the wind energy plays a leading role in providing clean energy, and has made great progress in the past 20 years. By 2019, the installed capacity of global wind turbines have been reached 651 gigawatt (GW). Nevertheless, some problems emerge; for example, large wind farms on the land induce visual, noise pollution, and the installation spaces are inadequate. On the other hand, offshore wind turbines limit these problems; as a consequence, researchers pay more and more attention to this class of wind turbines. Among the possible solutions, one can cite the offshore floating wind turbines (FWT): such turbines can be installed in deeper

waters with floating foundations, allowing to make use of the strong wind and the plenty of space in oceans.

However, huge progress must be made on this class of wind turbines, especially on their control. This is the main reason of this thesis. This chapter introduces the wind turbines, including the traditional onshore wind turbines, offshore wind turbines, especially the floating ones. The chapter also displays the wind turbines control systems and proposes a review of controllers. Finally, the research motivations and organizations of this thesis are outlined.

Introduction of wind systems

The development of wind energy

Wind turbine is the product of modern science and technology. It is a power generation equipment that uses natural wind energy to firstly convert the kinetic energy of wind into mechanical energy. Then, the turbine driving the generator, power generation is possible. As a kind of clean, renewable and sustainable energy, wind energy plays an important role for the global power supply system and becomes the fastest increasing new clean electric power. In 2019, new installed capacity exceeded the 60 GW milestone for the second time in history, that is +19% compared with 2018 (see Figure 1). Table 1 is listing the top 5 countries of installed wind power capacity by 2019.

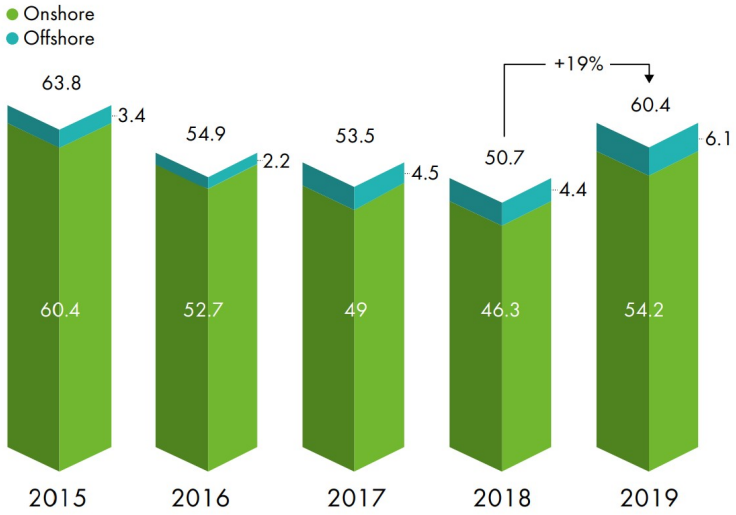

Figure 1 – New installations of wind energy (GWEC 2019).

Country	Installed capacity (MW)
China	237,029
United States	105,433
Germany	61,357
India	37,529
Spain	25,808

Table 1 – Installed capacities for the top 5 countries by the end of 2019 (*Wind Energy International* 2020).

Offshore wind energy

Although the majority of the wind turbines are installed onshore, the offshore wind market is growing rapidly (about 30% per year) since 2010 thanks to the development of technology. For example, in 2019, 6.1 GW (a record) of offshore wind energy has been installed (see Figure 1). The fast development of offshore wind energy is due to the fact that (H. Namik and K. Stol 2013; Olondriz Erdozain 2019):

- the quality of offshore wind resource is better: less turbulence and higher annual mean wind speed. Then, smaller structure load and higher power generation can be achieved;
- the lack of space for onshore wind turbines being a reality in numerous countries, the offshore area provides additional space;
- offshore solutions induce reduced visual and noise impact.

In the next five years, about 150 new offshore wind projects are expected to be completed all over the world, pointing to an increasing role for offshore wind in power supplies. Many european countries stimulate the development of this technology, among them United Kingdom, Germany and Denmark. The United Kingdom and Germany currently have the largest offshore wind capacities in operation, while Denmark produces 15% of its electricity from offshore wind in 2018. China added more capacity than any other country in 2018 (IEA 2019b).

Overview of floating wind turbine

Offshore wind energy has a great potential and is expected in the future to have a greater portion of the global energy mix. However, 80% of offshore wind resources are in the deep water zones (deeper than 60 m). In order to use these resources, floating wind turbines are the solutions.

The concept of floating wind turbine (FWT) was firstly proposed in (Heronemus 1972): this concept allows to generate electricity in the deep water zones thanks to floating structures that supports the wind turbines. However, since the establishment of commercial wind power industry in the mid 1990's, the topic of FWT has gradually got attention from the research community (Musial, Butterfield, and Boone 2004). Based on the floating technologies derived from oil & gas industry, FWT could imagine using the abundant oceanic wind energy resources.

Current contributions of floating wind systems versus all the wind installations is fairly small, but it will play an increasingly important role toward the end of this decade, accounting for 6 percent of global new wind installations in 2030 (GWEC 2020). Europe has the most developed FWT technologies and has a great potential for the floating wind market (WindEurope 2017). Furthermore, european companies lead three quarters of the floating wind projects, with more than fifty FWT projects all over the world. Numerous of pre-commercial FWT projects (see Table 2) are now announced and will be in operation in the next few years.

Wind farm name	Country	Capacity (MW)	Commissioning date
Windfloat Atlantic	Portugal	25	2019
Flocan 5 Canary	Spain	25	2020
Nautilus	Spain	5	2020
SeaTwirl S2	Sweden	1	2020
Kincardine	United Kingdom	49	2020
Forthwind Project	United Kingdom	12	2020
EFGL	France	24	2021
Groix-Belle-Ile	France	24	2021
PGL Wind Farm	France	24	2021
EolMed	France	25	2021
Katanes Floating Energy Park -Array	United Kingdom	32	2022
Hywind Tampen	Norway	88	2022

Table 2 – Announced pre-commercial FWT projects in Europe (WindEurope 2018).

Notice that, despite Europe's largest seafront, France is lagging far behind in the development of FWTs. This thesis wanted to contribute to the catching up of this delay.

There are four main floating structures currently applied to the FWT systems (*Wind Energy International* 2020): barge, semi-submersible (semi-sub), spar-buoy (spar) and tension leg platform (TLP) as shown in Figure 2. They are classified by the principles of stabilization mechanisms in the water; a brief introduction of the four platforms is given in the sequel (Si 2015; Hazim Namik 2012; Olondriz Erdozain 2019; Scheu et al. 2018)

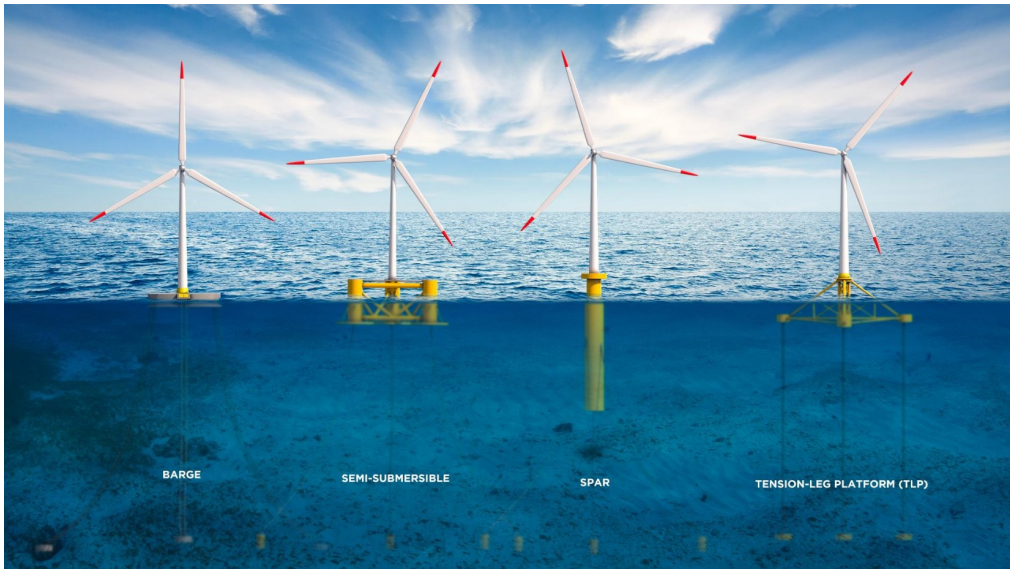

Figure 2 – The four main floating wind turbine concepts (WindEurope 2017).

- **Barge structure:** the barge platform is stabilized mainly by a water-plane area, that is a mechanical structure similar to a ship. Such platform usually has a large area with a shallow draft that gives the minimum water depth requirement. Mooring lines are necessary to maintain the platform at a given spot and prevent the drift displacement. Moreover, moon pool or heave plates can equipped the barge platform in order to increase the damping and reduce the platform motions (Scheu et al. 2018);

- **Semi-submersible (semi-sub) structure:** the semi-sub platform is stabilized by the combination of ballast and water-plane area. The ballast diameters, their distances from each other, the draft and the mass of the structure, affect the stability of the platform. Therefore, the motions of the platform can be adjusted by those parameters. Mooring system is also required to keep the platform at a given position;

- **Spar-buoy (spar) structure:** the spar-buoy platform is stabilized by a ballast, with a lower center of mass lower than the center of buoyancy. Thanks to such structure, a restore moment can be generated so that the stability of the platform is kept from the heeling moment. The platform is moored by catenaries (normally, 3 mooring lines), ensuring that the platform is in a fixed position and without drift displacement. This type of platform can be used in very deep sea water areas;

- **Tension leg platform (TPL) structure:** the TLP structure is stabilized by tension moor-

ing lines that are fixed to the seabed; the tension is generated by the large buoyancy of the floating structure. Such platform has a good stability; however, it needs a high requirement for the mooring system installation and the cost is higher.

Control of wind turbine systems

A wind turbine control system is composed by a set of sensors, actuators, hardware and software. Signals are captured by sensors, and are sent to the hardware and software. Then, output signals such as the blade pitch and generator torque control can be generated for the actuators (Olondriz Erdozain 2019). The main control objectives of a wind turbine control system are the regulation of power output while reducing the fatigue loads. As the size and capacity of wind turbines are getting larger, the control system becomes more and more important.

There are three sequences of control: safety control, supervisory control and closed-loop control (Burton, Sharpe, Jenkins, and E. Bossanyi 2001). Safety control ensures that the wind turbine works under a safety operation state; safety control is responsible for shutting down the system in case of emergency. Supervisory control is responsible for determining the operating state of wind turbines and, for switching from one operating state into another. When a wind turbine starts to produce energy, the first control objective is to maximum the power or limit it at its rated value. The choice of power level production depends on the different operating regions in which the system is evolving as detailed in the next subsection. For large scale wind turbines, the fatigue loads reduction is also an important control objective.

Operating regions

Among the numerous types of wind turbines (Tong 2010), the variable speed horizontal-axis wind turbine is the most popular used in large-scale wind turbines. Such wind turbines admit 4 operating regions which are classified by the wind speed, the control objectives varying with the different regions (E. A. Bossanyi 2000; Bianchi, De Battista, and Mantz 2006; J. Jonkman, Butterfield, et al. 2009; Hazim Namik 2012). Figure 3 displays the 4 operating regions of those wind turbines.

- **Region I:** The wind speed is slower than the cut-in wind speed. In this case, the wind is too slow to start-up the wind turbine; no electric power is generated.

- **Region II:** When the wind speed is between the cut-in and the rated wind speed, the wind turbine works in Region II. In this region, the generator rotation speed is below the rated speed, the main control objective of this region being then to maximize the power output.

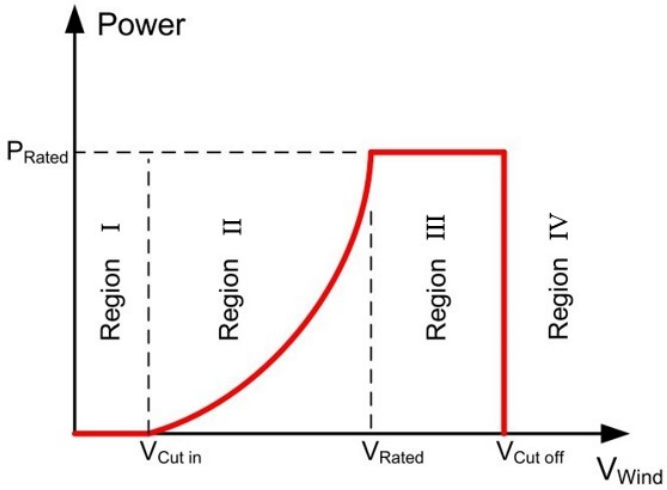

Figure 3 – Four operating regions of wind turbine (Hazim Namik 2012).

This region is also known as the generator torque region since the generator torque is controlled in order to maximize the power. The pitch angle of the blades is so maintained at an optimum value allowing a large value of the power coefficient (Olondriz Erdozain 2019). Therefore, the famous power optimization technique, called maximum point power tracking (MPPT) (Beltran, Ahmed-Ali, and Benbouzid 2008; Bianchi, De Battista, and Mantz 2006) is used.

- **Region III:** When the wind speed is higher than its rated value and lower than the cut-off wind speed, the wind turbine works in Region III (also known as *above-rated* region). In this region, the control goal is no longer to maximize the power output, but to limit it to its rated value in order to protect the components of wind turbine. Then, the blade pitch control is activated to limit the rotor speed, and thereby regulates the power. The generator torque in this region has two control strategies:

  1. keep the generator torque at its rated value (Γ_{g0}). Then, the power P can be regulated by the rotor speed Ω_r according to the following formula (n_g the gear box ratio)

$$P = n_g \Gamma_{g0} \Omega_r \tag{1}$$

  2. the generator torque is controlled inversely proportional to the rotor speed in order to

limit the of power fluctuation from the rated value P_0, *i.e.*

$$\Gamma_g = \frac{P_0}{n_g \Omega_r} \tag{2}$$

- **Region IV:** Finally, if the wind speed exceeds the cut-off wind speed, for the safety of the wind turbine system, the shut-down mode is activated in this region.

Another operating mode of the wind turbine system is called emergence stop, that is activated for example when a fault is detected. Furthermore, the start-up and shut-down of the turbine are decided by the supervision control. Those control logic are not considered in this work.

Control strategies are designed with respect to the current region. **This thesis is focused on the control problems of FWT in the Region III.**

Blade pitch control

For wind turbine control systems, many actuators such as blade pitch angle, generator torque, turbine yaw drive ..., are available in order to achieve the control objectives in the different operating regions (H. Namik and K. Stol 2013). Among those actuators, the generator torque and, especially, the blade pitch are most commonly used. For the blade pitch control, two different strategies are available: collective blade pitch (CBP) control and individual blade pitch (IBP) control.

Collective blade pitch control

Collective blade pitch control is the most widely used in the installed wind turbines (Njiri and Söffker 2016), This blade pitch control strategy allows to control all the blades (normally 3 blades) collectively, namely, the control signal for all the blade pitch actuators is identical. When the wind turbine operates in Region III, CBP control is able to regulate the power output at its rated value to protect the generator and the mechanical structure of wind turbine. For a conventional wind turbine, generator torque is fixed at its rated value in Region III, the CBP closed-loop control being obtained by a feedback of error between the rotor speed and its rated value. One of the most common control scheme is the proportional-integral-derivative (PID) control (Hand and Balas 2000).

Obviously, given that a similar action is applied to whole the blades, such control scheme is single-input single-output (SISO) one. If additional control objectives must be achieved, the CBP control must be redefined by a particular way (see the sequel of this thesis) to get satisfying performances without compromising power regulation or other objectives (H. Namik and K. Stol 2013).

Individual blade pitch control

Individual blade pitch control is a recently emerging technology that provides individual control signal to each blade. It is typically used to reduce the fatigue load (E. A. Bossanyi 2003; Selvam et al. 2009; Van Engelen 2006). Since the load reduction becomes more and more critical with the increasing size of wind turbines, the research of IBP control is one of the hot points.

Thanks to the IBP approach, the number of inputs is increased; therefore, additional control objectives can be added inducing a multiple-input multiple-output (MIMO) system. Some advanced control schemes (Ossmann, Theis, and Seiler 2017; Petrović, Jelavić, and Baotić 2015; Sarkar, Fitzgerald, and Biswajit Basu 2020; H. Namik and K. Stol 2014; Raach et al. 2014) based on IBP approach are applied to achieve different control objectives, such as blade load reduction, rotor speed regulation and platform pitch motion reduction (for the FWT). However, because of the intensive use of blade pitch angle actuators, the requirements for the actuators are relatively high that can explain why IBP control approach is not currently widely used in commercial wind turbines (Menezes Novaes, Araújo, and Bouchonneau Da Silva 2018).

Control of floating wind turbines

Versus the onshore wind turbine that has a fixed bottom, floating wind turbine has additional degree of freedoms (DOFs) due to the floating platform, including platform roll/pitch/yaw rotations; platform horizontal surge/horizontal sway/vertical heave translations (see Figure 4).

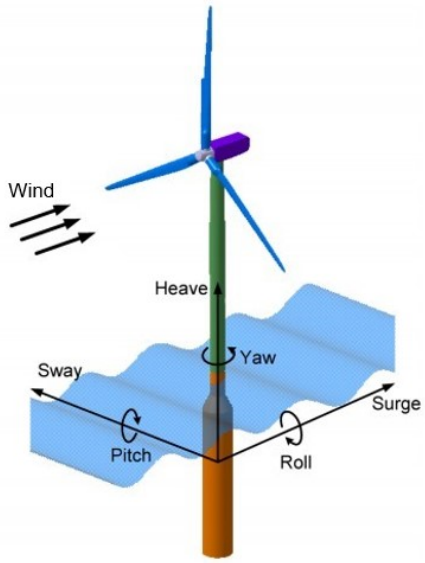

Figure 4 – 6 DOFs platform motions of floating wind turbine (T. Tran, D. Kim, and Song 2014).

Among these motions, the platform pitch motion/rotation has the most significant influence on the FWT system when the wind speed exceeds its rated value (Region III). Such motion can lead to the reduction of power generation quality and the increase of load, and can reduce the lifetime of the FWT (Y. Shi et al. 2017). Hence, the reduction of the platform motions being critical for FWT, there are some solutions available to solve this problem, such as design of different kinds of floating platforms to damp these motions, use of tuned mass dampers providing stiffness and damping or development of control strategies reducing the motions and regulating the power (Hazim Namik 2012). The thesis is focused on the latter improvement way.

Some previous studies (Skaare et al. 2007; Larsen and Hanson 2007; J. Jonkman 2008a) have shown that the traditional control approach for onshore (fixed bottom) wind turbines cannot be directly used for the floating ones due to the fact that these approaches do not take the platform pitch into consideration. In case of use, they result in large resonant platform motions, also known as negative damping (Skaare et al. 2007) (see Figure 5). Such unstable dynamics can be explained as follows: assume that the floating platform is pitching against the wind in Region III; the relative wind speed captured by the rotor increases. So, the traditional blade pitch controller reduces the aerodynamic torque in order to ensure a constant rotor speed/power regulation. However, at the same time, the aerodynamic thrust on the rotor is reduced as well. Such phenomenon leads to the platform pitching forward more, this motion will increase the relative wind speed on the rotor, accelerating the rotor rotation speed (Fischer and Loepelmann 2016). In summary, because of the negative damping, there exists a trade-off between the power regulation and the platform pitch motion reduction (Figure 5). Thus, specific controllers for FWT must be developed.

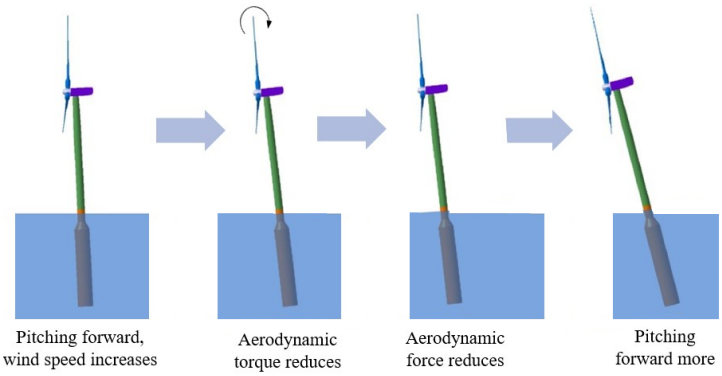

Figure 5 – Negative damping phenomenon of floating wind turbines, adapt from (T.-T. Tran and D.-H. Kim 2015).

To summarize, as detailed before, the control objectives of a FWT in Region III are:

- firstly, regulation of the power at its rated value to protect the generator and the mechanical structure;
- then, reduction of the platform pitch motion, ensuring the stability of the platform;
- in addition, in order to extend the service life of FWT, another control objective lies in the reduction of structure load.

Linear approaches

Lot of works have been done in the development of control algorithms to counteract the negative damping of FWT. The most well-known approach is the gain-scheduled proportional-integral (GSPI) control (Larsen and Hanson 2007; J. Jonkman 2008a) using CBP control technology; such method is based on the baseline rotor speed control of onshore wind turbines (J. Jonkman, Butterfield, et al. 2009). By detuning the controllers gains such that the natural frequency of close-loop system is lower than the platform pitch natural frequency, then the platform pitch motion can be greatly reduced. However, due to the low bandwidth of the control, the rotor speed variation is increased, that means that the power regulation in Region III is degraded. In (Wakui, Yoshimura, and Yokoyama 2017), novel parameters setting is proposed for the GSPI controller, the parameters being determined to obtain a natural frequency of the closed-loop system higher than the natural frequency of the platform pitch motion. Furthermore, the objective is to get a damping coefficient greater than 1.0. These parameters tuning results in a similar platform pitch motion reduction as the tuning given in (J. Jonkman 2008a), but with a significantly reduction of the power fluctuations around the rated.

In (Lackner 2009; Lackner 2013), gain-scheduled collective blade pitch control is used to track the set point of rotation speed that is defined as a function of the platform pitch velocity, so-called variable power pitch control (VPPC). With this approach, the platform pitch motion is greatly attenuated; however, the power fluctuation is increased.

Linear quadratic regulator (LQR) control based on linear model has been firstly applied to a FWT system in (Hazim Namik, Karl Stol, and J. a. Jonkman 2008), in which the rotor speed variation and platform pitch motion are reduced compared to (J. Jonkman 2008a). Notice that CBP strategy is used in this work, the two control objectives being achieved by using a penalty func-

tion that optimizes the trade-off between the speed regulation and the platform pitching. More recently, many works have been proposed based on LQR approach (Christiansen, Knudsen, and T. Bak 2011) combining with a wind estimator and a state observer to improve the control performances. In (Christiansen, Knudsen, and T. Bak 2014), an additional LQR control loop has been added to an onshore wind turbine controller and reduces power fluctuations and platform oscillations; such approach simplifies the control design of FWT without modifying the onshore controller.

Another popular optimal algorithm, H-infinity (H_∞) control is also used for FWT (Bakka and Karimi 2012; Bakka and Karimi 2012; X. Li and Gao 2015). This class of controllers is designed based on a family of linear state-space model, namely the linear parameter varying (LPV) models. By this way, the controllers ensure better performances than the controllers based on a single linear model. In (Hara et al. 2017), H_∞ control law is implemented to a scaled FWT system. The experimental results show the effectiveness of rotor speed regulation and platform pitch motion reduction. Nevertheless, the authors point out that, for further improvement of the control performances, the use of LPV model is necessary.

In (Hazim Namik and Karl Stol 2010; Namik and Karl Stol 2011; H. Namik and K. Stol 2014), individual blade pitch control is considered with disturbance accommodating control (DAC) for barge, TPL and spar-buoy floating systems. Multiple objectives are achieved by the multiple inputs (IBP angles) controller: the platform motions and tower fatigue are significantly reduced versus the GSPI, as well as the power and rotor speed regulation are improved. However, such improvements have a cost: extensive use of blade pitch actuator (4-12 times larger than GSPI CBP control).

Model predictive control (MPC) is another popular algorithm that is widely adapted to the control of FWT. In (Lemmer, Raach, et al. 2015), a MPC controller using IBP scheme is applied to a 10 MW FWT; good performances have been shown for rotor speed tracking and tower fatigue reduction versus a PI controller. In (Cunha et al. 2014), MPC is adopted combining with the VPPC algorithm: the platform pitch motion is reduced with less power variation than (Lackner 2009). Moreover, the blade as well as the tower fatigue loads are also reduced. In (Raach et al. 2014; Schlipf, Sandner, et al. 2013), nonlinear MPC using wind speed prediction have been introduced, where the incoming wind information is obtained by the light detection and ranging (LIDAR) remote sensing technology. Results show a better performance than the baseline GSPI control.

Limits and nonlinear approaches

The study carried out in this work is motivated by the requirement of developing efficient controllers for floating wind turbines in Region III. The main idea is to propose efficient control strategies that

require very reduced effort of modeling and tuning. As previously recalled, the control algorithms used for the bottom-fixed wind turbines cannot be directly applied to the floating ones. The dynamics of floating platforms, especially the platform pitch motion, must be taken into consideration in the control design process in order to deal with negative damping (Skaare et al. 2007).

The control objectives of a FWT in Region III are: the regulation of the power output at its rated value (as the bottom-fixed wind turbine) and the reduction of the pitch motion of the floating platform. Moreover, the fatigue loads of the structure must be limited.

As detailed in the previous section, numerous works have been made on the control of FWT in Region III. The traditional GSPI controller is adopted to FWT by detuning the controller gains in order to damp the platform pitch motion; modern control theories have also been used based on linear state-space models, such as the LQR, H_∞, DAC ..., in which some studies use optimal algorithms to deal with the trade-off between the power regulation and platform pitch motion by CBP control. Some studies also used MIMO control that uses IBP angles as control inputs to achieve several control objectives (power regulation, platform motion reduction and fatigue load reduction). However, the main part of these studies uses linear representations of the FWTs, these linear models being obtained for a given operating point depending on wind conditions and rotor speed. The linear models are used for the control design: the drawback is that, once the turbine is working away from the operating point, the controller loses its efficiency and its desired performances. As a consequence, the controller must be tuned for each operating point to ensure its efficiency; another way is the use of LPV model to schedule the controller gains. Such tuning and gain scheduling process is fastidious and is not friendly to wind turbine manufacturers.

An alternative solution would be to base the control law design on more general nonlinear systems. However, the applications of nonlinear control strategies to FWTs are very limited in the literature (Sandner et al. 2012; Homer and Nagamune 2018), the nonlinear models developed in these works appearing to be limited in the frame of control.

Therefore, it is necessary to develop control solutions for FWTs that

- reduce the tuning effort and guarantee high level performances;
- require very few information on system model.

In this thesis, sliding mode control (V. Utkin 1977) is adopted for its robustness and its simplicity; the adaptive versions of such control approach (in its high order version) can deal with the

robust control problem with very limited information of the model and high level performances in spite of uncertainties and perturbations. Notice that, in order to attenuate the negative chattering phenomena of SMC, high order sliding mode control (Yuri Shtessel, Edwards, et al. 2014) combined with gain adaptation (Plestan et al. 2010; Yuri Shtessel, Taleb, and Plestan 2012) have been chosen. Indeed, such algorithms are particularly well-adapted to the FWT control problems because:

- the used adaptive algorithms offer continuous control and thus reduce the chattering that allows to protect the actuators (*i.e.* the blade pitch actuators) from high frequency oscillations;
- they are simple for application that is friendly for manufacturers;
- moreover, the adaptation algorithms dynamically adapt the gains versus uncertainties and perturbations: it avoids the over-estimation of controller gains, and strongly reduces the tuning effort;
- the adaptive versions of SMC algorithms require very reduced information on modeling;
- finally, these approaches allow to propose controllers with a single set of tuning parameters for the whole operating domain that strongly simplifies the control design.

Organization and contributions

This thesis consists of five parts:

Chapter 1 describes the modeling of a FWT, simulation set-up and performance analysis tools. The modeling includes the physical model that concerns the coordinates system, the power capture system, the drive train system and a brief explanation of hydrodynamics of the floating structure. Then, linearized models of FWT are introduced. Simulation context (FAST (Jason M Jonkman, M. L. Buhl Jr, et al. 2005)) and the research object (a 5MW spar-buoy FWT) are also introduced.

In **Chapter 2**, adaptive high order sliding mode control is applied to the FWT based on collective blade pitch approach. Firstly, the problem statement and the control objectives of the FWT are discussed: regulation of the rotor speed at its rated value (assuming that the generator torque is fixed) and reduction of the platform pitch motion. Then, high order sliding mode control with different adaptation strategies are recalled, including the adaptive super-twisting (ASTW) proposed by (Yuri Shtessel, Taleb, and Plestan 2012) and a recently developed homogeneity based controller with varying exponent parameter (HCVP) (Tahoumi, Plestan, et al. 2019). Meanwhile, a new simplified adaptive super-twisting (SAST) algorithm with very few tuning parameters (only 2 parameters are required) is proposed. All of those algorithms are applied to FWT in the FAST/SIMULINK environment and the performances are compared with the GSPI (J. Jonkman 2008a) control for

different scenarios. Simulation results shows that the controllers designed in this chapter have better performances than the GSPI controller with reduce tuning effort and knowledge of system model.

In **Chapter 3**, a permanent magnet synchronous generator (PMSG) is supposed to equip the FWT. The control is not only acting on the aero/hydrodynamic part, but also considers the control of electrical part. The control objectives are stated as the regulation of the power at its rated value, the reduction of the platform pitch motion, and the reduction of the ripple effect of the generator. Unlike the previous chapter (in which the generator torque was fixed at its rated value), the power regulation is achieved by the combination of torque control and rotor speed control. Both ASTW and SAST controllers are used in this chapter; the simulation results are compared with GSPI.

In **Chapter 4**, the individual blade pitch (IBP) approach is studied. Therefore, besides regulating the power and reducing the platform pitch motion, the controller proposed in this chapter takes the structural load reduction into consideration. The overall control scheme consists in two parts: the CBP control loop for the rotor speed regulation and platform pitch reduction, and the IBP control loop for the blade load reduction. The ASTW approach is applied in this chapter, simulation results and their analysis being given at last.

In **Chapter 5**, the proposed simplified adaptive super-twisting (SAST) controller is applied to an experimental floating wind turbine set-up in the ECN wave tank. The experimental set-up is composed by a reduced scale system in the wave tank and a numerical one modeled by FAST software. The introduction of the reduced scale system and the numerical model are firstly described. Then, three kinds of controllers are briefly introduced and implemented: the university of Denmark (DTU) GSPI controller (Hansen and Henriksen 2013) with Olav Olsen (Yu et al. 2018) parameters setting, the LQR control developed by D-ICE company and the SAST control proposed in Chapter 2. Experiments are made by using the three controllers under same wave and wind conditions in Region III; experimental results are analysed and compared.

Some of the results presented in this thesis have been published or submitted for publication in the following journals and conferences.

International journals

[1] Zhang. C and Plestan. F, "Adaptive sliding mode control of floating offshore wind turbine equipped by PMSG", *Wind Energy*, DOI 10.1002/we.2601, 2020.

[2] Gutierrez. SV, Zhang. C, Plestan. F and de León-Morales. J, "A simplified version of adaptive super twisting for control of floating wind turbine", *Control engineering Practice*, first revision, 2020.

[3] Zhang. C and Plestan. F, "Individual/collective blade pitch control of floating wind turbine based on adaptive second order sliding mode", Ocean Engineering, submitted, 2020.

International conferences

[1] Zhang. C, Gutierrez. SV, Plestan. F and de León-Morales. J, "Adaptive super-twisting control of floating wind turbines with collective blade pitch control", *IFAC Workshop on Control of Smart Grid and Renewable Energy Systems*, Jeju, Republic of Korea, 2019.

[2] Zhang. C, Tahoumi. E, Gutierrez. SV and Plestan. F and de León-Morales. J, "Adaptive robust control of floating offshore wind turbine based on sliding mode", *IEEE Conference on Decision and Control*, Nice, France, 2019.

[3] Zhang. C and Plestan. F, "Power and motion control of a floating wind turbine: an original approach based on adaptive second order sliding mode control", *IFAC World Congress*, Berlin, Germany, 2020.

Chapter 1

System modeling and analysis tools

Contents

1.1 Introduction

A wind turbine is mainly composed by rotor, blades, tower and nacelle including gear box and generator, as shown in Figure 1.1; for the floating one, there is an additional floating platform. The principle of energy conversion applied to wind systems is that the kinetic energy of the wind is received by the blades and forces the rotor to rotate. Then, the kinetic energy is transferred into mechanical energy; in the nacelle, the low speed shaft (LSS) rotates with the rotor and is connected to a generator with the high speed shaft (HSS) via a gear box. Then, the mechanical power is transferred into electric energy.

This chapter describes the modeling of a FWT system and the simulation environment. The first section introduces the physical model of the FWT, including the coordinates system, the power

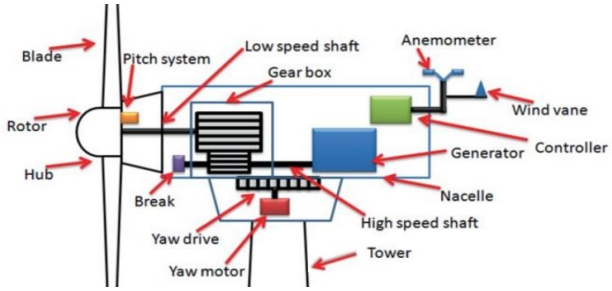

Figure 1.1 – Components of a wind turbine (Karimirad 2014).

capture system [1], the drive train system and a brief explanation of hydrodynamics of the floating structure. The second part describes the linearized model of the FWT system, for the purpose of control design; a reduced linear model is introduced and compared with FAST nonlinear model. The last part presents the analysis tools, the FWT under interest in this work, and the performance indicators used in this work.

1.2 Physical model

This section is devoted to the description of the models of the FWT elements. The coordinate system, power capture system, drive train system and the hydrodynamics of FWTs are introduced.

1.2.1 Coordinate systems

Figure 1.2 displays the 6 DOFs of motions of a floating platform. There are the platform surge, sway and heave translations and the platform roll, pitch and yaw rotations.

The platform surge translation is along with the x_p-axis (pointing horizontally in the downwind direction); the platform sway translation is along with the y_p-axis (perpendicular to the x_p-axis in the horizontal direction, pointing to right when looking face to the wind). Finally, the platform heave translation is along with the z_p-axis (pointing vertically upward opposite to gravity). When the platform is rolling, it rotates about the x_p-axis; when the platform is pitching, it rotates about the y_p-axis; when the platform is yawing, it rotates about the z_p-axis (Jason M Jonkman, M. L. Buhl Jr, et al. 2005).

Tower base coordinate system is shown in Figure 1.3. Its origin is located in the center of the intersection of tower base and platform: x_t-axis pointing horizontally in the opposite of upwind direction;

1. In this chapter, only the mechanical part of power capture system is discussed; the electrical part will be detailed in the next chapter.

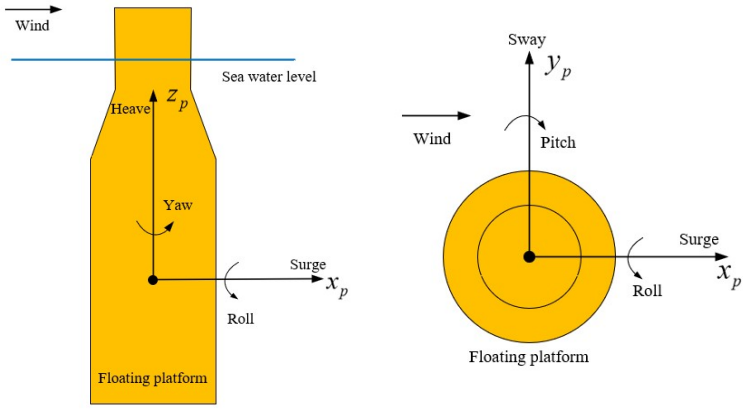

Figure 1.2 – Floating platform coordinate system. **Left.** Front view. **Right.** Top view.

y_t-axis being perpendicular to the x_t-axis in the horizontal direction, pointing to right when looking face to the wind. Finally, z_t-axis is pointing vertically up from the tower base.

In this coordinates system, tower base fore-aft, side-to-side and torsional moments are defined. Tower base fore-aft moment is caused by the tower pitching about the y_t-axis; tower base side-to-side moment is caused by the tower rolling about the x_t-axis; tower base torsional moment is caused by the tower yawing about the z_t-axis (Jason M Jonkman, M. L. Buhl Jr, et al. 2005).

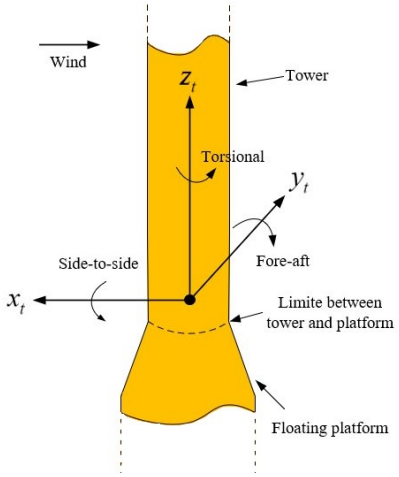

Figure 1.3 – Tower base coordinate system.

Blade coordinates system is shown in Figure 1.4-left. x_{bi}-axis ($i = \{1,\ 2,\ 3\}$ for blade 1, 2 or 3 respectively) is pointing horizontally to the nacelle from the center of the blade root; z_{bi}-axis is

pointing along the pitch axis towards the tip of blade i; y_{bi}-axis is parallel with the chord line (see Figure 1.4-right), pointing to the trailing edge (see Figure 1.4-right).

The blade flap-wise moment is caused by the flap-wise force about the y_{bi}-axis at the blade root; the blade edge-wise moment is caused by the edge-wise force about the x_{bi}-axis at the blade root.

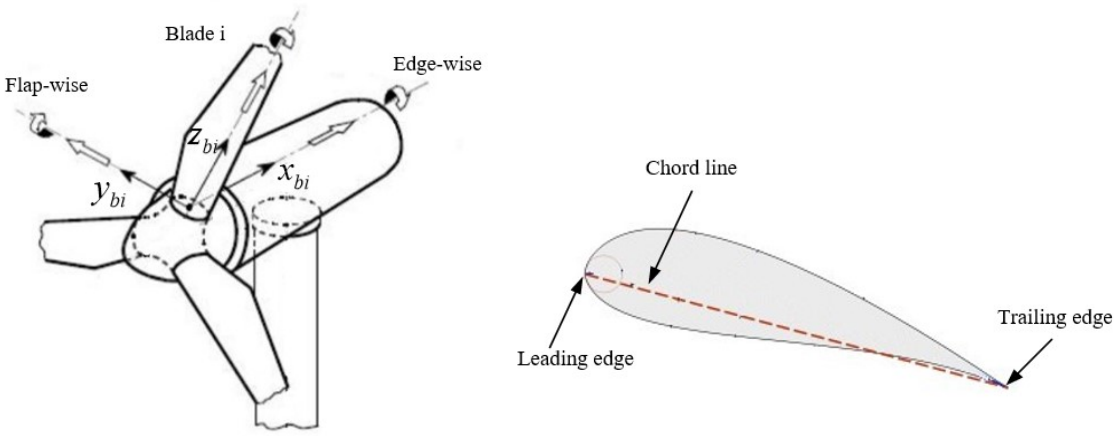

Figure 1.4 – **Left.** Blade coordinates system, adapted from (Jelavić, Petrović, and Perić 2010). **Right.** Blade section.

Finally, the rotor azimuth angle ψ is defined between the vertical axis and the current position of the blade #1 symmetrical axis (see Figure 1.5).

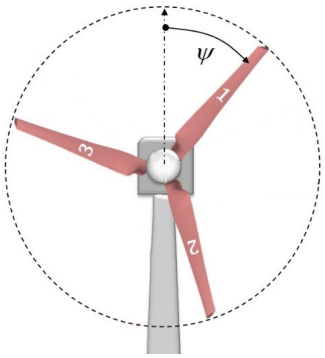

Figure 1.5 – Rotor azimuth angle (Cheon et al. 2019).

1.2.2 Power capture system

The turbine captures energy from the wind passing through its blades and transforms it into mechanical energy. Assume that the wind turbine is facing the wind; then, the mechanical power can be expressed as (Huang, F. Li, and Jin 2015; Guenoune et al. 2017; Yenduri and Sensarma 2016; Pöschke, Fortmann, and Schulte 2017)

$$P = \frac{1}{2} C_p(\lambda, \beta) \lambda \rho \pi R^2 V^3 \tag{1.1}$$

with

- β the blade pitch angle;
- R the radius of the blades;
- ρ the air density; at a temperature of $15°C$ and an atmospheric pressure of 1.0132 bar, the air density is approximately equal to 1.205 kg/m^3;
- V the wind speed;
- λ the tip speed ratio (TSR) being the ratio between the rotation speed of the rotor Ω_r and the wind speed V, and reading as

$$\lambda = \frac{\Omega_r}{V} R. \tag{1.2}$$

The power coefficient C_p characterizes the efficiency of the conversion of wind energy into mechanical energy; such coefficient can be obtained either by real-world experiments or by using accurate simulations. Then, it can be described by different approaches, as look-up tables (Odgaard, Stoustrup, and Kinnaert 2013) (see Figure 1.6) or fitted to a polynomial (Raach et al. 2014) by the following expression

$$\begin{aligned} C_p &= c_1(c_2\xi - c_3\beta - c_4)e^{c_5\xi} \\ \xi &= \frac{1}{\lambda + 0.08\beta} - \frac{0.035}{\beta^3 + 1} \end{aligned} \tag{1.3}$$

with $c_1 - c_5$ the C_p curve fitting coefficients (Guenoune et al. 2017). Therefore, C_p is not well-known and introduces uncertainties to the model.

Figure 1.6 displays the power coefficient C_p versus the TSR λ, for a given blade pitch angle β. It is then strongly influenced by the wind since λ is a function of V. **Then, from** (1.1)**, the power of**

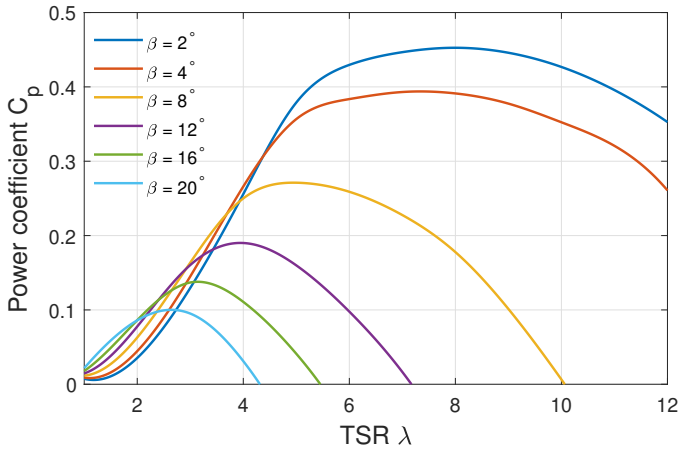

Figure 1.6 – Power coefficient C_p versus the tip-speed ratio λ, for different blade pitch angle β.

the turbine for different wind speeds can be adjusted thanks to the blade pitch angle β.

In addition, wind fluctuations induce torque fluctuations, increasing the fatigue loads on the drive shaft and also affecting the quality of the produced power produced. So, there is a real interest in designing variable speed wind turbines, to adapt their rotation speeds to wind variations in order to obtain the most appropriate C_p value and therefore to optimize the power output in different operating regions (for definition of regions, see previous chapter). The aerodynamic torque developed by the turbine blades is defined by (Guenoune et al. 2017; Huang, F. Li, and Jin 2015)

$$\Gamma_a = \frac{1}{2}\frac{C_p(\lambda,\beta)}{\lambda}\rho\pi R^3 V^2. \tag{1.4}$$

1.2.3 Drive train system

The purpose of the drive train is to transmit wind power and mechanical torque from the turbine to the electric generator (Burton, Sharpe, and Jenkins 2001). There are different types of drive train models, depending on the number of the mass, such as six-mass, three-mass and two-mass models (Muyeen et al. 2007). Among those models, the two-mass model has been widely used in the literature (Novak, Jovik, and Schmidtbauer 1994; Beltran, Ahmed-Ali, and Benbouzid 2008; Abo-Khalil et al. 2019). The complexity of the two-mass model is reduced, but this mdoel is sufficient for characterizing the dynamics of the drive train (McFadden and Basu 2016).

Figure 1.7 illustrates a two-mass drive train model. This model consists in the following elements: two mass with rotational inertia J_r and J_g representing the inertia of the mechanical part (blades, tower and hub) and electrical part (generator rotor) respectively, a low speed shaft (LSS) modeled by a torsional spring and a torsional damper, a rigid high speed shaft (HSS), and finally a gear box

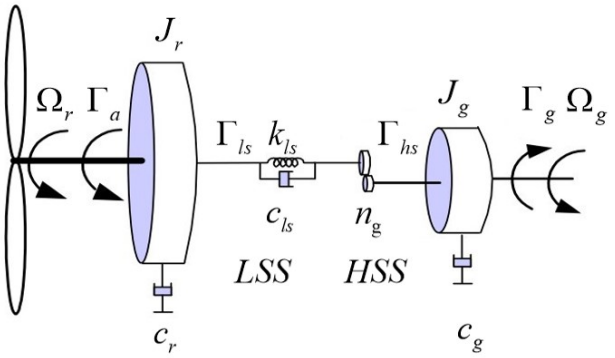

Figure 1.7 – Two-mass drive train model with a gear box (adapted from (Abo-Khalil et al. 2019)).

connecting the two parts, mechanical one (turbine) and electrical one (generator). The mathematical representation of such model is given by

$$\begin{aligned} J_r\dot{\Omega}_r &= \Gamma_a - c_r\Omega_r - \Gamma_{ls} \\ J_g\dot{\Omega}_g &= \Gamma_{hs} - c_g\Omega_g - \Gamma_g \\ \dot{\Gamma}_{ls} &= k_{ls}(\Omega_r - \Omega_g) - c_{ls}(\dot{\Omega}_r - \dot{\Omega}_g) \end{aligned} \tag{1.5}$$

with

- Ω_r the rotor speed;
- Ω_g the electric generator speed;
- n_g the gear box speed-up ratio;
- Γ_a and Γ_{ls} the aerodynamic torque generated by the wind and the LSS torque, respectively;
- Γ_g and Γ_{hs} the generator torque and the HSS torque, respectively;
- c_r, c_g and c_{ls} the damping coefficients of the turbine, generator and shaft, respectively;
- k_{ls} the stiffness coefficient of the LSS.

For simplicity, assume that the rotor is perfectly rigid. So, ignoring the shaft friction (see Figure 1.8), the dynamics of the drive train reads as

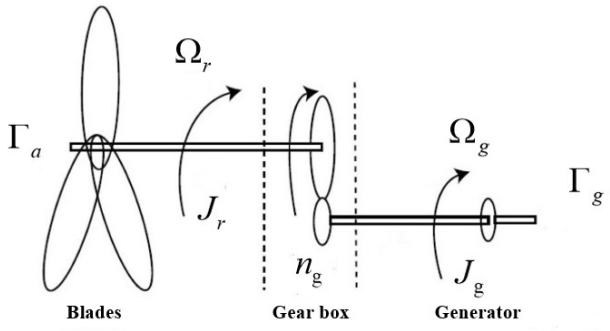

Figure 1.8 – Reduced wind turbine drive train with a gear box (Betti et al. 2013).

$$J\dot{\Omega}_r = \Gamma_a - n_g\Gamma_g \tag{1.6}$$

with J the total inertia of the drive train system. The relation between the total inertia J, and both the rotational inertia J_r and J_g reads as

$$J = n_g^2 J_g + J_r. \tag{1.7}$$

1.2.4 Hydrodynamics

Different from the fixed-bottom wind turbine, due to the presence of a floating platform, additional 6 DOFs (platform horizontal surge, horizontal sway, vertical heave translation and platform roll, pitch, yaw rotation - Figure 1.2) must be considered for the floating wind turbines. These 6 DOFs are infected by the hydrodynamics forces caused by waves, mooring system, and by the aerodynamic forces caused by the wind. Of course, all these factors have a great influence on translations and rotations of the platform. Additionally, in the offshore environment, the dynamics of the platform are highly nonlinear and coupled with the aerodynamics of the turbine system; it is clearly a very complex task to model the hydrodynamics in control design context (Jason M Jonkman, M. L. Buhl Jr, et al. 2005; Y. Shi et al. 2017; Cho 2020). Therefore, specific models for FWT are required in a reduced scale and will be introduced in the next section.

1.3 Linearized model

In the previous subsection, it has been concluded that the blade pitch angle affects the aerodynamic torque Γ_a and thereby, control the rotor speed Ω_r and the power output. However, the dynamics between the floating platform and the blade pitch angle are not obvious; namely, from the control design point of view, the models of the platform (G et al. 2012; Sandner et al. 2012) in the literature are not usable. Therefore, in order to simplify the design process of the controller, linear models

have been usually considered for a reduced number of DOFs.

Linear models used in this work are obtained by the FAST software [2] (B. Jonkman and J. Jonkman 2016). FAST code contains complex and precise wind turbine nonlinear models; such nonlinear models are used as simulation objects that provide accurate aerodynamic and structure responses to the wind, wave, blade pitch... Nevertheless, on the other hand, due to the complexity of the models, from a control point-of-view, such models can not be used for the control design. To this end, FAST has the function of generating linearized representations of wind turbine; then, linear state-space models can be extracted from the FAST and can be used as the "plant" for control design and analysis (Jason M Jonkman, M. L. Buhl Jr, et al. 2005).

The linear model carried out from FAST depends on the considered operating point of the wind turbine. At a specific operating point that depends on the wind speed and the rotor speed, a set of values of the wind turbine system are determined, for example: system DOFs displacements, velocities and accelerations, blade pitch angle .... Once the wind turbine is operating in a steady condition, the operating point values are periodic with respect to the rotor azimuth angle (see Figure 1.5). This periodicity is driven by aerodynamic loads, which depend on the rotor azimuth angle in the presence of prescribed shaft tilt, wind shear, yaw error, or tower shadow. Gravitational loads also drive the periodic behavior when there is a prescribed shaft tilt or appreciable deflection of the tower due to thrust loading (Jason M Jonkman, M. L. Buhl Jr, et al. 2005). Then, for a given operating point, FAST generates a periodic state-space model with a period equal to the time of one rotor revolution. Then, around the operating conditions (x_{op}, u_{op}, δ_{op}), the model reads as

$$\dot{x} \quad = \quad A(\psi) \cdot x + B(\psi) \cdot u + B_d(\psi) \cdot \delta \tag{1.8}$$

where

- $x = \begin{bmatrix} q \\ \dot{q} \end{bmatrix}$ denotes the state vector, $x \in \mathbb{R}^N$, q being the DOFs of the wind turbine system (e.g. rotor azimuth, blade deflections, platform rotations...). The dimension of q and $\dot{q}$ depends on the DOFs enabled in FAST (that is a user's choice);

- u is the control input. For a CBP (see previous chapter) controller, $u = \beta_{col}$ with β_{col} the collective blade pitch angle. For a IBP (see previous chapter) controller, $u = [\beta_1 \ \beta_2 \ \beta_3]^T$ is the control input vector with β_1, β_2 and β_3 the pitch angles of the three blades;

- $A(\psi)$ is the state matrix ($N \times N$), and is periodic with respect to the rotor azimuth angle ψ;

2. A well-known open source software for wind turbine research; it will be introduced in Section 1.4.

- $B(\psi)$ is the input matrix ($N \times 3$), and is periodic with respect to ψ;
- $B_d(\psi)$ is the wind input disturbance matrix ($N \times 1$), and is periodic with respect to ψ;
- δ is the wind disturbance input;
- x_{op}, u_{op} and δ_{op} are the value of the states, inputs and wind speed at the operating point, respectively.

The elements of $A(\psi)$, $B(\psi)$ and $B_d(\psi)$ depend on the properties of the system, such as stiffness and damping. As previously mentioned, these matrices are periodic with respect to the rotor azimuth ψ that induces a periodic model (1.8). In order to simplify the control design, a linear time-invariant model can be derived by averaging system (1.8) with respect to ψ. Notice that the periodic models can be averaged when the system states are located in non-rotating frames, such as the platform frame and the tower base frame (see Figures 1.2 and 1.3).

In the sequel, the azimuth-average model will be used for design of CBP control. However, for the IBP control, the dynamics of each blade are in the reference rotating frame (see Figure 1.4) located in each blade respectively; so, the periodic information on the rotating frame is lost while averaging. Therefore, multi-blade coordinate (MBC) transformation (G. Bir 2008; Karl Stol et al. 2009; Hazim Namik and Karl Stol 2010) is used in order to keep the periodic information before averaging. This class of solution will be detailed in Chapter 4.

1.3.1 Reduced state-space model

The FAST nonlinear floating wind turbine models can have huge number of DOFs, including the blade flap-wise/edge-wise bending mode, the tower fore-aft/side-to-side bending-mode, the platform rotation and translation... In the present work, in order to simplify the control design, a reduced linear model is used with only 2 DOFs, that are the rotor azimuth ψ and the platform pitch rotation φ. This choice has been made because these quantities are related to the control objectives of the study.

Furthermore, as mentioned in the previous subsection, the linearized model (1.8) is periodic with respect to the rotor azimuth angle ψ. Since the two DOFs chosen are in the non-rotating frame of reference, the periodic model can be azimuth averaged, in order to get a linear time-invariant one, reading as

$$\dot{x} = A_{Avg} \cdot x + B_{Avg} \cdot u + B_{dAvg} \cdot \delta \tag{1.9}$$

where A_{Avg}, B_{Avg} and B_{dAvg} are obtained by averaging $A(\psi)$, $B(\psi)$ and $B_d(\psi)$. In a first time, only CBP approach is considered, so, the control input u is the collective blade pitch angle β_{col}. According to FAST linearization, the column associated with the rotor azimuth state is zero, meaning that this state can effectively be eliminated from the state space model (J. Jonkman 2019). Hence, rotor azimuth ψ is not included, that gives a 3-state vector consisting of

$$x \;=\; \begin{bmatrix} \varphi & \dot{\varphi} & \Omega_r \end{bmatrix}^T$$

with φ the platform pitch angle, $\dot{\varphi}$ the platform pitch angle velocity and $\Omega_r = \dot{\psi}$ the rotor speed.

Notice that model (1.9) is efficient only when the system is close from the considered operating point around which it has been established. Among a large operating domain, A_{Avg}, B_{Avg} and B_{dAvg} obtained for a fixed operating point can not accurately represent the system dynamics. Therefore, in order to ensure the accuracy of the linearized system, many systems (1.9) should be carried out at different operating points. For example, when the considered floating wind turbine is operating at a wind speed equals to $18m/s$ and rotor speed equals to its rated value $\Omega_{r0} = 12.1\ rpm$, one has

$$A_{Avg} = \begin{bmatrix} 0 & 1 & 0 \\ -0.0141 & -0.0405 & -0.0004 \\ -0.0757 & -2.3031 & -0.2304 \end{bmatrix}, B_{Avg} = \begin{bmatrix} 0 \\ -0.0035 \\ -1.1864 \end{bmatrix}, B_{dAvg} \;=\; \begin{bmatrix} 0 \\ 0.0001 \\ 0.0276 \end{bmatrix} \tag{1.10}$$

whereas one gets, for a wind speed equals to $20m/s$ and a rotor speed equals to Ω_{r0}

$$A_{Avg} = \begin{bmatrix} 0 & 1 & 0 \\ -0.0141 & -0.0403 & -0.0006 \\ -0.0679 & -2.5069 & -0.3182 \end{bmatrix}, B_{Avg} = \begin{bmatrix} 0 \\ -0.0035 \\ -1.3856 \end{bmatrix}, B_{dAvg} \;=\; \begin{bmatrix} 0 \\ 0.0001 \\ 0.0030 \end{bmatrix} \tag{1.11}$$

Consequently, due to the wind variations in Region III (11.3 m/s to 25 m/s) and considering a large operating domain, it is reasonable to assume the FWT model as follows

$$\dot{x} \;=\; A_{Avg}(x,t) \cdot x + B_{Avg}(x,t) \cdot u + B_{d_{Avg}}(x,t) \cdot \delta \tag{1.12}$$

with $A_{Avg}(x,t)$, $B_{Avg}(x,t)$ and $B_{dAvg}(x,t)$ the matrices containing the parameters of the reduced two DOFs model in the operating domain, namely, the matrices are varying in the different operating points. It is clear that these matrices are evolving with respect to wind speed (depending on time) and rotor speed (depending on the state variable Ω_r).

Moreover, for the convenience of the following nonlinear control design, by a more general point-of-view, the system (1.12) could be viewed as a particular class of nonlinear systems reading as

$$\dot{x} \quad = \quad f_{wt}(x,t) + g_{wt}(x,t)u \tag{1.13}$$

where

- $f_{wt}(x,t)$ contains the term represented by $A_{Avg}(x,t)\cdot x$ and the term $B_{d_{Avg}}(x,t)\cdot\delta$ containing the uncertainties of the system and the perturbations introduced by wind, waves and other external environments;

- $g_{wt}(x,t) = B_{d_{Avg}}(x,t)$ is the input function.

1.3.2 Comparisons with FAST nonlinear reduced model

In the previous subsection, linearized models are carried out from FAST software around different operating points. In the current subsection, simulations have been made between the linearized model (1.9) and the FAST nonlinear model in order to verify if

- the linear model has similar time response as the FAST model and can be used for the control design;

- the linear model obtained for a given operating point is accurate enough if the system operates away from the operating point.

Consider the model (1.9) obtained for a wind speed equals to 18 m/s with no wave, and a rotor speed equals to its rated value; in this condition, the reduced FWT is described by (1.10). On the other hand, FAST can run a nonlinear model with rotor azimuth and platform pitch enabled as DOFs. Simulations are made on the linear and FAST models respectively, in the two following cases

- **Case 1**: 18 m/s constant wind and without wave (similar conditions as the linearization ones);

- **Case 2**: 20 m/s constant wind and without wave.

Both cases of simulations have similar control input, the collective blade pitch angle β_{col} being fixed at a constant value (the value selected here is the operating point value of blade pitch angle derived from the FAST linearization with wind speed equals to 18 m/s, rotor speed equals to 12.1 rpm). Figure 1.9 shows the responses of platform pitch φ and rotor speed Ω_r obtained by both linearized and FAST models when the wind speed equals to 18 m/s (*e.g.* the system operates at the operating

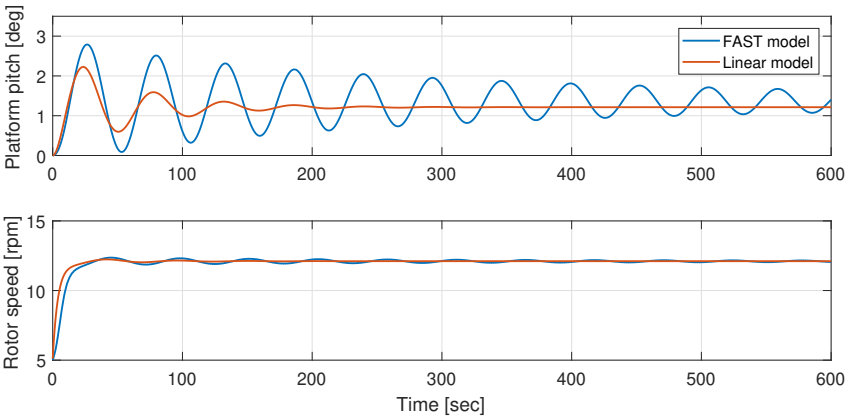

Figure 1.9 – **Case 1.** Platform pitch angle φ (top-deg) and rotor speed Ω_r (bottom-rpm) obtained with both linear and FAST models versus time (sec).

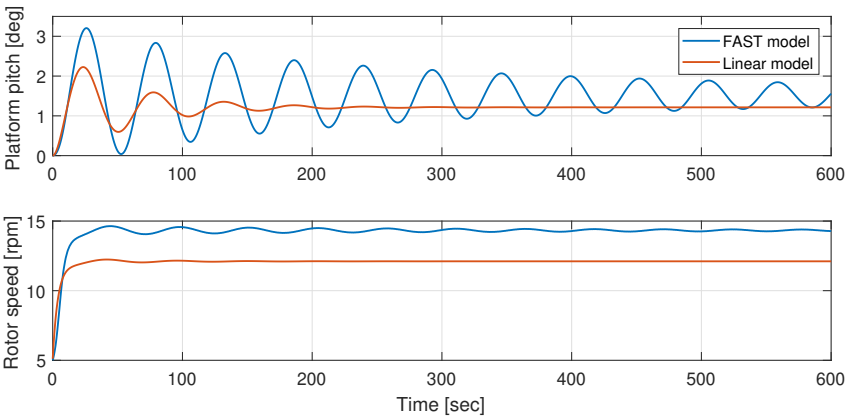

Figure 1.10 – **Case 2.** Platform pitch angle φ (top-deg) and rotor speed Ω_r (bottom-rpm) obtained with both linear and FAST models versus time (sec).

point). It is clear that both the platform pitch angle and rotor speed are finally converging to the same values on the two model. However, there are huge differences in the transient behavior (more oscillating response for FAST model). Figure 1.10 displays the similar simulations but with wind speed equals to 20 m/s that means that for the linearized model, the system works away from the operating point. Obviously, the responses of the platform pitch angle and the rotor speed of the linearized model cannot converge to the same values as the FAST nonlinear model, *e.g.* the system model is no longer accurate if the system operates away from the operating point. As previously, the transient behavior is really different.

Therefore, as declared in the previous subsection, if linear control approaches are used, it is necessary to linearize the nonlinear model at different operating points. However, as previously viewed, dynamic behavior is not repeated by an accurate way. In this thesis, it is exactly the way that one does not want because it makes the control design much more complex and probably less efficient. Indeed, it means "one operating point = one controller tuning". It is the reason why another way will be used: control design based on nonlinear uncertain system.

1.4 Simulation set-up and performance analysis tools

1.4.1 FAST software

FAST (Fatigue, Aerodynamics, Structures and Turbulence) is an open source software developed by National Renewable Energy Laboratory (NREL) (Jason M Jonkman, M. L. Buhl Jr, et al. 2005) and can be used to analyse the structural dynamics of wind turbine systems. FAST is using models of the tower, blades and drive-train as flexible elements and is using bending mode shapes for the analysis. Each blade has two flap-wise and one edgewise bending modes. The tower has two fore-aft and two side-side bending modes. The drive-train flexibility is modelled through a linear spring and a damper for the low speed shaft. The remaining elements of the wind turbine (nacelle and hub) are modelled as rigid bodies. The fidelity of the model can be set by selecting which DOFs are to be enabled or disabled (there are 24 DOFs in FAST model).

With the development of floating wind turbines, additional dynamics introduced by floating offshore environment is considered in the FAST code; indeed, the hydrodynamics module and mooring lines module used for floating platform dynamics are developed in (J. Jonkman and Sclavounos 2006). As shown in Figure 1.11, the overall FAST floating wind system is composed by the coupled aerodynamics, hydrodynamics, turbine dynamics and mooring line dynamics.

As detailed in subsection 1.3, FAST also has the capability to provide a linearize model of the FWT

at a specific operating point.

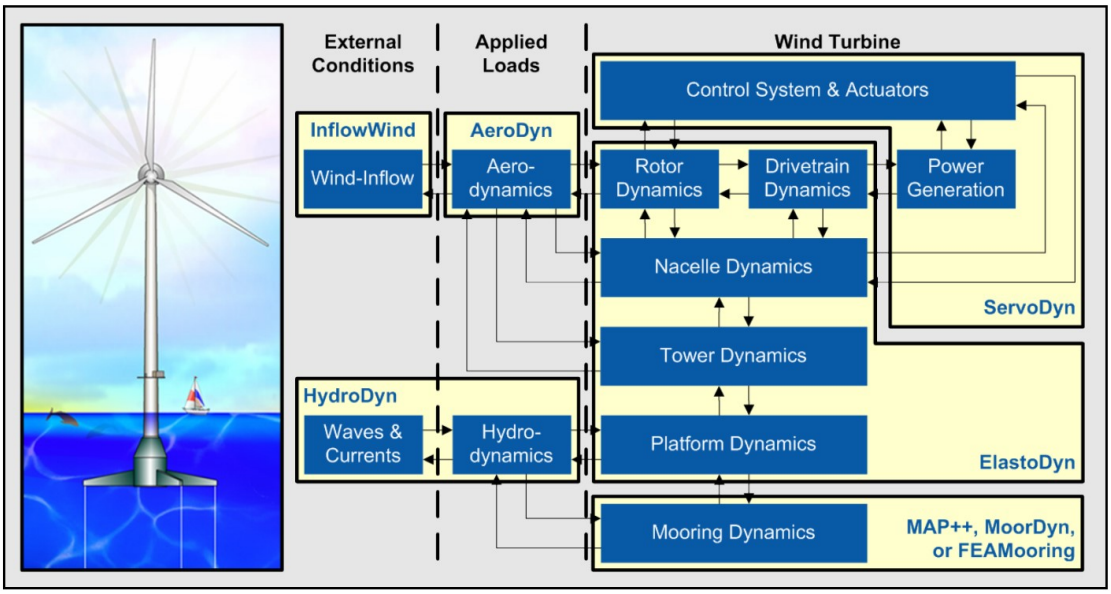

Figure 1.11 – FAST structure for floating wind systems (B. Jonkman and J. Jonkman 2016).

The control system can be integrated in the FAST simulation environment. The wind turbine actuators (blade pitch, generator torque, yaw drive and high-speed shaft brake) can be controlled by a dynamic link library (DLL) file or by interfacing with SIMULINK (Hazim Namik 2012). As a well-known simulation tool for control design, SIMULINK allows to develop the control scheme with high flexibly. The FAST software has the ability to be linked with SIMULINK through a s-function: this offers a convenient way to design control in the SIMULINK environment while using the nonlinear model described by FAST. Figure 1.12 displays the structure of control/system co-simulator: it is composed of FAST model (green box) that contains s-function with equations of motions and, in SIMULINK, the controllers providing the adapted signals.

1.4.2 5MW spar-buoy floating wind turbine model

In this study, the "NREL offshore 5MW OC3-Hywind" floating wind turbine model from the FAST software will be used for all the simulations. This model is based on the NREL offshore 5MW wind turbine (J. Jonkman 2010; J. Jonkman, Butterfield, et al. 2009), which is a well-known turbine and widely used in the research field of wind turbine, the main properties of this wind turbine being displayed in Table 1.1.
The platform applied to this FWT model is the spar-buoy concept and has been developed by Statoil of Norway on the Offshore Code Comparison Collaboration (OC3) project (Passon et al.

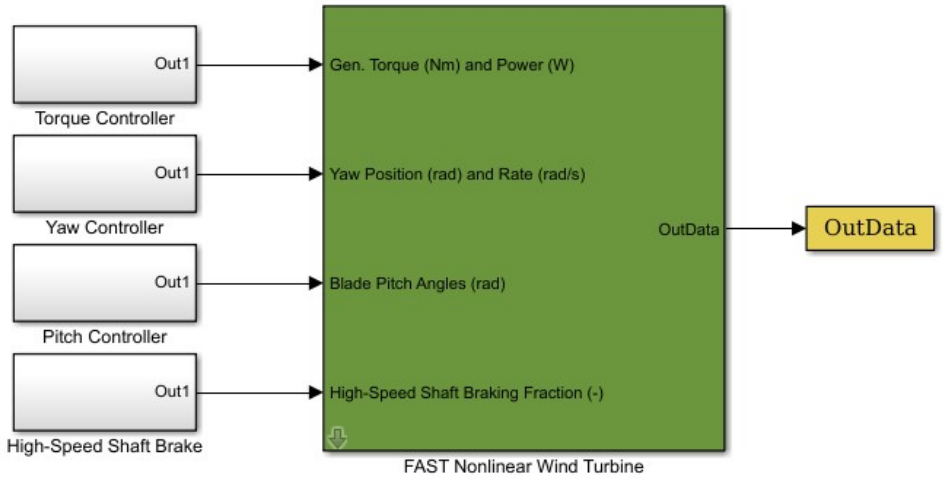

Figure 1.12 – Model and control scheme using FAST code (green box) in MATLAB/SIMULINK environment.

Description	Value
Cut-in, rated, cut-out wind speed	3 m/s, 11.4 m/s, 25 m/s
Rotor diameter	126 m
Hub diameter	3 m
Hub height	90 m
Rated power	5 MW
Rated rotor speed	12.1 rpm
Rated generator speed	1173.7 rpm
Rated generator torque	43,093.55 N·m
Minimum blade pitch setting	0 °
Maximum blade pitch setting	90 °
Maximum blade pitch rate	8 °/s

Table 1.1 – Properties of the NREL 5MW wind turbine (J. Jonkman, Butterfield, et al. 2009).

2007); it is known as "Hywind". Such concept has been chosen because of the simplicity in design, good stability and comparatively easy to implement in practice. Notice that the original Hywind spar-buoy is equipped by a 2.3-MW wind turbine. In order to support the NREL 5MW wind turbine, Jason Jonkman of NREL has adapted slightly the properties of the floating structure. Table 1.2 summarizes the main properties of the platform. Figure 1.13 illustrated the NREL 5MW OC3-Hywind floating wind turbine and the main dimensions of the spar platform.

Parameters	Value
Depth to platform base below still water level (SWL)	120 m
Elevation to platform top above SWL	10 m
Platform diameter above taper	6.5 m
Platform diameter below taper	9.4 m
Platform mass	7,466,330 kg

Table 1.2 – Properties of OC3-Hywind spar-buoy platform (J. Jonkman 2010).

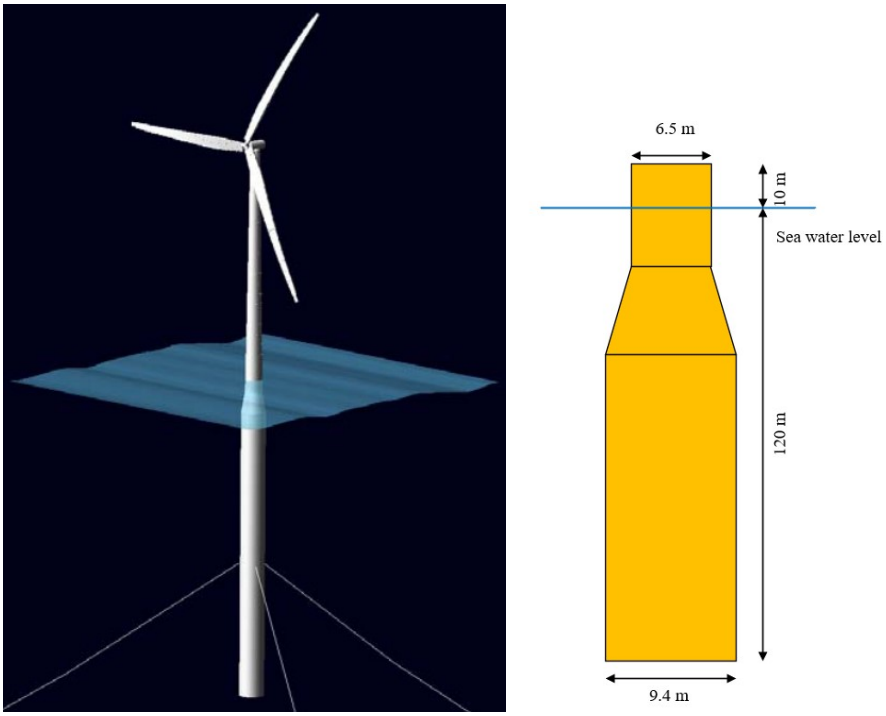

Figure 1.13 – **Left**. Illustrations NREL 5MW OC3-Hywind floating wind turbine (J. Jonkman 2010). **Right.** Main dimensions of OC3-Hywind spar-buoy platform.

1.4.3 Performance indicators

Different kinds of performance indicators are used in the sequel to precisely compare the controllers, it is the main way to have accurate comparison between the proposed control approaches. The objective being the evaluation of the controllers efficiency, the idea consists in evaluating the amount of produced power, the global behaviour of the FWT (motions, structure loads,...).

The first indicators are the root mean squares (RMS) of the power output, rotations and motions of the turbine and floating platform respectively. These RMS values allow to check the quality of the tracking (power/rotation speed) and the limited motions of the FWT.

The second indicators are the fatigue damage equivalent loads (DEL) that are used to evaluate the lifetime of the key components; such indicators are calculated by the post processing code Mlife (Gerber and M. Buhl Jr 2012).

Finally, the variation (VAR) of the blade pitch angle evaluates the activity of the blade pitch actuator: intensive action on blade pitch angle implies high energy consumption and could also reduced the lifetime of the actuator. Recall that VAR of a function Y (B. Wang et al. 2014) reads as

$$\mathrm{VAR}[p,q] = \sum_{i=p}^{q} |Y_{i+1} - Y_i|, \tag{1.14}$$

with $[p, q]$ the interval of sampled system output.

To summarize, the performance indicators are divided into the following categories:
Power, rotor speed regulation and motions of floating platform. The smaller the values, the better the performances.

- RMS of generator power error with respect to rated power (5 MW);
- RMS of rotor speed error with respect to the rated rotor speed (12.1 rpm);
- RMS of platform roll and its rate;
- RMS of platform pitch and its rate;
- RMS of platform yaw and its rate;

Fatigue loads of key components. The lower the value means the lower fatigue load of corresponding component.

- DEL of tower base (TB) fore-aft moment;
- DEL of tower base (TB) side-to-side moment;
- DEL of tower base (TB) torsional moment;

- DEL of blade root (BR) flap-wise moments;
- DEL of blade root (BR) edge-wise moments;
- DEL of fair-lead force (FF) of mooring lines;
- DEL of anchor force (AF) of 3 mooring lines.

Activity of blade pitch actuator. A high value implies its frequent use and is a key-indicator in order to detect, for example, chattering when sliding mode based control law is used.

- VAR of blade pitch angle.

1.5 Conclusions

This chapter has described the modeling of a FWT system, the simulation system and the analysis of performances. Firstly, the coordinate system is established. Physical models of power capture and drive train system are introduced. Then, a brief explanation of hydrodynamics of the floating structure is given. For the control design point of view, the linearized model of FWT is introduced and compared with the FAST nonlinear model. Finally, FAST software used in the sequel for the simulations of a 5 MW spar-buoy FWT is introduced, and performance indicators are defined.

Chapter 2

Collective blade pitch control of floating wind turbines

Contents

2.1 Introduction

The main objectives of controlling a traditional onshore wind turbine in Region III are to ensure a rated production of electrical power. In order to meet these objectives, many control strategies have been proposed (Menezes Novaes, Araújo, and Bouchonneau Da Silva 2018). However, these control algorithms can not be directly applied to the floating wind turbines due to the introduction of the floating platform: the dynamics of floating platform, particularly the platform pitch motion must

be taken into consideration in order to avoid the negative damping problem (Skaare et al. 2007) that leads to instability (as detailed in General Introduction). Thus, specific control algorithms for FWT must be proposed.

Recalling the General Introduction, the main control objectives of FWT in Region III are to maintains a rated power meanwhile reducing the platform pitch motion (J. Jonkman, Butterfield, et al. 2009). Many works have been done during the last decade on this problem. Linear control based on collective blade pitch (CBP) strategy (control of the three blades pitch angles by a single control command) such as GSPI controller (J. Jonkman 2008a), linear quadratic regulator and linear parameter-varying controllers (Bagherieh and Nagamune 2015), model predictive control and feedforward control (Schlipf, Pao, and Cheng 2012; Schlipf, Simley, et al. 2015). Most control approaches are based on linearized models of FWT (see previous chapter) that are derived from FAST software around an operating point depending especially on the wind and rotor speed. Consequently, the parameters of the controllers (that are mostly linear ones) must be tuned in different operating points to keep high performances; this tuning process has a cost and can be fastidious. A solution is the use of nonlinear control algorithms that have larger operating domains. In (Sandner et al. 2012; Schlipf, Sandner, et al. 2013; Raach et al. 2014; Homer and Nagamune 2018), nonlinear control strategies have been applied based on nonlinear models.
Due to the fact that

- the FWT system is highly nonlinear, uncertain and perturbed;
- the system modeling is not well-known and can be viewed, over a large operating domain, as a “black box”,

high order sliding mode control algorithms (Y. Shtessel et al. 2014; Cruz-Zavala and J. Moreno 2016) combined with gain/parameter adaptation laws (Yuri Shtessel, Taleb, and Plestan 2012; Tahoumi, Plestan, et al. 2019; S. Gutierrez et al. 2020) are well adapted. Such control algorithms are efficient even if the knowledge on the models is very limited and they are robust versus uncertainties and perturbations. In the sequel, the main contributions include

- the control problem statement of FWT in the Region III;
- the introduction of HOSM (super-twisting (Levant 1993) and homogeneous based control (Cruz-Zavala and J. Moreno 2016)), the gain/parameter adaptation algorithms and a new version of gain adaptation law for the super-twisting algorithm;

- the application of the adaptive HOSM solutions to the FAST nonlinear model according to different scenarios;

- the analysis and comparison of different adaptive HOSM approaches with respect to baseline GSPI control (J. Jonkman 2008a).

2.2 Control problem statement

Recalling that the FWT admits 4 operating regions (see Subsection *Operating regions* in General Introduction), this work is focused on the control problems in the Region III (also know as above-rated region). For the FWT system, the control problems in the considered region are firstly, the regulation of the power output at its rated value P_0, preventing an overload so as to protect the electric machine and the mechanical structure. Secondly, due to the additional DOFs introduced by the floating platform, the platform motion, especially the platform pitching, must be taken into consideration in order to avoid the negative damping (Skaare et al. 2007); as conclusion, the platform pitch motion must be reduced.

In the sequel, it is supposed that the FWT is face the wind. The problem of FWT orientation control is not considered here. Then, suppose that the FWT turbine is face the wind and the generator torque is fixed at its rated Γ_{g0} [1]. So the power (P) regulation is turned into rotor speed (Ω_r) regulation according to the relation between the power, the generator torque and the rotor speed

$$P = n_g \Gamma_{g0} \Omega_r$$

where n_g the gear box ratio. Therefore, the control objectives of the FWT in Region III can be described as the following ones:

- regulation of the rotor speed Ω_r at its rated value Ω_{r0}, with $\Omega_{r0} = \dfrac{P_0}{n_g \Gamma_{g0}}$, P_0 being the rated power;

- reduction of the platform pitch motion, *i.e.* cancellation of the platform pitch velocity $\dot{\varphi}$.

From the reduced linearized models (1.9)-(1.11) (Section 1.3.1), the dynamics of rotor speed Ω_r and platform pitch velocity $\dot{\varphi}$ directly depend on the CBP angle β_{col} that is viewed as the control input. By this way, one concludes that the relative degree of the system with Ω_r or $\dot{\varphi}$ as output, is equal to 1. Furthermore, the two control objectives have to be achieved by a single control input; obviously,

1. In the next chapter, a generator will be supposed to equip the turbine. Then, its torque will be able to vary.

it is an under-actuated problem.

Existing solutions are, as mentioned in General Introduction, mainly based on the following ideas to solve this problem: the first solution is to use the detuned GSPI controller (Larsen and Hanson 2007; J. Jonkman 2008a) such that the natural frequency of closed-loop system is lower than the platform pitch natural frequency; this approach successfully attenuating the platform pitch motion but at a cost of larger power fluctuation. The second solution is based on modern control theory, such as LQR (Hazim Namik, Karl Stol, and J. a. Jonkman 2008; Christiansen, Knudsen, and T. Bak 2011; Christiansen, Knudsen, and T. Bak 2014) and H_∞ (Bakka and Karimi 2012; Bakka and Karimi 2012; X. Li and Gao 2015; Hara et al. 2017). The third solution is to use IBP control to increase the number of the inputs (Hazim Namik and Karl Stol 2010; H. Namik and K. Stol 2014; Lemmer, Raach, et al. 2015; Suemoto, Hara, and Konishi 2017); thus, multiple control objectives can be achieved. However, these solutions induce a great tuning effort due to the fact that the control is based on numerous linearized models, each model being obtained for an operating point. Moreover, the IBP control significantly increases the use of blade actuator comparing with the collective one, and is not completely implemented in commercial wind turbines (Menezes Novaes, Araújo, and Bouchonneau Da Silva 2018).

The solution used in this study is inspired by the work of (Lackner 2009; Lackner 2013; Cunha et al. 2014) and takes advantage from physical features of floating wind turbines. Consider that the desired rotor speed Ω_r^* is a function of platform pitch velocity

$$\Omega_r^* = \Omega_{r0} - k\dot{\varphi} \tag{2.1}$$

with k a positive constant. In this case, the desired rotor speed is no longer set at its rated value, but at a value varying with the platform pitch velocity (Lackner 2009; Lackner 2013). Such reference is based on the trade-off between rotor speed and platform pitch motion.

As shown in Figure 2.1, suppose that the platform is pitching forward/against the wind (notice that when the platform is pitching forward, $\dot{\varphi} < 0$. Then, the reference Ω_r^* is calculated higher than the rated: thanks to the control, the rotor speed increases with aerodynamic torque so as to track the reference. Meanwhile, the aerodynamic thrust captured by the rotor increases, which prevents the platform pitching forward, *i.e.* $|\dot{\varphi}|$ reduces. Thereby, according to (2.1), the rotor speed reference Ω_r^* converges to its rated value Ω_{r0}. On the contrary, when the platform is pitching downwind/with the wind, the control reduces the rotor speed since the reference rotor speed is lower than the rated one. At the same time, the aerodynamic thrust on the rotor decreases that stops the platform pitch downwind. Likewise, $|\dot{\varphi}|$ reduces and Ω_r^* converges to Ω_{r0}.

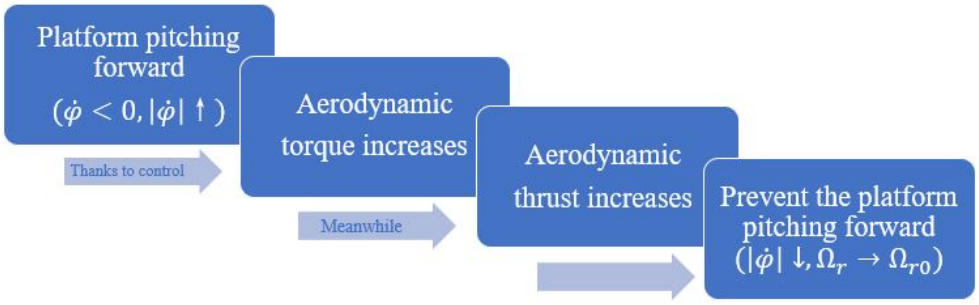

Figure 2.1 – Relationship between rotor speed and platform pitch motion under the control action.

2.3 Sliding mode control

The floating wind turbine system is a highly perturbed and uncertain nonlinear system, not only due to the elasticity of the structure (*e.g.* tower, blade, ...), but also given that the wind and waves can influence the system. Hence, the linear controllers such as GSPI (J. Jonkman 2008a; Wakui, Yoshimura, and Yokoyama 2017), LQR (Hazim Namik, Karl Stol, and J. a. Jonkman 2008; Christiansen, Knudsen, and T. Bak 2011), H_∞ (Bakka and Karimi 2012; Bakka and Karimi 2012; X. Li and Gao 2015; Hara et al. 2017) and ... are based on a linear model obtained around a given operating point; as a consequence, they have reduced operating ranges. Since the gains of linear control guarantee the expected performances only around the operating point, several sets of gains must be tuned for a set of operating points that implies a great effort of tuning.

> The idea of this work is to show that nonlinear controllers with a *single* set of parameters are efficient over a large operating domain; thanks to this fact, the advantage of the proposed nonlinear control approaches is the tuning effort reduction while maintaining high level performances.

In order to develop robust nonlinear control strategies, sliding mode control (SMC) (V. Utkin 1977) is considered: it is a well-known nonlinear control strategy with properties of robustness, accuracy and finite time convergence. In fact, the standard first order SMC can be easily implemented; however, the control law of standard SMC is discontinuous. Due to the discontinuous term of the control input, chattering phenomenon (V. Utkin, Guldner, and J. Shi 1999) appears and can damage the physical components such as blade pitch actuators in this study. High order sliding mode (HOSM) (Y. Shtessel et al. 2014; Cruz-Zavala and J. Moreno 2016) control can reduce the chattering while keeping robustness and improving accuracy. Two kinds of HOSM controllers, super-twisting controller (Y. Shtessel et al. 2014) and homogeneity based (Cruz-Zavala and J. Moreno 2016) are presented in the sequel.

Furthermore, considering that system (1.9) is a simplified model with only 2 DOFs enabled, such simplified model can not describe all the characteristics of the system; the model uncertainties and the perturbations must be taken into account. As a consequence, the gains of the controllers should be sufficiently large to counteract the uncertainties/perturbations effects; it means that the gains are tuned in order to ensure high performances, *i.e.* even in the *worst* case. However, when the perturbations became relatively small, the gain is finally too large, that leads to unnecessary large variations of control (more energy consumption) and reduces the control performances. Therefore, adaptation strategies for super-twisting (through the gains) and for homogeneity based controller (through exponent parameter) are used and described respectively in the sequel.

2.3.1 Recalls

Consider the following system

$$\begin{aligned} \dot{z} &= f(z,t) + g(z,t)\upsilon \\ y &= c(z,t) \end{aligned} \tag{2.2}$$

with $z \in Z \subset \mathbb{R}^n$ the state and $\upsilon \in U \subset \mathbb{R}$ the control input. $f(z,t)$ and $g(z,t)$ are the bounded unknown nonlinear functions, and y the system output. Define the so-called sliding variable $S = S(z,t)$ such that, once $S = 0$, then $y \to 0$.

The idea of SMC is to design the control input υ such that the sliding variable $S(z,t)$ is forced to reach the sliding surface $S(z,t) = 0$ in a finite time, in spite of uncertainties and perturbations. Once $S(z,t) = 0$, the system trajectories are evolving on this surface: then y goes towards 0. Notice that the sliding variable $S(z,t)$ is defined according to control objective y and the relative degree. Assume that

Assumption 1. *The relative degree ρ of system (2.2) with respect to S is constant and known with $\rho \geq 1$. Then, one gets*[2]

$$S^{(\rho)} = a(z,t) + b(z,t)\upsilon. \tag{2.3}$$

■

In the sequel, ρ will be equal to 1 or 2.

Assumption 2. *Functions $a(z,t)$ and $b(z,t)$ are unknown and bounded such that*

$$|a| \leq a_M,\ 0 < b_m \leq b \leq b_M \tag{2.4}$$

$\forall z \in Z$, $t > 0$, a_M, b_m and b_M being positive constants. ■

2. In the sequel, given $k \in \mathbb{N}$, $S^{(k)}$ is the k-th time derivative of S.

Suppose that $\rho = 1$: one has

$$\begin{aligned} \dot{S} &= \underbrace{\frac{\partial S}{dt} + \frac{\partial S}{dz} f(z,t)}_{a(z,t)} + \underbrace{\frac{\partial S}{dz}(z,t)}_{b(z,t)} \upsilon \\ a(z,t) &= a_0(\cdot) + a_u(\cdot) \\ b(z,t) &= b_0(\cdot) + b_u(\cdot) \end{aligned} \tag{2.5}$$

with $a_0(\cdot)$ and $b_0(\cdot)$ being known functions, $a_u(\cdot)$ and $b_u(\cdot)$ being unknown and bounded uncertainties The control objective is fullfilled by determining υ such that system (2.5) is stabilized at 0 in spite of uncertainties on a and b. A solution is to define the control input υ based on the standard first order sliding mode control (V. I. Utkin 1992; V. Utkin, Guldner, and J. Shi 1999) that reads as

$$\upsilon = -k \cdot \text{sign}(S) \tag{2.6}$$

with k the controller gain. Derived from Lyapunov approach (V. Utkin, Guldner, and J. Shi 1999), a first order sliding mode can be established, (*i.e.* the system trajectory converges to $S = 0$ in a finite time), if the sliding condition (with $\eta > 0$)

$$S\dot{S} \leq -\eta|S| \tag{2.7}$$

is satisfied. A sliding mode can be established if the controller gain satisfies

$$k > \frac{a_M + \eta}{b_m} \tag{2.8}$$

Then tuning of η allows to act on the convergence time t_c that is bounded by

$$t_c < \frac{S(0)}{\eta}. \tag{2.9}$$

Although the standard first order sliding mode control can achieve the control objective, the first derivative of S is discontinuous due to the discontinuity of the sign function that induces the so-called chattering phenomenon (V. Utkin, Guldner, and J. Shi 1999) that degrades the control performances. Many studies have been done in order to reduce this phenomenon, while keeping the original main characteristics (robustness, convergence in finite time). A solution is to use high order sliding mode (HOSM) algorithms (Y. Shtessel et al. 2014; Cruz-Zavala and J. Moreno 2016): the task is to keep a smoother dynamics of S by guaranteeing the high order derivatives of S equal to zero. For the r-th order sliding mode, one has (Perruquetti and Barbot 2002)

$$S = \dot{S} = \ddot{S} = ... = S^{(r-1)} = 0. \tag{2.10}$$

Among the most popular HOSM algorithms, super-twisting (Levant 1993) and homogeneity based control are applied in this work.

Super-twisting control (Levant 1993)

The control υ can be applied only for systems (2.3) with $\rho = 1$. Then, the control reads as (Levant 1993)

$$\begin{aligned} \upsilon &= -k_1|S|^{\frac{1}{2}} \cdot \text{sign}(S) + \omega \\ \dot{\omega} &= -k_2 \cdot \text{sign}(S) \end{aligned} \tag{2.11}$$

with k_1 and k_2 the controller gains. One of the main advantage of STW is that it only depends on the sliding variable S (not on $\dot{S}$ as most of the second order sliding mode controllers-see for example the twisting algorithm (Levant 1993)). A key point for the tuning of STW is the estimation of the minimum values of the controller gains allowing to ensure the establishment of a second order sliding mode, *i.e.*

$$S, \dot{S} \rightarrow 0 \tag{2.12}$$

From the knowledge of the bounds defined in Assumption 2, a second order sliding mode can be established in a finite time with the controller (2.11) if (Levant 1993)

$$k_1 > \frac{a_M}{b_M}, \; k_2^2 \geq \frac{4a_M}{b_m^2} \cdot \frac{b_M}{b_m} \cdot \frac{k_1 + a_M}{k_1 - a_M} \tag{2.13}$$

In practice, the super-twisting controller ensures, in a finite time, the establishment of a "real" second order sliding mode (Levant 1993) such that

$$|S| < \mu_1 T_e^2, \quad |\dot{S}| < \mu_2 T_e \tag{2.14}$$

with T_e the control sampling time, and μ_1 and μ_2 positive constant. It is established that the sliding mode appears in a finite time with sufficiently large gains k_1 and k_2. However, in practice, the bounds of uncertainties and perturbations are difficult to determine; furthermore, even if they are determined, they are often over-estimated that degrades the control performances. A solution is the use of adaptive gains: it allows to dynamically increase the gains when accuracy is not sufficient, and to dynamically reduce them when control objectives are reached. Such gain adaptation laws will be detailed in the sequel.

Homogeneous controller (Cruz-Zavala and J. Moreno 2016)

Another solution to establish HOSM is based on Lyapunov functions and proposed in (Cruz-Zavala and J. Moreno 2016). The control υ reads as [3]

$$\begin{array}{rcl} \upsilon & = & -k_\rho \lceil S_\rho \rfloor^0 \\ S_i & = & \lceil S^{(i-1)} \rfloor^{\frac{r_1}{r_i}} + k_{i-1}^{\frac{r_1}{r_i}} S_{i-1}, \quad i = 2, \cdots, \rho \end{array} \tag{2.15}$$

with relative degree $\rho \geq 2$, $[r_1, \cdots, r_\rho] = [\rho, \rho-1, \cdots, 1]$, $S_1 = S$ and $(k_1, \cdots, k_\rho)$ the controller gains. As previously, in order to ensure the establishment of a ρ^{th}-order sliding mode, the gains should fulfill the following conditions

- $\rho = 2$. The gain k_1 is arbitrarily fixed positive and k_2 is derived from

$$b_m k_2 - a_M \quad \geq \quad \gamma_1 k_1^2 \tag{2.16}$$

- $\rho > 2$. The gain k_1 is arbitrarily fixed positive and k_i is derived from

$$\begin{array}{rcl} k_i & = & \gamma_{i-1} k_1^{\frac{\rho}{\rho-(i-1)}}, \quad \forall i = 2, \cdots, \rho-1 \\ b_m k_\rho - a_M & \geq & \gamma_{\rho-1} k_1^\rho \end{array} \tag{2.17}$$

with γ_{i-1}, $(i = \{2, 3, \cdots, \rho-1\})$ the parameters that are calculated to guarantee the time derivative of Lyapunov function negative definite. Table 2.1 shows the values of γ_{i-1} for $\rho = 2, 3, 4$.

Table 2.1 – Parameters γ_{i-1} (Cruz-Zavala and J. Moreno 2016).

ρ	Parameters
2	$\gamma_1 = 1.26$
3	$\gamma_2 = 1.26$, $\gamma_1 = 1.26$
4	$\gamma_3 = 1.26$, $\gamma_2 = 1.26$, $\gamma_1 = 1.26$

In current study the case $\rho = 2$, is under interest. One gets $r_1 = 2$, $r_2 = 1$

$$\begin{array}{rcl} S_1 & = & S \\ S_2 & = & \lceil \dot{S} \rfloor^2 + k_1^2 S \end{array} \tag{2.18}$$

and the control υ reads as

$$\begin{array}{rcl} \upsilon & = & -k_2 \cdot \text{sign}(S_2) \\ & = & -k_2(|\dot{S}|^2 \text{sign}(\dot{S}) + k_1^2 S) \end{array} \tag{2.19}$$

Although HOSM can be established by homogeneous controller in a finite time, the controller gains of such method are also overestimated as the STW in practice, which induces high actuator energy

3. In the sequel, $\lceil S \rfloor^n = |S|^n \text{sign}(S)$ with $n \in \mathbb{N}$.

consumption. Moreover, due to the sign function used in the control, another drawback, chattering phenomenon can appear. This phenomenon is further magnified by the overestimated gains (Obeid et al. 2018).

In the sequel, an adaptive solution of (2.15) is given by introducing a time varying exponent parameter $\bar{\alpha}$. By this way, the closed-loop accuracy can be ensured with less both chattering and energy assumption.

2.4 Adaptation algorithms

As detailed in the previous section, the choice of sufficiently large gains (versus uncertainties and perturbations) allows to guarantee the establishment of high order sliding mode. However, in many applications, the bounds of uncertainties and perturbations are difficult to determine, that is the case for FWT systems. As a consequence, the gains are often over-estimated. A solution consists to use adaptive gains or parameters with an intuitive approach: the accuracy of the closed-loop system versus the control objectives is checked and an action on the gains/parameters is made in order to guarantee a sufficient accuracy and an attenuated chattering. In this section, both such approaches are presented knowing that one of main objectives is to the limitation of the chattering.

Gain adaptation

This approach is applied to the STW controller (2.11), the controller gains k_1 and k_2 being dynamically adapted with respect to the uncertainties and perturbations. Namely, the gains are time-varying and are reduced if the accuracy is good, increased if accuracy falls (Y. Shtessel et al. 2014; Cruz-Zavala and J. Moreno 2016; Yuri Shtessel, Taleb, and Plestan 2012; S. Gutierrez et al. 2020). This way allows to reduce the amplitude of the chattering since the gains are not overestimated but adjusted to the uncertainties and perturbations. Based on this gains adaptation approach, two adaptive control laws will be used in the sequel

- the first one is the adaptive super-twisting (ASTW) control proposed by (Yuri Shtessel, Taleb, and Plestan 2012);

- the second one is the "simplified" version of adaptive super-twisting (SAST) control, that is firstly proposed in (S. Gutierrez et al. 2020).

Exponent adaptation

This approach is based on the homogeneous controller (2.15). Quite different from the previous gain adaptation, the adaptation here is achieved by introducing a parameter $\bar{\alpha}$ on the exponent terms of (2.15)

$$\upsilon = -k_\rho \lceil S_\rho \rfloor^{\bar{\alpha}} \tag{2.20}$$

with the parameter $\bar{\alpha}$ adapted with respect to the closed loop accuracy. When the trajectory of the system is far from the origin, the controller must be robust. Then, $\bar{\alpha}$ is fixed at 0: it is equivalent to HOSM controller increasing the robustness and the accuracy of the system. When the trajectory of the system is close to the origin, a smoother linear control can be applied by varying $\bar{\alpha}$ from 0 to 1. In this case, the controller is linear that reduces the chattering effect. It finds a trade-off between accuracy and energy consumption by directly acting on terms depending on sign functions (Tahoumi, Ghanes, et al. 2018; Tahoumi, Plestan, et al. 2018b; Tahoumi, Plestan, et al. 2018a; Tahoumi, Plestan, et al. 2019). In the sequel, the parameter adaptation controller selected in this work is the homogeneity based controller with varying exponent parameter (HCVP) (Tahoumi, Plestan, et al. 2019).

2.4.1 Adaptive super-twisting (Yuri Shtessel, Taleb, and Plestan 2012)

Thanks to the adaptation law, the controller gains k_1 and k_2 in (2.11) must be dynamically adapted to the "just sufficient" values in spite of the uncertainties and perturbations. Furthermore, they must ensure the convergence of the closed-loop system and reduce the chattering effect. Recall that the control design must require no information on the bounds of uncertainties and perturbations. Following all these features, the adaptation law is defined by (Yuri Shtessel, Taleb, and Plestan 2012)

$$\begin{aligned} \dot{k}_1 &= \begin{cases} \omega\sqrt{\frac{\chi}{2}}\text{sign}(|S|-\mu) & \text{if } k_1 > k_m \\ m & \text{if } k_1 < k_m \end{cases} \\ k_2 &= \epsilon k_1 \end{aligned} \tag{2.21}$$

where k_m, ϵ, ω, χ, μ and m are positive constants, $k_1(0) > k_m$. The idea of the gain adaptation is the following

- if $|S|$ is small enough versus the accuracy defined by μ, *i.e.* $\text{sign}(|S|-\mu) < 0$, it means that the controller is efficient: the gain can be reduced. $\dot{k}_1$ being negative, k_1 decreases;

- if $|S|$ is larger than the desired accuracy, *i.e.* $\text{sign}(|S|-\mu) > 0$, it could be due to the fact that the gain is too small versus uncertainties and perturbations. Then, $\dot{k}_1$ being positive, k_1 increases;

- the parameter k_m is taken as a very small value and ensures the positiveness of k_1.

Notice that the ASTW controller can be applied without any knowledge of $a(z,t)$ and $b(z,t)$.

2.4.2 Simplified adaptive super-twisting (S. Gutierrez et al. 2020)

As detailed in the previous section, the ASTW combines second order sliding mode algorithm and adaptive law that successfully reduces the chattering and keeps a high accuracy. Furthermore, this controller requires no information on the uncertainties and perturbation, and the adaptation law is intuitive and easily implementable. Nevertheless, the major drawback of previous algorithm is its numerous tuning parameters (k_m, ϵ, ω, χ, μ and m). Furthermore, there is no tuning methodology. A first simplified adaptive super-twisting has been proposed in (S. V. Gutierrez et al. 2019) that reduced the number of tuning parameters at 2. However, the key problem with this approach is that the gains tuning process is not easy and the behaviour of the gain is not easily predictable (the adaptation law is not intuitive). Therefore, a new adaptive version of super-twisting algorithm with an intuitive adaptation law and a reduced number of parameters SAST is proposed in this work.

Assumption 3. *The relative degree ρ is equal to 1. S-dynamic reads as*

$$\dot{S} = a_0(\cdot) + b_0(\cdot)u + \varrho(z,t) \tag{2.22}$$

with $a_0(\cdot)$ and $b_0(\cdot)$ known functions, and $\varrho(z,t)$ the parametric uncertainties and external perturbations. ■

Assumption 4. *The first time derivative of the perturbation ϱ is bounded with unknown boundary δ, i.e. there exists $\delta > 0$, such that $\dot{\varrho} \leq \delta$.* ■

Consider the following state feedback u defined as

$$u = \frac{1}{b_0(\cdot)}\left(-a_0(\cdot) + v\right) \tag{2.23}$$

that linearizes the sliding variable dynamics when no perturbation/uncertainty is acting, and the "new" control input v given by

$$\begin{aligned} v &= -2L(t)|S|^{\frac{1}{2}}\text{sign}(S) + w \\ \dot{w} &= -\frac{L^2(t)}{2}\text{sign}(S) \end{aligned} \tag{2.24}$$

The controller (2.24) is based on the STW algorithm where $L(t)$ is a time-varying gain that will be tuned thanks to an adaptation law. Then, under the control (2.23)-(2.24), it follows that the

S-dynamics reads as (S. Gutierrez et al. 2020)

$$\dot{S} = -2L(t)|S|^{1/2}\text{sign}(s) + w + \varrho \tag{2.25}$$

that can be also written as

$$\begin{aligned} \dot{S} &= -2L(t)|S|^{1/2}\text{sign}(s) + \bar{w} \\ \dot{\bar{w}} &= -\frac{L^2(t)}{2}\text{sign}(s) + \dot{\varrho} \end{aligned} \tag{2.26}$$

Notice that controller (2.24) only depends on the gain $L(t)$, which simplifies its tuning. The idea now is to propose an adaptation law that dynamically changes the control gain $L(t)$ until a real second order sliding mode is established (*i.e.* (2.14) is fullfilled).

The main methodological result of the "simplified" adaptation law is formulated as following (S. Gutierrez et al. 2020)

$$\dot{L} = \begin{cases} L\left(|S| - \mu\right), & \text{if } L > L_m \\ L_m, & \text{if } L \leq L_m \end{cases} \tag{2.27}$$

where μ and L_m are positive constants, $L(0) > L_m$. The parameter L_m is introduced in order to get only positive values for $L(t)$, and can be chosen arbitrarily small. The parameter μ is tuned with respect to the desired accuracy of the closed-loop system. Notice that only two parameters are required and only the choice of μ is crucial.

Proof

Consider the STW algorithm with perturbation term

$$\begin{aligned} \dot{z}_1 &= -2L(t){z_1}^{1/2}\text{sign}(z_1) + z_2 \\ \dot{z}_2 &= -\frac{L(t)^2}{2}\text{sign}(z_1) + \gamma(t, z) \end{aligned} \tag{2.28}$$

that has the same form as (2.25). Now, in order to represent system (2.28) in a convenient form for Lyapunov analysis, consider the following change of coordinates

$$\xi_1 = {z_1}^{1/2}\text{sign}(z_1), \qquad \xi_2 = \frac{z_2}{L(t)} \tag{2.29}$$

with $L(t) > 0$. Then, from system (2.28), one gets

$$\begin{aligned}\dot{\xi}_1 &= \frac{L(t)}{2\xi_1}(-2\xi_1 + \xi_2)\\ \dot{\xi}_2 &= \frac{L(t)}{2\xi_1}\left(-\xi_1 + \frac{2\xi_1\gamma(t,\xi)}{L^2(t)}\right) - \frac{\dot{L}(t)}{L(t)}\xi_2\end{aligned} \tag{2.30}$$

Then, the system (2.30) can be rewritten as

$$\dot{\xi} = \frac{L}{2\xi_1}\left\{(\mathbf{A} - \mathbf{S}_\infty^{-1}\mathbf{C}^T\mathbf{C})\xi + \frac{1}{L^2}\mathbf{D}\right\} - \frac{\dot{L}(t)}{L(t)}\mathbf{B}\mathbf{B}^T\xi \tag{2.31}$$

with

$$\xi = \begin{bmatrix}\xi_1\\ \xi_2\end{bmatrix},\ \mathbf{A} = \begin{bmatrix}0 & 1\\ 0 & 0\end{bmatrix},\ \mathbf{B} = \begin{bmatrix}0\\ 1\end{bmatrix}\ \mathbf{C} = \begin{bmatrix}1, & 0\end{bmatrix},$$

$$\mathbf{S}_\infty = \begin{bmatrix}2 & 1\\ 1 & 0\end{bmatrix},\ \ \mathbf{D}(t,\xi) = \begin{bmatrix}0\\ 2\xi_1\gamma(t)\end{bmatrix}$$

with $\mathbf{S}_\infty$ a symmetric and positive definite matrix solution of the algebraic Lyapunov equation $\mathbf{S}_\infty + \mathbf{A}^T\mathbf{S}_\infty + \mathbf{S}_\infty\mathbf{A} - \mathbf{C}^T\mathbf{C} = 0$. Consider the following Lyapunov candidate function

$$V_{(\xi,L)} = V_{(\xi)} + \frac{1}{2}(L(t) - L^*)^2 \tag{2.32}$$

with $V_{(\xi)} = \xi^T\mathbf{S}_\infty\xi$. Taking the time derivative of Lyapunov function along the trajectories of the system (2.31), it follows that

$$\begin{aligned}\dot{V}_{(\xi,L)} = \frac{1}{2\xi_1}&\left[-L(t)\xi^T\mathbf{S}_\infty\xi - L(t)\xi^T\mathbf{C}^T\mathbf{C}\xi + 2\xi^T\mathbf{S}_\infty\mathbf{D}\right]\\ &+ \dot{L}(t)\left[(L(t) - L^*) - \frac{2}{L(t)}\xi^T\mathbf{B}\mathbf{B}^T\xi\right]\end{aligned} \tag{2.33}$$

The function $V_{(\xi)}$ satisfies the following inequalities

$$\lambda_{min}(\mathbf{S}_\infty)||\xi||^2 \leq V_{(\xi)} \leq \lambda_{max}(\mathbf{S}_\infty)||\xi||^2 \tag{2.34}$$

where $\lambda_{min}(\mathbf{S}_\infty)$ and $\lambda_{max}(\mathbf{S}_\infty)$ are the minimum and maximum eigenvalues of the matrix $\mathbf{S}_\infty$ respectively; one gets

$$\xi_1 \leq \xi \leq \frac{V_{(\xi)}^{1/2}}{\lambda_{min}^{1/2}(\mathbf{S}_\infty)} \tag{2.35}$$

Consider the norm of the nonlinear term $2\xi^T\mathbf{S}_\infty\mathbf{D}$, and transformed the perturbation satisfies

$\mathbf{D}(t,\xi) \leq \delta\xi$ (J. A. Moreno 2009). Taking into account (2.33) and (2.34), one obtains

$$\begin{aligned}
\dot{V}_{(\xi,L)} &\leq \frac{1}{2\xi_1}\left[-L(t)V_{(\xi)} + 2\mathbf{S}_\infty\ \delta\xi\ ^2 - L(t)\xi^T\mathbf{C}^T\mathbf{C}\xi\right] \\
&\quad + \dot{L}(t)\left[(L(t)-L^*) - \frac{2}{L(t)}\xi^T\mathbf{B}\mathbf{B}^T\xi\right] \\
\dot{V}_{(\xi,L)} &\leq -\eta V_{(\xi)}^{1/2} - \frac{L(t)}{2}\xi_1 \\
&\quad + \dot{L}(t)\left[(L(t)-L^*) - \frac{2}{L(t)}\xi^T\mathbf{B}\mathbf{B}^T\xi\right]
\end{aligned} \tag{2.36}$$

with

$$\eta = \frac{L(t)-q}{2\lambda_{min}^{-1/2}(\mathbf{S}_\infty)}, \qquad q = \frac{2\delta\mathbf{S}_\infty}{\lambda_{min}(\mathbf{S}_\infty)}$$

By adding and subtracting the term $\kappa L(t) - L^*$ in (2.36), one obtains

$$\begin{aligned}
\dot{V}_{(\xi,L)} &\leq -\eta V_{(\xi)}^{1/2} - \frac{L(t)}{2}\xi_1 - \kappa L(t) - L^* + \kappa L(t) - L^* \\
&\quad + \dot{L}(t)\left[(L(t)-L^*) - \frac{2}{L(t)}\xi^T\mathbf{B}\mathbf{B}^T\xi\right]
\end{aligned} \tag{2.37}$$

Using Jensen's inequality

$$(a^q + b^q)^{1/q} \leq a + b, \quad q > 0$$

and choosing $a = V_{(\xi)}$, $b = (L(t)-L^*)^2$ and $q = \dfrac{1}{2}$, then one has

$$-\eta V_{(\xi)}^{1/2} - \kappa L(t) - L^* \leq -\iota V_{(\xi,L)}^{1/2} \tag{2.38}$$

with $\iota = min\,(\eta,\kappa)$. Taking into account (2.38), and assuming there exist positive constant L^* such that $L(t) - L^* < 0\ \forall t \geq 0$. In view of the above assumption, equation (2.37) can be reduced to the following

$$\dot{V}_{(\xi,L)} \leq -\iota V_{(\xi,L)}^{1/2} + \epsilon \tag{2.39}$$

with

$$\epsilon = -\frac{L(t)}{2}\xi_1 - L(t) - L^*(\dot{L}(t) - \kappa) - \frac{2\dot{L}(t)}{L(t)}\xi^T\mathbf{B}\mathbf{B}^T\xi$$

Next, through the study of ϵ and its sign, stability of the closed-loop system is analyzed. More precisely, the behavior of the time derivative of the Lyapunov function is analyzed. To ensure the stability of $\dot{V}_{(\xi,L)}$, consider the following cases.

Case 1. Suppose that $L(t) > L_m$, and $|S| - \mu > 0$. Then, $L(t)$ is increased until the second order slid-

ing mode is established. If $\kappa < L(t)(|S| - \mu)$, Then, ϵ is negative, and it follows that $\dot{V}_{(\xi,L)} \leq -\iota V_{(\xi)}^{1/2}$ with $\iota = min\,(\eta, \kappa)$.

Case 2. Suppose now $L(t) \leq L_m$ that implies $\dot{L}(t) = L_m$, and

$$\epsilon = -\frac{L(t)}{2}\xi_1 - L(t) - L^*(L_m - \kappa) - \frac{2L_m}{L(t)}\xi^T \mathbf{B}\mathbf{B}^T \xi \tag{2.40}$$

In this case, considering $\kappa = L_m$, which yields $\epsilon \leq 0$, then, the 2-sliding mode is established, one gets

$$\dot{V}_{(\xi,L)} \leq -\iota V_{(\xi,L)}^{1/2} \tag{2.41}$$

As soon as inequality (2.41) is fulfilled in finite-time, the SAST control law (2.27) drives the sliding variable S and is derivative to zero in finite time, that is estimated as

$$t_c \leq \frac{2V_{(\xi,L)}^{1/2}(0)}{\iota} \tag{2.42}$$

Thus, the states ξ_1 and ξ_2 converge to zero in finite-time. This implies that also the states z_1, z_2 will converge to zero in finite-time.

Case 3. Suppose that $L(t) > L_m$, and $|S| - \mu < 0$, that implies $L(t)$ is reducing in according to (2.27), then, the term ϵ becomes positive. Hence, in view of (2.39), $\dot{V}_{(\xi,L)}$ becomes sign indefinite. As soon as the state $|S|$ becomes greater than μ (this happens in finite time), the condition that defines Case 1 holds, i.e. it means that $L(t)$ shall increase in accordance with (2.27) that guarantee $\dot{V}_{(\xi,L)}$ is negative definite.

Academic example

Consider the uncertain system $\dot{S} = u + \varrho(t)$ with $\varrho(t)$ defined as

$$\varrho(t) = \begin{cases} 10\sin(2t) & \text{if } t \leq 50\ sec \\ 50\cos(2t) & \text{if } t > 50\ sec \end{cases}$$

The initial value of the sliding variable is defined as $S(0) = 5$. The control input u is defined as (2.23)-(2.24)-(2.27) with $a_0 = 0$ and $b_0 = 1$. Parameters of the controller have been tuned in order to get good behaviour and performances, *i.e.* $L_m = 0.005$, $\mu = 0.03$. Figure 2.2 displays the sliding variable $S(t)$. The efficiency of the proposed adaptation algorithm is described in Figure 2.3: the gain $L(t)$ increases until a sliding mode is established. Thus, the gain starts reducing. This gain reduction is reversed as soon as the sliding variable starts deviating from the vicinity of $S = 0$.

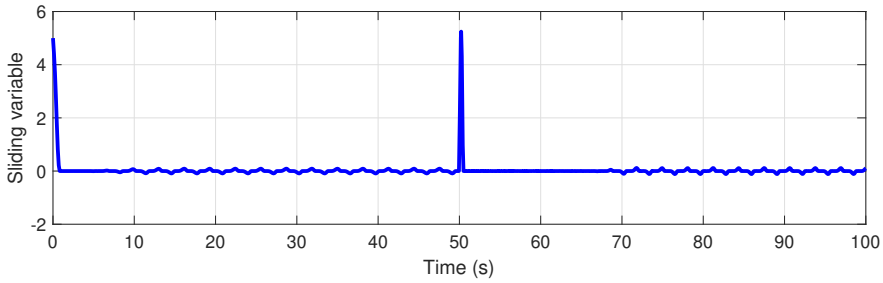

Figure 2.2 – Sliding variable $S(t)$ versus time (sec).

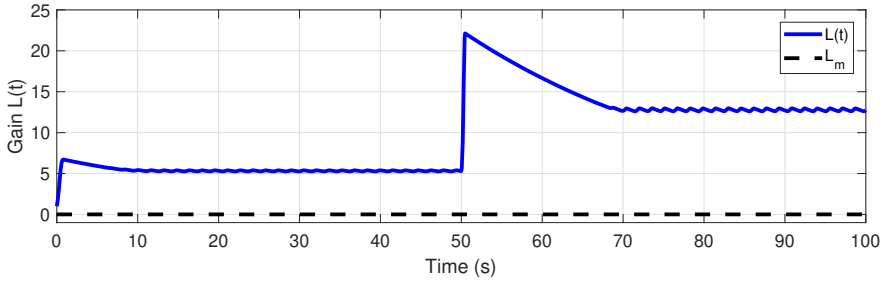

Figure 2.3 – Adaptive gain $L(t)$ versus time (sec).

2.4.3 Homogeneity based controller with varying exponent parameter (Tahoumi, Plestan, et al. 2019)

The approach has been very recently proposed by (Tahoumi, Plestan, et al. 2019) and is based on the homogeneous controller (2.15). The adaptation law is made by introducing a time varying exponent parameter $\bar{\alpha}$ such that the control law now reads as

$$\upsilon = -k_\rho \lceil S_\rho \rfloor^{\bar{\alpha}} \tag{2.43}$$

with k_ρ, S_ρ tuned as (2.15) and $\bar{\alpha} \in [0, 1]$ with the adaptive law

$$\bar{\alpha} = max(-\bar{\beta} \sum_{i=1}^{\rho} \frac{|S^{(i-1)}|}{|S^{(i-1)}| + \epsilon_{S_i}} + 1, 0) \tag{2.44}$$

with ϵ_{S_i} a positive constant and $\bar{\beta} > 1$ tuned by the user. The idea of the adaptation is the following

- if $|S|$ and its time derivatives are small enough, the exponent term $\bar{\alpha}$ is forced towards 1. Formally, if a high order sliding mode is established, one gets $\bar{\alpha} = 1$: a linear controller versus S_ρ is obtained

  $$\upsilon = -k_\rho S_\rho \tag{2.45}$$

  that reduces the energy consumption;

- on the contrary, if a sliding mode is not established, $\bar{\alpha}$ reaches 0 and increases the control accuracy given that the control law appears as a sliding mode one versus S_ρ

$$\upsilon = -k_\rho \text{sign}(S_\rho) \tag{2.46}$$

- ϵ_{S_i} and $\bar{\beta}$ are the $\rho + 1$ parameters acting on the accuracy of the controller.

In conclusion, this approach allows to get a trade-off between accuracy and energy consumption.

2.5 Application to floating wind turbine

As described in Section 2.2, the control input u and the output y can be defined as (β_{col} being the collective blade pitch angle, and Ω_r (resp. Ω_r^*) being the rotor (resp. reference) velocity)

$$\begin{aligned} u &= \beta_{col} \\ y &= \Omega_r - \Omega_r^* \end{aligned} \tag{2.47}$$

with Ω_r^* defined by (2.1). The control objective is to ensure y converging to 0. System (1.10)-(1.11) with the output y has a relative degree with respect to the CBP angle β_{col} equal to 1. Consequently, the sliding variable vector S is defined as

$$S = \Omega_r - \Omega_{r0} + k\dot{\varphi} \tag{2.48}$$

Then, the time derivative of S reads as

$$\dot{S} = a(\cdot) + b(\cdot)u \tag{2.49}$$

with $a(\cdot)$ and $b(\cdot)$ unknown but bounded functions, derived from uncertain functions $f_{wt}(x,t)$ and $-g_{wt}(x,t)$ [4] (see system (1.13) detailed in Chapter 1).

2.5.1 Adaptive STW controllers

Given that the control strategies applied in the sequel are based on STW algorithm, system on which they are applied must have a relative degree equals to 1. With S defined as (2.48), that is in the case.

4. Notice that the term $b(\cdot)$ must be positive according to Assumption 2, but the term $g_{wt}(x,t)$ is negative according to the linearized model. Thus, define that $b(\cdot) = -g_{wt}(x,t)$.

ASTW based control law

Recall that the ASWT algorithm can be applied without the knowledge of $a(\cdot)$ and $b(\cdot)$. Therefore, the control input reads as

$$\begin{aligned} u &= -k_1|S|^{\frac{1}{2}}\text{sign}(S) - \int_0^t k_2\text{sign}(S)d\tau \\ \dot{k}_1 &= \begin{cases} \omega\sqrt{\frac{\chi}{2}}\text{sign}(|S|-\mu) & \text{if } k_1 > k_m \\ m & \text{if } k_1 < k_m \end{cases} \\ k_2 &= \epsilon k_1 \end{aligned} \tag{2.50}$$

SAST based control law

As mentioned in Subsection 2.4.2, the formal proof of SAST algorithm has been made based on the Assumption 3, with $a_0(\cdot)$ and $b_0(\cdot)$ supposed to be well-know terms. can be derived from system model. Recalling that, for a given wind speed V and a given rotor speed Ω_r, the wind turbine model can be written as a linear one, it is possible to numerically evaluate the terms $a(x,t)$ and $b(t)$ from FAST software. Indeed, for each couple wind speed-rotor speed, from the linearized model (1.9) around this operating point, $a(x,t)$ and $b(t)$ are derived from system metrics $A_{Avg}(x,t)$, $B_{Avg}(x,t)$ and the state vector x. Figure 2.4 displays the evolution of $b(t)$ with respect to the rotor speed Ω and the wind speed V. Consider that $b(t)$ can be written as

$$b(t) = b_0 + b_u(t)$$

with b_0 being the nominal term and $b_u(t)$ describing the uncertainties on $b(t)$. From Figure 2.4, $b(t)$ is bounded between 0.2282 and 1.2603 on the operating domain. Furthermore, one can arbitrarily state $b_0 = 0.7403$ that gives $-0.5121 \leq b_u(t) \leq 0.5200$. Thus, $|b_u(t)| < b_0$.

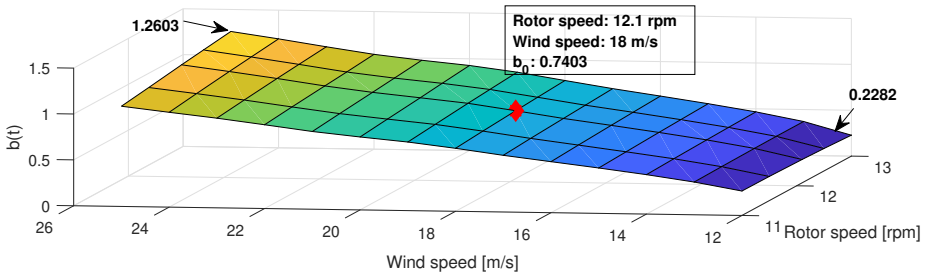

Figure 2.4 – Function $b(t)$ versus rotor speed Ω (rpm) and wind speed $V(m/s)$.

Consider now that $a(x,t)$ can be written as

$$a(x,t) \quad = \quad \underbrace{(a_0 + a_u(t))}_{h(t)} \cdot x \tag{2.51}$$

with a_0 1×3-vector the nominal term and $a_u(t)$ 1×3-vector containing the uncertainties on $a(x,t)$ that is varying with the considered operating points. Denote $h(t) = [h_1 \ h_2 \ h_3] = a_0 + a_u(t) = [a_{10} \ a_{20} \ a_{30}] + [a_{1u}(t) \ a_{2u}(t) \ a_{3u}(t)]$. By a similar way than previously, Figure 2.5 displays the evolution of each component of $h(t)$ with respect to the rotor speed Ω_r and the wind speed V. Form this figure, one can find that $h(t)$ is bounded in the operating domain, and thereby, $a(x,t)$ is bounded as well. Furthermore, considering $h(t)$ at the rated rotor speed and the rated wind speed, one can arbitrarily state $a_0 = [a_{10} \ a_{20} \ a_{30}] = [-0.1753 \ -1.7760 \ -0.1487]$.

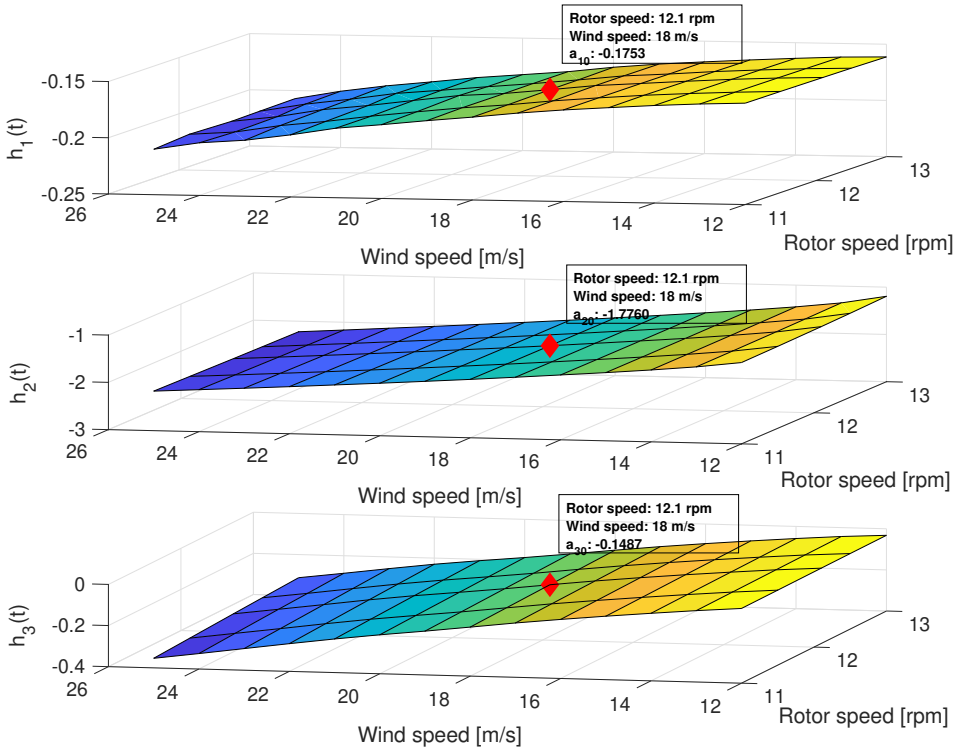

Figure 2.5 – Vector $h(t)$ versus rotor speed Ω (rpm) and wind speed V (m/s).

Then, from (2.49), one gets

$$\dot{S} \quad = \quad [a_0 + a_u(t)] \cdot x + [b_0 + b_u(t)]u \tag{2.52}$$

Considering the control law as (2.23)

$$u = \frac{v - a_0 \cdot x}{b_0}, \tag{2.53}$$

one gets

$$\dot{S} = v + \underbrace{(a_u - \frac{b_u}{b_0}a_0) \cdot x + \frac{b_u}{b_0} \cdot v}_{\varrho} \tag{2.54}$$

Recalling that $|b_u(t)| < |b_0|$, it is trivial to show that the control v as defined as (2.24)

$$\begin{aligned} v &= -2L|S|^{\frac{1}{2}}\text{sign}(S) - \int_0^t \frac{L^2}{2}\text{sign}(S)d\tau \\ \dot{L} &= \begin{cases} L\left(|S| - \mu\right), & \text{if } L > L_m \\ L_m & \text{if } L \leq L_m \end{cases} \end{aligned} \tag{2.55}$$

allows the establishment of a second order sliding mode. However, given that all the other controllers are designed without prefeedback (2.23) [5], SAST will be used in the similar way, *i.e.*

$$u = -2L|S|^{\frac{1}{2}}\text{sign}(S) - \int_0^t \frac{L^2}{2}\text{sign}(S)d\tau \tag{2.56}$$

Indeed, considering S-dynamics

$$\dot{S} = [a_0 + a_u(t)] \cdot x + [b_0 + b_u(t)]u \tag{2.57}$$

one gets

$$\dot{S} = \{[a_0 + a_u(t)] \cdot x + b_u(t) \cdot u\} + b_0 \cdot u \tag{2.58}$$

then,

$$\dot{S} = \underbrace{[a_0 + a_u(t)] \cdot x + [b_u(t) - 1 + b_0] \cdot u}_{\varrho} + u \tag{2.59}$$

Recalling that $b_0 = 0.7403$ and $-0.5121 \leq b_u(t) \leq 0.5200$, one gets

$$-0.7718 \leq b_u(t) - 1 + b_0 \leq 0.2603$$

it means that the control input u can always act on S-dynamics, in spite of the fact that ϱ depends on u. Then, the system (2.59) is under the form of (2.22). SAST algorithm can be directly applied.

5. Indeed, the objective is to have the most simple control structure.

2.5.2 Homogeneity based controller

As detailed in Subsection 2.3.1, the homogeneity based controller can be applied only if the relative degree ρ is larger or equal to 2. However, as shown in (2.49), the relative degree is equal to 1. A solution consists in acting through the time derivative of u. Denoting $\bar{u} = \dot{u}$, one has

$$\ddot{S} = \bar{a}(\cdot) + \bar{b}(\cdot)\bar{u} \tag{2.60}$$

with $\bar{a}(\cdot)$ and $\bar{b}(\cdot)$ respectively derived from $a(\cdot)$ and $b(\cdot)$. Then, considering (2.60), the relative degree ρ equals to 2 with respect to the *new* input $\bar{u}$. In this case, the HCVP control algorithm can be applied and reads as

$$\begin{aligned} \bar{u} &= -k_2 \lceil S_2 \rfloor^{\bar{\alpha}} \\ \bar{\alpha} &= max(-\bar{\beta} \sum_{i=1}^{2} \frac{|S^{(i-1)}|}{|S^{(i-1)}| + \epsilon_{S_i}} + 1, 0) \end{aligned} \tag{2.61}$$

with $S_2 = \lceil \dot{S} \rfloor^2 + k_1^2 S$ and $S_1 = S$.

2.5.3 Baseline gain scheduled PI control

The gain-scheduled proportional integral (GSPI) controller based on the CBP control developed by (J. Jonkman, Butterfield, et al. 2009) is a well-known controller for the FWT in Region III. It is widely used as the baseline controller by the community of researchers to compare the performances of the proposed controllers. The GSPI control is given by

$$\beta_{col} = K_p e(t) + K_i \int_0^t e(\tau) \mathrm{d}\tau \tag{2.62}$$

with

- $e(t)$ the error between the actual generator speed Ω_g and the rated generator speed Ω_{g0}

$$e(t) = \Omega_g - \Omega_{g0} = n_g(\Omega_r - \Omega_{r0}) \tag{2.63}$$

- K_p and K_i the proportional and integral gain respectively, which are given by

$$K_p = \frac{2 I_D \Omega_{r0} \xi \omega_n}{n_g(-\frac{\delta P}{\delta \beta_{col}})} \tag{2.64}$$

and

$$K_i = \frac{I_D \Omega_{r0} \omega_n^2}{n_g(-\frac{\delta P}{\delta \beta_{col}})} \tag{2.65}$$

with I_D the drive train inertia of the low-speed shaft, ξ and ω_n the closed-loop natural frequency and damping ratio respectively. The term $\delta P/\delta\beta_{col}$ is the sensitivity of the rotor aerodynamic power to collective blade pitch angle that depends on the wind speed, rotor speed and blade pitch angle; its value can be calculated by FAST linearization program and varies for different operating points, as shown in Table 2.2. Therefore, the controllers gains K_p and K_i are viewed as functions of the collective blade pitch angle. Detailed information of the power sensitivity and controller gains can be found in (J. Jonkman, Butterfield, et al. 2009).

Table 2.2 – Sensitivity $\delta P/\delta\beta_{col}$ versus wind speed, rotor speed and blade pitch angle (J. Jonkman, Butterfield, et al. 2009).

Wind speed (m/s)	Rotor speed (rpm)	Blade pitch angle (°)	$\delta P/\delta\beta_{col}$ (watt/rad)
11.4 (Rated)	12.1	0.00	-28.24E+6
12	12.1	3.83	-43.73E+6
13	12.1	6.60	-51.66E+6
14	12.1	8.70	-58.44E+6
15	12.1	10.45	-64.44E+6
16	12.1	12.06	-70.46E+6
17	12.1	13.54	-76.53E+6
18	12.1	14.92	-83.94E+6
19	12.1	16.23	-90.67E+6
20	12.1	17.47	-94.71E+6
21	12.1	18.70	-99.04E+6
22	12.1	19.94	-105.90E+6
23	12.1	21.18	-114.30E+6
24	12.1	22.35	-120.20E+6
25	12.1	23.47	-125.30E+6

Equation (2.62) shows that the GSPI control regulates only the rotor speed to its rated value by actuating the collective blade pitch angle. Considering the negative damping problem introduced by the floating structure, a solution is to ensure the smallest closed-loop natural frequency lower than the smallest system natural frequency (*i.e.* the natural frequency of floating structure) (J. Jonkman

2008a; Larsen and Hanson 2007).

As conclusion, the gains K_p and K_i are reevaluated at each operating point depending on wind speed, rotor speed and blade pitch angle. From (J. Jonkman, Butterfield, et al. 2009), by applying such approach, the controller can achieve the control objectives in Region III.

2.6 Simulations and analysis

In this section, simulations are made by co-simulation between FAST and Matlab/Simulink. As detailed in Section 1.4, the model used is the NREL 5MW OC3-Hywind FWT one. All simulations have been made over 600 seconds. The integration algorithm is ODE1 (Euler) with a fixed step equal to 0.0125 *sec.* Considering the real applications, blade pitch angles are saturated as $[0°, 90°]$ whereas the blade pitch rates limit is $8°/s$ (J. Jonkman, Butterfield, et al. 2009). Three scenarios of simulations are made in the sequel in order to evaluate the performances of the proposed adaptive controllers.

- **Scenario 1** is considered to evaluate the efficiency of the proposed SAST controller. Being a new adaptive control algorithm, SAST controller is firstly evaluated on a reduced FAST nonlinear model with only wind disturbance, without wave. Moreover, the performances of SAST are compared with the ASTW control;

- **Scenario 2** is made in order to check that the proposed control algorithms are working well on the full DOFs FAST nonlinear model. Namely, with a single set of parameters, the controller gains are adapted in different ranges of wind speed. For sake of simplicity, only ASTW controller is checked, and the performances are compared to GSPI control;

- **Scenario 3** evaluates all the three controllers (ASTW, SAST and HCVP) in more or less realistic conditions. The full DOFs FAST nonlinear model is used whereas wind speed varies in Region III with irregular waves. The performances are compared to GSPI control.

The parameter k of sliding variable (2.48) is equal to 16.7 in all the three scenarios.

2.6.1 Scenario 1

This scenario focuses on the evaluation of SAST controller in a "simple case" described as follows: only 2DOFs are enabled (rotor speed and platform pitch) in the FAST code, $18m/s$ stochastic wind with 15% turbulence intensity (see Figure 2.6); still water.

The ASTW and SAST controllers have been tuned as depicted in Table 2.3. Notice the difference

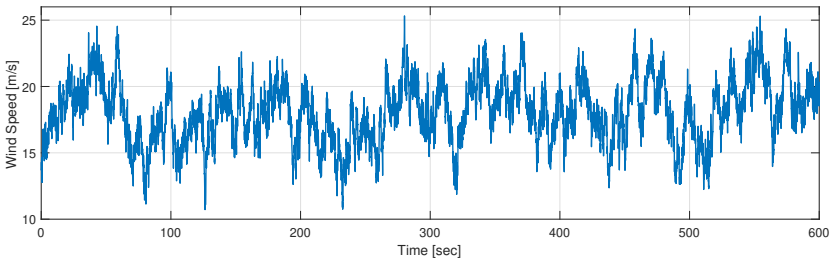

Figure 2.6 – **Scenario 1.** Wind speed (m/s) versus time (sec).

of parameters number. The parameters have been tuned in order to get the best results for each controller.

Table 2.3 – **Scenario 1.** Controller parameters.

ASTW	$\omega = 0.001$, $\chi = 2$, $\epsilon = 0.05$, $k_m = 0.0001$, $\mu = 0.01$, $\eta = k_m$
SAST	$L_m = 0.0001$, $\mu = 0.02$

The simulation results are displayed in Figure 2.7 and show comparison with GSPI. Obviously, the SAST control successfully achieves both the control objectives, *i.e.* regulation of the rotor speed around its rated value, and reduction of the platform pitch rate. Table 2.4 shows that the SAST algorithm allows better performances than GSPI controller; comparing with ASTW, SAST has similar performances but the advantage is its reduced number of parameters (see Table 2.3). Since only 2 DOFs are enabled, the rest of DOFs are considered rigid; therefore, the platform roll, yaw and fatigue life of the wind turbine components are not evaluated in this scenario. All of those performance indicators will be evaluated and compared in a more realistic condition in Scenario 3.

Table 2.4 – **Scenario 1.** RMS values of rotor speed error and platform pitch rate with SAST, ASTW and GSPI controllers

RMS	Rotor speed error (rpm)	Platform pitch rate (deg/s)
SAST	0.4954	0.0685
ASTW	0.4943	0.0603
GSPI	1.2540	0.0730

2.6.2 Scenario 2

For this scenario, only the ASTW and GSPI controllers are applied on the full-DOFs enabled FAST nonlinear model. The controllers performances are compared under irregular wave with significant height of 3.25 m and peak spectral period of 9.7 s, with 3 cases of wind conditions (see Figure 2.8)

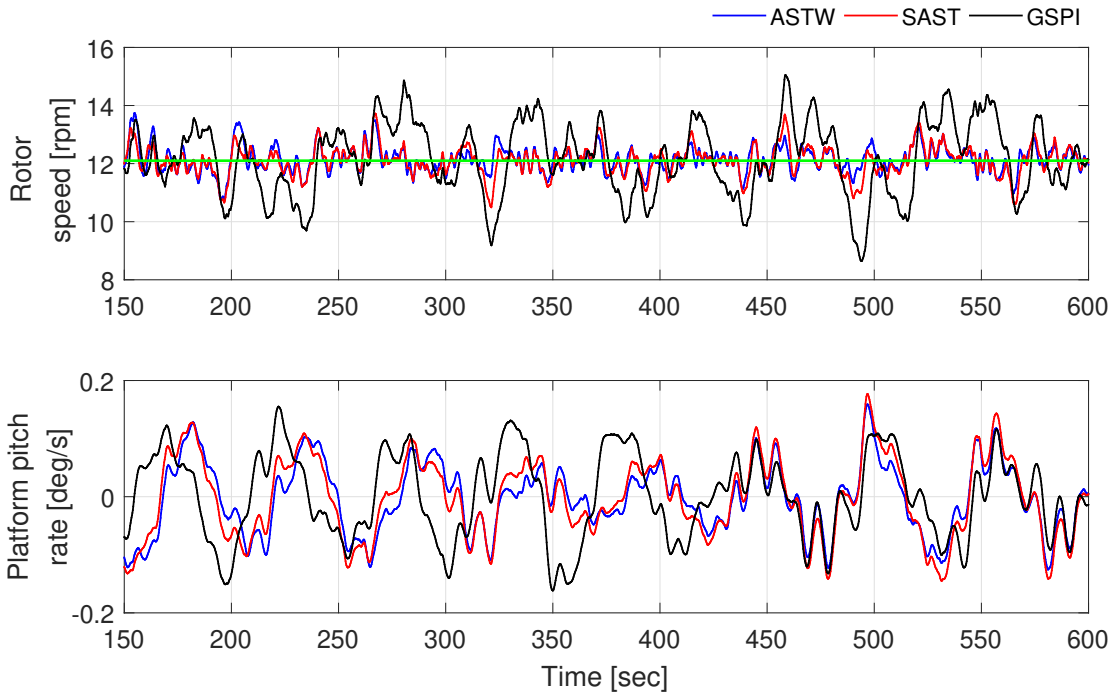

Figure 2.7 – **Scenario 1. Top.** Rotor speed Ω_r (rpm) versus time (sec). The green line is the rated value of rotor speed that is the control objective. **Bottom.** Platform pitch rate $\dot{\varphi}$ (deg/s) versus time (sec).

- Case 1: 16 m/s stochastic wind, 5% turbulence intensity;
- Case 2: 18 m/s stochastic wind, 5% turbulence intensity;
- Case 3: 20 m/s stochastic wind, 5% turbulence intensity.

A single set of parameters is used for ASTW controller in the 3 cases ($\omega = 0.001$, $\chi = 2$, $\epsilon = 0.05$, $k_m = 0.12$, $\mu = 0.01$ and $\eta = k_m$). The purpose of this scenario is to illustrate the efficiency of adaptive law on the full DOFs FAST nonlinear model, even if only a single set of parameter is used.

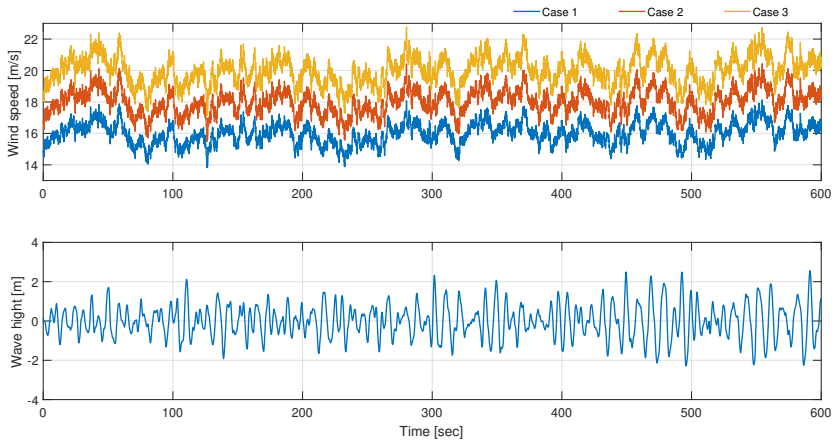

Figure 2.8 – **Scenario 2. Top.** Wind speed (m/s) versus time (sec). **Bottom.** Wave height (m) versus time (sec).

Figure 2.9 shows the main normalized performance indicators: root mean square (RMS) of rotor speed error, RMS of power error, RMS of platform pitch rated and variation (VAR) of blade pitch angle. ASTW and GSPI allow to obtain very similar performances (through RMS) concerning the rotor speed/power error in the 3 cases. Concerning the platform pitch rate, the ASTW gives smaller RMS values than GSPI; namely, the platform pitch motion is reduced with respect to GSPI. Recall that such performances are carried out with only one set of parameters while the GSPI needs more parameters (see Table 2.2). A drawback of ASTW controller is that it stimulates more the blade pitch angle actuator (see VAR of blade pitch angle in Figure 2.9). Finally, recall that Scenario 2 considers only 5% wind turbulence; Scenario 3 will propose more realistic and different conditions.

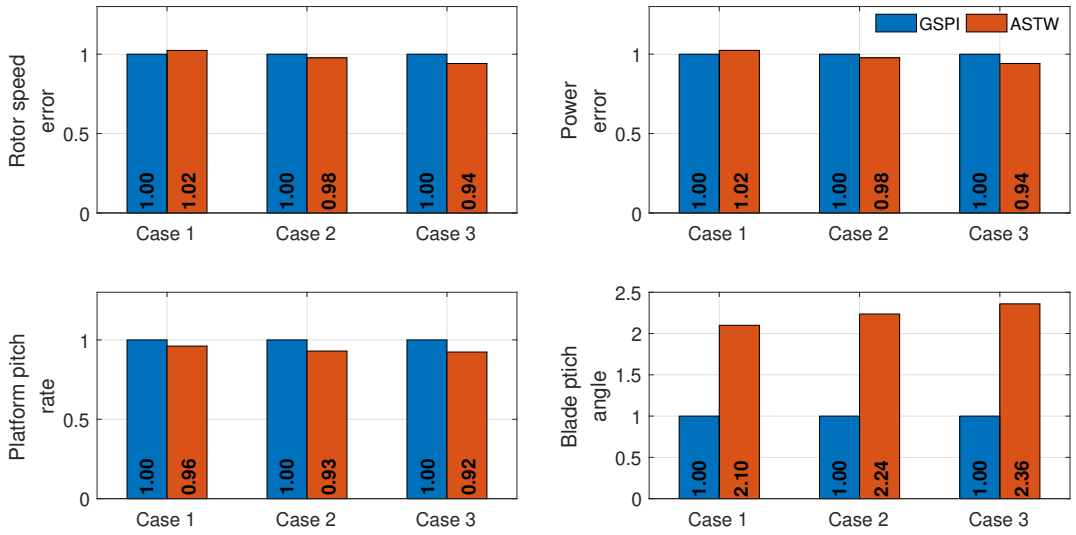

Figure 2.9 – **Scenario 2.** Normalized performance indicators for the 3 cases. **Top-left.** RMS of rotor speed error. **Top-right.** RMS of power error. **Bottom-left.** RMS of platform pitch rate. **Bottom-right.** VAR of blade pitch angle.

2.6.3 Scenario 3

It has been shown in the previous scenarios that

- the proposed SAST control is efficient for the FWT control application on the reduced FAST nonlinear model and has good performances with respect to perturbations and uncertainties of the system.
- the ASTW controller is working well considering the full DOFs FAST nonlinear model, in different wind conditions with reduced turbulence with only a single phase of tuning;

In the Scenario 3, conditions are more close from real ones and are described as

- all-DOFs enabled FAST nonlinear model;
- 18 m/s stochastic wind with 15% turbulence intensity (Figure 2.6);
- irregular wave with significant height of 3.25m and peak spectral period of 9.7s (Figure 2.8-bottom).

The three adaptive controllers (ASTW, SAST and HCVP) are now applied and compared with GSPI. The controller parameters are given in Table. 2.5.

Table 2.5 – **Scenario 3**: controller parameters.

ASTW	$\omega = 0.001$, $\chi = 2$, $\epsilon = 0.03$, $\mu = 0.05$, $\eta = k_m$
SAST	$L_m = 0.0001$, $\mu = 0.06$
HCVP	$\epsilon_{S_1} = 0.05$, $\epsilon_{S_2} = 0.02$, $k_1 = 0.11$, $k_2 = 0.015$, $\bar{\beta} = 1.2$

Figure 2.10 shows the main variables of the FWT obtained by the four controllers: the power, the rotor speed, the platform pitch rate and the blade pitch angle. Clearly, all the controllers allow to achieve the control objectives recalling that the controllers are designed on a 2 DOFs system, and applied to the full DOFs nonlinear model. The generator power and the rotor speed are varying around their rated values, *i.e.* 5 MW and 12.1 rpm respectively. The platform pitch rate is varying around 0 meaning that the platform pitch motion is limited and the system is stabilized.

For a sake of clearly, the performance indicators are normalized with respect to GSPI (see Figures 2.11, 2.12 and 2.13). As a consequence, a value smaller/larger than 1 means that the performance of the control is better/worse than GSPI. All the performance indices are computed between 150 sec and 600 sec in order to reduce the influence of the initial condition.

From Figure 2.11-top. the adaptive controllers (ASTW, SAST and HCVP) have smaller RMS for rotor speed/power error and platform pitch rate than GSPI; it means that both the two control objectives are achieved with better performances than GSPI. Of course, such improvements have a cost and lead to a larger value of the VAR of blade pitch angle: the adaptive controllers are using by a more intensive way, the blade pitch actuator. However, since the blade pitch angle saturation ([0°, 90°]) and rate limiter (8°/s maximum) are taken into consideration in the simulations, the controllers can be applied in practice. Furthermore, Figure 2.11-bottom displays the RMS of the platform rotations (yaw, pitch and roll angle) and their rates. Although those indicators are not so important than the previous ones, they should be kept as low as possible in order to get a lower tower base bending load. All these indicators are smaller with adaptive controllers than with GSPI. These controllers improve the associated performances. Furthermore, notice that the three adaptive controllers greatly reduce the roll and the roll rate comparing with GSPI.

Fatigue damage equivalent load (DEL) is used to measure the fatigue load of structure (as detailed in Section 1.4.3) is evaluated for the tower base (TB), the blade root (BR) (see Figure 2.12) and the mooring lines (see Figure 2.13). Figure 2.12 shows DEL performances of the proposed controllers

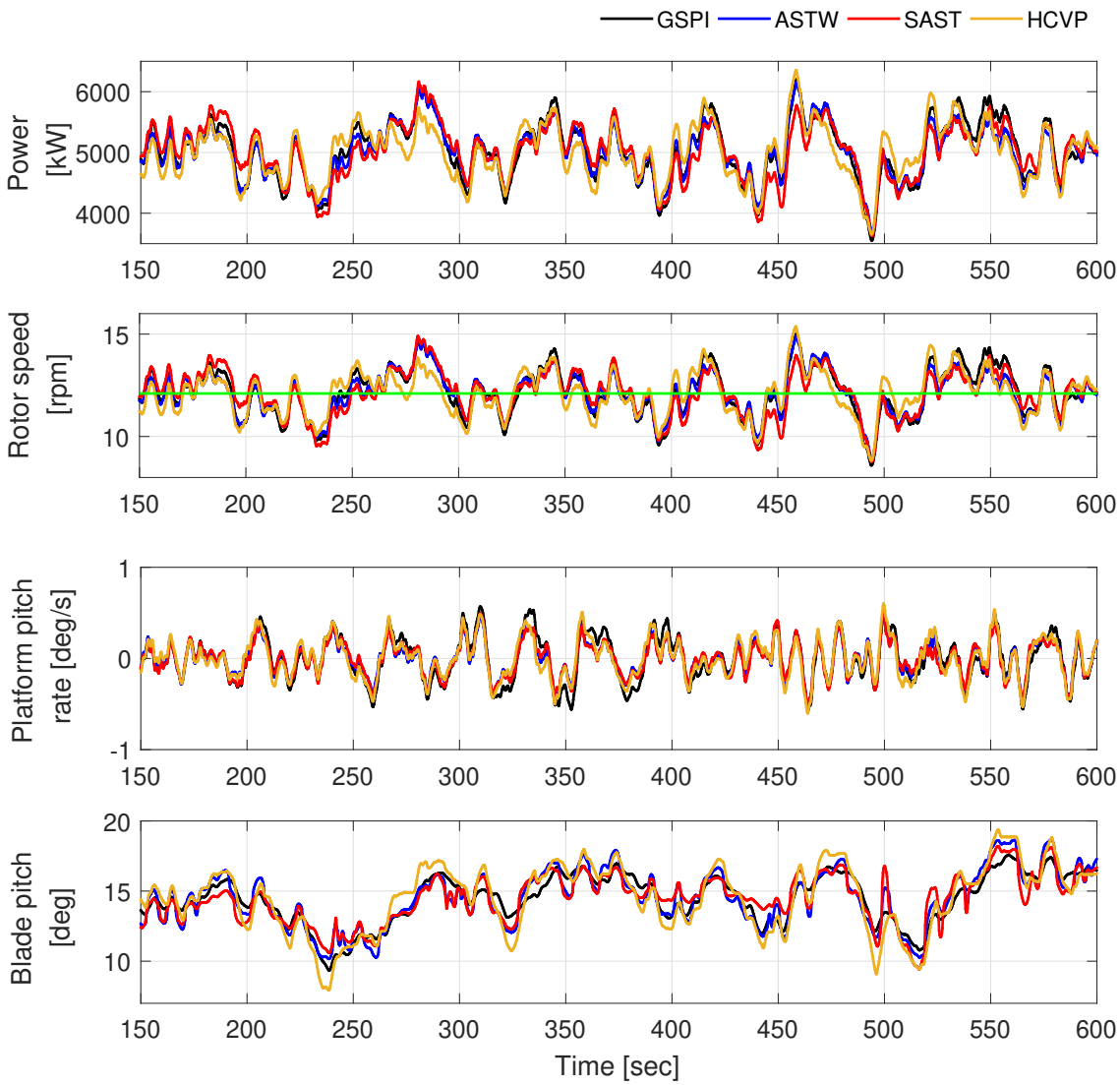

Figure 2.10 – **Scenario 3.** Main variables of the FWT versus time (*sec*) respectively, obtained by GSPI (black), ASTW (blue), SAST (red) and HCVP (yellow). The green line in the second sub-figure indicates the rated rotor speed Ω_{r0} (12.1 *rpm*).

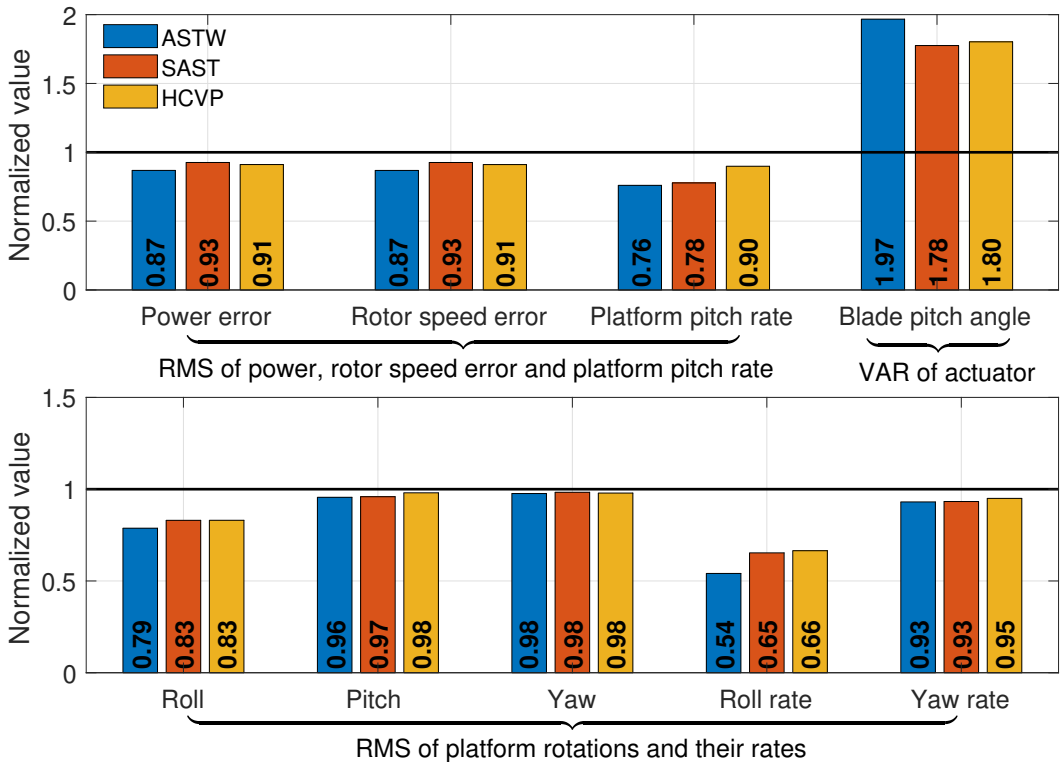

Figure 2.11 – **Scenario 3.** Normalized RMS/VAR values of performances indicators obtained by ASTW (blue), SAST (red) and HCVP (yellow) controllers.

comparing with GSPI: ASTW slightly reduces the tower base load and slightly increases the blade root flap-wise moment by +5%. SAST has almost no influence on the tower base and blade root load whereas HCVP allows a reduction of the tower base side-to-side load by −8% but induces an increase of the blade root flap-wise moment by +12%. Figure 2.13 shows the normalized DEL of the fair-lead force (FF) and anchor force (AF) of the 3 mooring lines. SAST and HCVP controllers decrease FF and AF loads of the mooring lines about 10%. However, ASTW increases these loads about 10%.

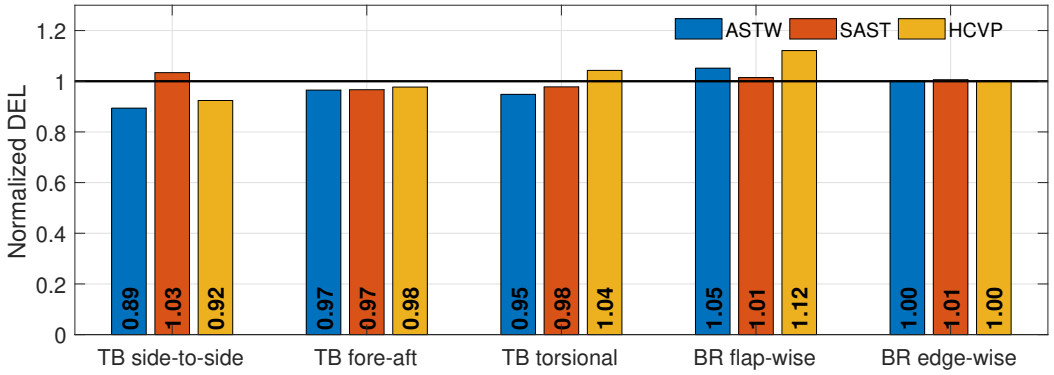

Figure 2.12 – **Scenario 3.** Normalized DEL values of TB and BR loads obtained by ASTW (blue), SAST (red) and HCVP (yellow) controllers.

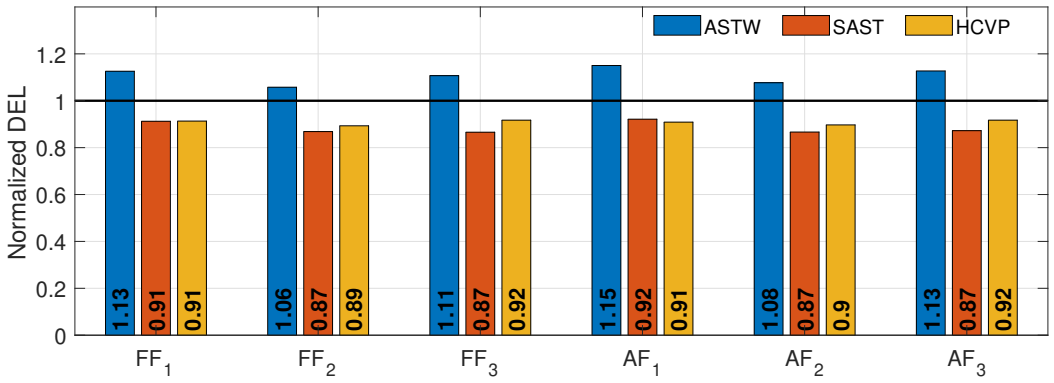

Figure 2.13 – **Scenario 3.** Normalized DEL values of mooring line loads obtained by ASTW (blue), SAST (red) and HCVP (yellow) controllers.

Recall that the ASTW, SAST and HCVP controllers are based on gain/parameter adaptation algorithms. Figure 2.14 shows ASTW gain k_1 (top), SAST gain L (middle) and adaptive exponent $\bar{\alpha}$ (bottom) for HCVP. The variation of the gains/parameter illustrate their dynamical adaptation versus the wind and wave perturbations; it clearly shows that

- for ASTW and SAST control, a time-varying gain offers a good opportunity to limit the gain versus the operating conditions;

- for HCVP control, the parameter $\bar{\alpha}$ that varies from $[0, 1]$ allows to reduce the chattering of the controller. Notice that the average value of $\bar{\alpha}$ for $t \in [100,\ 600]$ is 0.07.

Notice from Figure 2.15 that, after a transient time and for the three controllers, the sliding variables are converging towards a vicinity of 0.

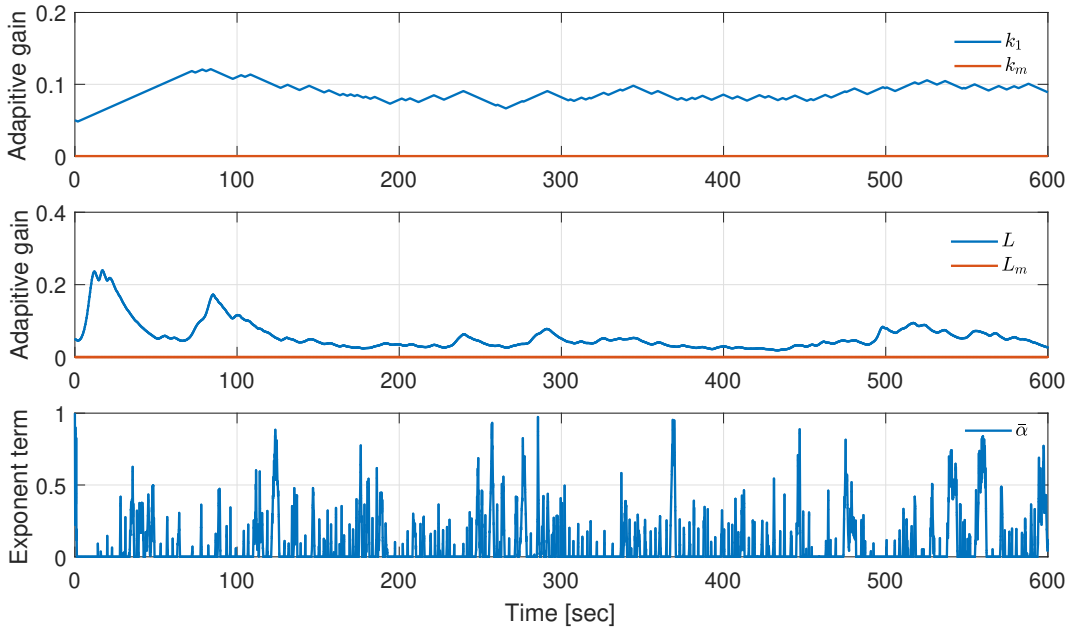

Figure 2.14 – **Scenario 3. Top.** ASTW controller gain k_1 (blue) and minimum value k_m (red) versus time (*sec*). **Middle.** SAST controller gain L (blue) and constant value L_m (red) versus time (*sec*). **Bottom.** HCVP exponent term $\bar{\alpha}$ versus time (*sec*).

Table 2.6 summarizes the performances information of the 4 controllers. It appears that SAST, with a very reduced number of parameters, allows to get among the best accuracy and the most reduced fatigue loads, with reasonable oscillations of blade pitch angle.

2.7 Conclusions

In this chapter, adaptive high order sliding mode control is applied to the FWT based on the collective blade pitch control. First, the formalization of the problem and the control objectives of the FWT are discussed: regulation of the rotor speed at its rated value (assuming that the generator

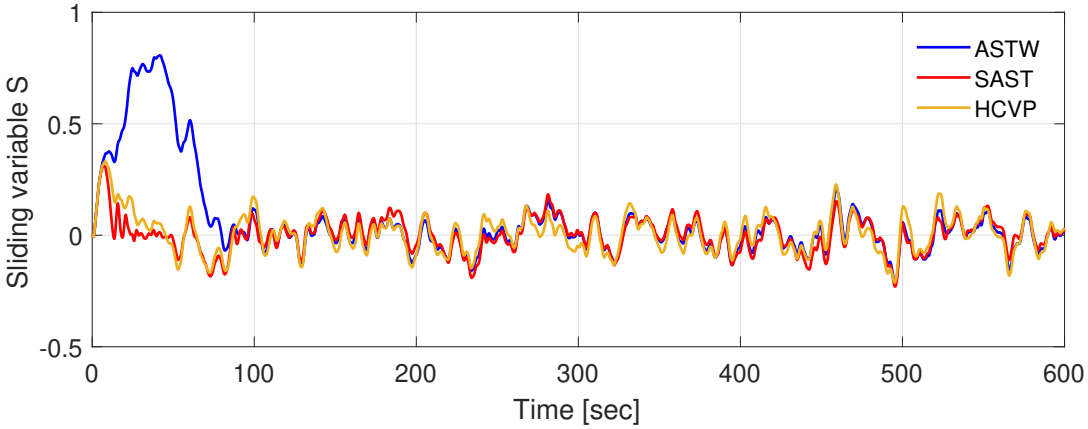

Figure 2.15 – **Scenario 3.** Sliding variable S versus time (sec) of ASTW (blue), SAST (red) and HCVP (yellow) controllers.

Table 2.6 – Performances information of the 4 controllers.

Control algorithm	Number of parameters	Accuracy of objectives	Actuator oscillation	Fatigue loads
GSPI	- - -	-	+ +	-
ASTW	+ +	+ +	- -	-
SAST	+ + +	+ +	- -	+
HCVP	+	+	- -	+

torque is fixed) and reduction of the platform pitch motion by using CBP control. Then, high order sliding mode control laws with different adaptation algorithms are recalled, including the adaptive super-twisting (ASTW) (Yuri Shtessel, Taleb, and Plestan 2012) and a recent developed homogeneity based controller with varying exponent parameter (HCVP) (Tahoumi, Plestan, et al. 2019). Meanwhile, a simplified adaptive super-twisting (SAST) algorithm with very few tuning parameters (only 2 parameters are must be tuned) is proposed. All of those algorithms are implemented to FWT in the FAST/SIMULINK environment and the performances are compared with the GSPI (J. Jonkman 2008a) control in different scenarios. Finally, the simulation results show that the adaptive control algorithms allow to successfully control the floating wind turbines in Region III with very reduced parameter tuning and knowledge of system modeling and have globally better performances than standard GSPI. Moreover, it appears that the proposed SAST control, with much less tuning parameters than ASTW and SAST, gives globally the best performances.

Chapter 3

Control of FWT equipped by a permanent magnet synchronous generator

Contents

3.1 Introduction

In Chapter 2, several adaptive high order sliding mode control algorithms have been applied on the FWT in Region III. Thanks to these novel approaches, both the power variation and the platform pitch motion are compared with the GSPI controller (J. Jonkman 2008b). These results have been obtained based on the fact that the generator torque is supposed to be fixed at its rated value, the power regulation being achieved by the rotor speed regulation. In fact, no model and control of electrical generator is considered.

In the current chapter, a permanent magnet synchronous generator (PMSG) is taken into consideration, and two adaptive versions of super-twisting controllers are applied to the FWT equipped

by a PMSG. The control is not only acting on the aero/hydrodynamic part, but also considers the electrical part that has not been made in previous chapter. Hence, both the collective blade pitch control and the generator torque control are now considered. In the sequel, the reference generator torque is no longer constant at the rated value, but is now varying with the rotor speed in order to guarantee a better regulation of power. The reference rotor speed is varying with platform pitch velocity as perennially to ensure attenuation of the platform pitch motion. Moreover, since a generator is considered, the limitation of oscillations of the electromagnetic torque is also taken in to consideration. In summary, the main contributions of this chapter are:

- modeling of the PMSG and interaction it with the FWT model;
- description of the control of the floating wind turbine equipped by a PMSG;
- application of the proposed adaptive HOSM controllers to the FAST software including PMSG model in SIMULINK, and performance analysis.

3.2 Model of FWT with the electric machine

3.2.1 Model of the permanent magnet synchronous generator

The PMSG is used by an industrial way, since it has features of high efficiency, high reliability, and low maintenance level (Haque, Negnevitsky, and Muttaqi 2010; Benelghali, Benbouzid, and Charpentier 2012; Keysan, McDonald, and Mueller 2011). Those features appear to be especially suitable for the wind turbines power generation systems, and the synchronous generator plays a crucial role in transforming mechanical energy into electrical energy. The mathematical model of the synchronous generator is a prerequisite in order to design the control algorithms. In this section, models of the PMSG in both the three-phase plane and the rotary $d-q$ reference frame, are recalled.

Three-phase model of PMSG (Guenoune 2018; Glumineau and De León-Morales 2015)

In order to establish a simplified model of the PMSG, consider the following assumptions

- the stator windings are balanced with a sinusoidal distribution of the magneto-motive force;
- the saturation of the magnetic circuit is neglected;
- Eddy currents, hysteresis phenomena and rotor salience are neglected.

The machine voltages in the three-phase frame of reference (a, b, c) of the stator are given by

$$\begin{bmatrix} V_a \\ V_b \\ V_c \end{bmatrix} = R_s \begin{bmatrix} i_a \\ i_b \\ i_c \end{bmatrix} + \frac{d}{dt} \begin{bmatrix} \phi_a \\ \phi_b \\ \phi_c \end{bmatrix} \tag{3.1}$$

with

$$\begin{bmatrix} \phi_a \\ \phi_b \\ \phi_c \end{bmatrix} = L_s \begin{bmatrix} i_a \\ i_b \\ i_c \end{bmatrix} + \phi_f \begin{bmatrix} cos(\theta) \\ cos(\theta - \frac{2\pi}{3}) \\ cos(\theta + \frac{2\pi}{3}) \end{bmatrix} \tag{3.2}$$

where

- $[V_a,\ V_b,\ V_c]^T$ the stator phase voltages;
- $[i_a,\ i_b,\ i_c]^T$ the stator phase currents;
- $[\phi_a,\ \phi_b,\ \phi_c]^T$ the stator fluxes;
- R_s the stator resistance. The resistances on the three-phase are assumed to be identical;
- ϕ_f the magnetic fluxes of the magnets;
- θ the angular position of the generator rotor;
- L_s the inductance matrix (3×3) composed by constant term and variable term such that

$$L_s = L_{s0} + L_{sv} \tag{3.3}$$

with

$$L_{s0} = \begin{bmatrix} L_{s0} & M_0 & M_0 \\ M_0 & L_{s0} & M_0 \\ M_0 & M_0 & L_{s0} \end{bmatrix} \tag{3.4}$$

and

$$L_{sv} = \begin{bmatrix} cos(2\theta_e) & cos(2\theta_e - \frac{2\pi}{3}) & cos(2\theta_e + \frac{2\pi}{3}) \\ cos(2\theta_e - \frac{2\pi}{3}) & cos(2\theta_e + \frac{2\pi}{3}) & cos(2\theta_e) \\ cos(2\theta_e + \frac{2\pi}{3}) & cos(2\theta_e) & cos(2\theta_e - \frac{2\pi}{3}) \end{bmatrix} \tag{3.5}$$

where L_{s0}, L_{sv} and M_0 are the proper and mutual inductances respectively. These terms are constant. Finally, $\theta_e = p\theta$ with p the number of poles of the generator.

Two-phase ($d-q$ frame) model of PMSG (Glumineau and De León-Morales 2015; Soliman et al. 2018)

The expressions of PMSG model in the three-phase reference frame are not easy to manipulate and for the control design. The three-phase-two-phase transformation makes it possible to obtain a simplified representation of the PMSG in a plane equivalent to two axes. By using the so-called Park's transformations (Park 1929; Vas 1998), the a, b, c three-phase currents of the stator are transferred to the direct axis (d-axis), quadrature axis (q-axis) and the zero axis (0-axis) perpendicular to the $d-q$ plane along with the rotor rotation, thus simplifying the analysis of synchronous machine. The standard model of PMSG in the $d-q$ frame reads as

$$\begin{aligned} V_d &= R_s i_d L_d \frac{di_d}{dt} - p\Omega_g L_q i_q \\ V_q &= R_s i_q L_q \frac{di_q}{dt} + p\Omega_g L_d i_d + p\phi_f \Omega_g \end{aligned} \tag{3.6}$$

with

- i_d and i_q the currents along the $d-q$ axes respectively;
- V_d and V_q the voltages along the $d-q$ axes respectively;
- L_d and L_q the inductances along the $d-q$ axes respectively; in this work, one assumes $L_d = L_q$;
- ϕ_f the permanent-magnet flux linkage;
- Ω_g the generator speed.

The circuit of PMSG on $d-q$ frame can be shown schematically in Figure 3.1, with E_d and E_q the counter electric potentials of d and q axes respectively, and reading as

$$\begin{aligned} E_d &= 0 \\ E_q &= p\Omega_g \phi_f \end{aligned} \tag{3.7}$$

The generator electromagnetic torque is given by (Soliman et al. 2018)

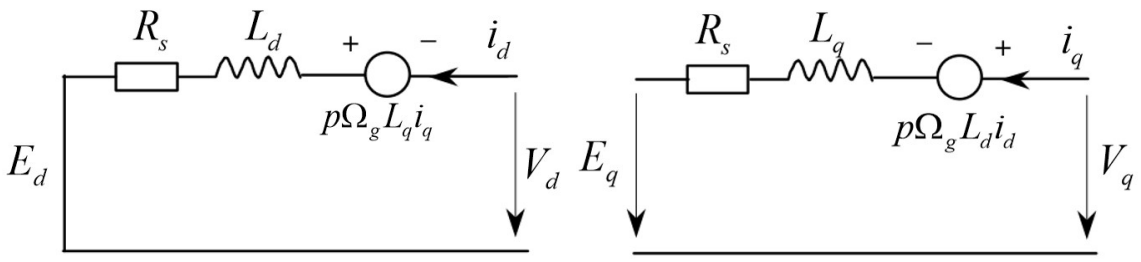

Figure 3.1 – Equivalent circuit of PMSG in the $d-q$ frame (Yin et al. 2007). **Left.** d-axis equivalent circuit. **Right.** q-axis equivalent circuit.

$$\Gamma_g = \frac{3}{2}p(\phi_f i_q + (L_q - L_d) i_d i_q) \tag{3.8}$$

Since the inductances along the $d-q$ axes are equal, the generator torque reads as

$$\Gamma_g = \frac{3}{2}p\phi_f i_q \tag{3.9}$$

Notice that Γ_g directly depends on q-axis current i_q and so could be controlled by i_q. This feature will be used in the sequel by a control point-of-view.

3.2.2 Model of the whole system

From (3.6), one gets the dynamics of $d-q$ currents

$$\begin{aligned} \frac{di_d}{dt} &= -\frac{R_s}{L_d} i_d + \frac{pL_q}{L_d}\Omega_g i_q + \frac{1}{L_d} V_d \\ \frac{di_q}{dt} &= -\frac{R_s}{L_q} i_q - \frac{pL_d}{L_q}\Omega_g i_d - \frac{p\phi_f}{L_q}\Omega_g + \frac{1}{L_q} V_q \end{aligned} \tag{3.10}$$

Then, the PMSG system can be written as

$$\dot{x}_{em} = f_{em}(x_{em}, \Omega_g) + g_{em} u_{em} \tag{3.11}$$

with $x_{em} = [i_d \; i_q]^T$ the state vector and $u_{em} = [V_d \; V_q]^T$ the input vector. The functions $f_{em}(x_{em}, \Omega_g)$ and g_{em} are defined respectively by

$$f_{em}(x_{em}, \Omega_g) = \begin{bmatrix} -\frac{R_s}{L_d} i_d + \frac{pL_q}{L_d}\Omega_g i_q \\ -\frac{R_s}{L_q} i_q - \frac{pL_d}{L_q}\Omega_g i_d - \frac{p\phi_f}{L_q}\Omega_g \end{bmatrix} \tag{3.12}$$

$$g_{em} = \begin{bmatrix} \frac{1}{L_d} & 0 \\ 0 & \frac{1}{L_q} \end{bmatrix} \tag{3.13}$$

Recalling the reduced FWT model (1.13) detailed in Section 1.3.1, as previously explained, in a large operating domain, the model of FWT can be defined as [1]

$$\dot{x}_{wt} = f_{wt}(x_{wt}, t) + g_{wt}(t)u_{wt} \tag{3.14}$$

with $x_{wt} = [\varphi\ \dot{\varphi}\ \Omega_r]^T$, φ being the platform pitch angle and Ω_r the rotor speed. u_{wt} is the collective blade pitch angle β_{col}. $f_{wt}(x_{wt}, t)$ is unknown but bounded function: it contains the properties of wind turbine in different operating point (the term $A_{Avg}(x, t)$ in (1.12)), the uncertainties of the system, the perturbations introduced by wind (the term $B_{d_{Avg}}(x, t)) \cdot \delta$ in (1.12)), waves and other external environments; $g_{wt}(t)$ is supposed to be unknown but bounded input function.

Notice that system (3.11) and (3.14) are linked by the the rotation speeds of generator/rotor with $\Omega_g = n_g\Omega_r$. Thus, combining the reduced model of FWT (3.14) and the model of PMSG (3.11), the whole system model can be viewed as the following nonlinear multiple-input multiple-output (MIMO) system

$$\dot{x} = \underbrace{\begin{bmatrix} f_{wt}(x_{wt}, t) \\ f_{em}(x_{em}) \end{bmatrix}}_{f(x,t)} + \underbrace{\begin{bmatrix} g_{wt}(t) & \mathbf{0}_{1\times 2} \\ \mathbf{0}_{2\times 1} & g_{em}(x_{em}) \end{bmatrix}}_{g(x,t)} \cdot \underbrace{\begin{bmatrix} \beta_{col} \\ V_d \\ V_q \end{bmatrix}}_{u} \tag{3.15}$$

with the state vector x and the input vector u of the whole system defined as

$$x = \begin{bmatrix} \varphi \\ \dot{\varphi} \\ \Omega_r \\ i_d \\ i_q \end{bmatrix},\ u = \begin{bmatrix} \beta_{col} \\ V_d \\ V_q \end{bmatrix} \tag{3.16}$$

Notice that $f(x, t)$ and $g(t)$ can be viewed as uncertain functions given that

- $f(x, t)$ depends on the perturbation term $B_{d_{Avg}}(x, t)) \cdot \delta$ and electrical parameters (resistances, inductance, ...) that can strongly vary especially versus temperature;

1. For a sake of clarity, notice the state vector and the input of the reduced FWT model as x_{wt} and u_{wt} respectively.

- $g(t)$ depends on inductance.

3.3 Control problem statement

In the considered operating region (Region III), the control objectives of floating wind turbine are the regulation of the power at its rated value P_0 to avoid overload operation and protect the electric machine; the second objective consists in attenuating the platform pitch motion so as to protect mechanical structure. In Chapter 2, the power regulation is achieved by regulating the rotor speed Ω_r with generator torque supposed at its rated value. The generator torque control was not taken into consideration, namely, the generator torque was supposed to be perfectly maintained at Γ_{g0}. In this chapter, given that the PMSG is now combined, the power control is completed by torque control and rotor speed control. Two kinds of strategies are possible

- **constant torque:** as detailed in Chapter 2, the generator torque Γ_g is fixed at its rated value Γ_{g0}, the power regulation being then turned into rotor speed regulation according to the relation between the power, the torque and the rotor speed

$$P = n_g \Gamma_{g0} \Omega_r. \tag{3.17}$$

- **constant power:** the control is directly acting on the power. In this case, the generator torque is no longer fixed at its rated value, but is changing with respect to the rotor speed, in order to maintain the constant power output, *i.e.*

$$P_0 = n_g \Gamma_g \Omega_r. \tag{3.18}$$

These two approaches will be used in the sequel. It has been demonstrated that, for the baseline GSPI control, the constant power strategy results in a smaller power variation (obvious given that the power is directly controlled) but induces additional platform pitch motion and structure loads whereas the constant torque strategy increases power variation but gives better performances on platform pitch motion and structure loads (Larsen and Hanson 2007; J. Jonkman 2008a; H. Namik and K. Stol 2014).

In this chapter, the adaptive high order sliding mode controllers are based on the constant power

approach, whereas two baseline GSPI controllers are applied both the constant torque and constant power approach, and are used as comparison objects.

3.3.1 Rotor speed reference

As explained in Chapter 2, in order to both regulate the rotor speed and reduce the platform pitch motion by CBP approach, a solution is to define the desired rotor speed Ω_r^* as a function of platform pitch velocity $\dot{\varphi}$

$$\Omega_r^* = \Omega_{r0} - k\dot{\varphi} \tag{3.19}$$

with $k > 0$.

3.3.2 Quadratic current reference

As mentioned previously, generator torque control is applied in this chapter. From (3.9), one finds that the generator torque can be modified by the quadratic current i_q, and then acting on the power output. Hence, according to the two control approaches (constant torque (3.17) and constant power (3.18)), the desired quadratic current i_q^* for the two strategies is designed as follows.

- **constant torque:** suppose that the generator torque is fixed at its rated value Γ_{g0}. According to (3.9), one has

$$\Gamma_{g0} = \frac{3}{2} p\phi_f i_q \tag{3.20}$$

  Then, the reference quadratic current i_q^* is defined as

$$i_q^* = \frac{2\Gamma_{g0}}{3p\phi_f} \tag{3.21}$$

  in order to keep a constant generator torque [2];

- **constant power:** in order to maintain a constant (rated) power output, the following equation based on (3.9) and (3.18) is established

$$\frac{P_0}{n_g\Omega_r} = \frac{3}{2} p\phi_f i_q \tag{3.22}$$

  Therefore, if the current i_q tracks the following reference

$$i_q^* = \frac{2P_0}{3n_g\Omega_r p\phi_f}, \tag{3.23}$$

2. In this case, if Ω_r is forced to Ω_r^* with reduced platform pitch motion, $\Omega_r = \Omega_{r0}$. Then, the power equals to its rated value $P_0 = n_g\Gamma_{g0}\Omega_{r0}$.

the power output is limited to its rated value.

3.3.3 Direct current reference

The oscillations of the electromagnetic torque can amplify the fatigue loads on the mechanical shaft, thus affecting the quality of the energy produced. In order to limit this drawback, a solution consists in forcing the direct current i_d to zero (Glumineau and De León-Morales 2015; Z. Chen 2013). The reference of this current is given by

$$i_d^* = 0. \tag{3.24}$$

3.4 Control algorithms application

From the control objectives detailed in the previous section, the control input vector u and the output vector y of the whole system read as (i_q^* used here being defined by (3.23))

$$u = \begin{bmatrix} \beta_{col} \\ V_d \\ V_q \end{bmatrix}, \quad y = \begin{bmatrix} y_1 \\ y_2 \\ y_3 \end{bmatrix} = \begin{bmatrix} \Omega_r - \Omega_r^* \\ i_d - i_d^* \\ i_q - i_q^* \end{bmatrix} \tag{3.25}$$

Recall that the control objective of is to force y to 0 (in practice, this objective is to force y to a vicinity of 0). From (3.15), the relative degree vector of the three outputs y_1, y_2 and y_3 with respect respectively to β_{col}, V_d and V_q is equal to $[1,\ 1,\ 1]$. As a consequence, the sliding vector S is defined as

$$S = \begin{bmatrix} S_1 \\ S_2 \\ S_3 \end{bmatrix} = \begin{bmatrix} y_1 \\ y_2 \\ y_3 \end{bmatrix} = \begin{bmatrix} \Omega_r - \Omega_{r0} + k\dot{\varphi} \\ i_d \\ i_q - \dfrac{2P_0}{3n_g\Omega_r p\phi_f} \end{bmatrix} \tag{3.26}$$

Dynamics of S_1. According to (3.19), (3.25) and (3.26), S_1-dynamics reads as

$$\dot{S}_1 = \dot{\Omega}_r + k\ddot{\varphi} \tag{3.27}$$

Recalling (1.4), (1.6) and (3.9), one gets

$$\dot{S}_1 = \underbrace{\frac{1}{2J}\left(\frac{C_p(\lambda,\beta_{col})}{\lambda}\rho\pi R^2 V^3 - 3n_g p\phi_f i_q\right)}_{\dot{\Omega}_r} + k\ddot{\varphi} \tag{3.28}$$

Notice that $\dot{\Omega}_r$ depends on the power coefficient C_p that is not well-known [3]. However, according to (1.3), it can be numerically shown that the power coefficient C_p can be approximated as

$$C_p = C_{p1}(\cdot) + C_{p2}(\cdot)\beta_{col} \tag{3.29}$$

Then, the dynamic of Ω_r can be rewritten as

$$\dot{\Omega}_r = a_{\Omega_r}(\cdot) + b_{\Omega_r}(\cdot)\beta_{col} \tag{3.30}$$

with a_{Ω_r} and b_{Ω_r} unknown but bounded functions. On the other hand, recalling the reduced linear model detailed in Subsection 1.3.1, $\ddot{\varphi}$ is a not well-known dynamics. For a large operating domain, one has [4]

$$\ddot{\varphi} = a_{\varphi}(\cdot) + b_{\varphi}(\cdot)\beta_{col} \tag{3.31}$$

with a_{φ} and b_{φ} unknown but bounded functions. As a consequence, the dynamic of S_1 can be rewritten as

$$\dot{S}_1 = a_1(\cdot) + b_1(\cdot)\beta_{col} \tag{3.32}$$

with $a_1 = a_{\Omega_r} + a_{\varphi}$, $b_1 = b_{\Omega_r} + b_{\varphi}$ unknown but bounded functions.

Dynamics of S_2. According to (3.10), (3.24), (3.25) and (3.26), S_2-dynamics reads as

$$\dot{S}_2 = -\frac{R_s}{L_d} i_d + \frac{pL_q}{L_d}\Omega_g i_q + \frac{1}{L_d} V_d \tag{3.33}$$

It can be rewritten as

$$\dot{S}_2 = a_2(\cdot) + b_2(\cdot)V_d \tag{3.34}$$

Notice that, in (3.10), one supposes that each parameter is composed by a known nominal part and unknown uncertainty one (for example, the resistance R_s can be written as $R_s = R_{sn} + \Delta R_s$, R_{sn} being the nominal value and ΔR_s the associated uncertainty). Then, one gets $a_2 = a_{2n} + \Delta a_2$ and $b_2 = b_{2n} + \Delta b_2$ with a_{2n} and b_{2n} the nominal part reading as

$$\begin{aligned} a_{2n} &= -\frac{R_s}{L_d} i_d + \frac{pL_q}{L_d}\Omega_g i_q \\ b_{2n} &= \frac{1}{L_d} \end{aligned} \tag{3.35}$$

3. C_p depends on the fitting coefficients c_1 - c_5. These coefficients are not well-known and introduce uncertainties (see Subsection 1.2.2).

4. Indeed, it is clear that $\dot{\Omega}_r$ can be obtained by this way. However, in this work, $\dot{\Omega}_r$ is obtained based on the physical model in order to claim that the physical model and the linearized model could get the same result.

Dynamics of S_3. According to (3.10), (3.23), (3.25) and (3.26), S_3-dynamics reads as

$$\dot{S}_3 = -\frac{R_s}{L_q} i_q - \frac{pL_d}{L_q}\Omega_g i_d - \frac{p\phi_f}{L_q}\Omega_g - \frac{2P_0\dot{\Omega}_r}{3n_g p\phi_f \Omega_r^2} + \frac{1}{L_q} V_q \tag{3.36}$$

It depends on the dynamics of Ω_r that is not well-known and coupled with the blade pitch angle β_{col}. However, numerical analysis in the operating domain shows that the influence of β_{col} is very limited on S_3-dynamics. Therefore, considering the term in $\dot{S}_3$ that contains $\dot{\Omega}_r$, as a bounded perturbation, it gives

$$\dot{S}_3 = a_3(\cdot) + b_3(\cdot) V_q \tag{3.37}$$

with $a_3 = a_{3n} + \Delta a_3$ and $b_3 = b_{3n} + \Delta b_3$. The terms a_{3n} and b_{3n} read as

$$\begin{aligned} a_3 &= -\frac{R_s}{L_q} i_q - \frac{pL_d}{L_q} n_g \Omega_g i_d - \frac{p\Phi_f}{L_q} n_g \Omega_g \\ b_{3n} &= \frac{1}{L_q} \end{aligned} \tag{3.38}$$

Therefore, the control input reads as

$$u = \begin{bmatrix} \beta_{col} \\ V_d \\ V_q \end{bmatrix} = \begin{bmatrix} \upsilon_1 \\ \dfrac{1}{b_{2n}}\left(-a_{2n} + \upsilon_2\right) \\ \dfrac{1}{b_{3n}}\left(-a_{3n} + \upsilon_3\right) \end{bmatrix} \tag{3.39}$$

with υ_1, υ_2 and υ_3 defined as adaptive super-twisting algorithms (2.11)

$$\begin{bmatrix} \upsilon_1 \\ \upsilon_2 \\ \upsilon_3 \end{bmatrix} = \begin{bmatrix} -k_{11}|S_1|^{\frac{1}{2}}\text{sign}(S_1) - \displaystyle\int_0^t k_{12}\text{sign}(S_1)d\tau \\ -k_{21}|S_2|^{\frac{1}{2}}\text{sign}(S_2) - \displaystyle\int_0^t k_{22}\text{sign}(S_2)d\tau \\ -k_{31}|S_3|^{\frac{1}{2}}\text{sign}(S_3) - \displaystyle\int_0^t k_{32}\text{sign}(S_3)d\tau \end{bmatrix} \tag{3.40}$$

with the gains k_{11}, k_{21}, k_{31} and k_{12}, k_{22}, k_{32} defined from (2.21) for ASTW, and from (2.27) for SAST [5].

5. For the controller gains of SAST in this chapter, $k_{i1} = 2L$, $k_{i2} = L^2/2$, $i \in \{1,\ 2\ ,\ 3\}$.

3.4.1 Baseline gain-scheduling PI controller

The baseline controller used in this paper for the rotor speed control loop is the famous GSPI controller (J. Jonkman 2008b; J. Jonkman, Butterfield, et al. 2009). Then, the control input

$$\upsilon_1 = n_g K_p(\Omega_r - \Omega_{r0}) + n_g K_i \int_0^t (\Omega_r - \Omega_{r0})\mathrm{d}\tau \tag{3.41}$$

with K_p and K_i obtained for different operating points and scheduled as functions of blade pitch angle (see Subsection 2.5.3). Furthermore, the gains are detuned in order to avoid platform pitch negative damping; details can be found in (J. Jonkman 2008b). Recall that the tuning of such controller is a huge and fastidious task given the large operating domain. For the generator torque/power control loop, two kinds of strategies (H. Namik and K. Stol 2014) are used in the sequel

- **Constant power control.** The control V_d and V_q are defined by (3.39) with

$$\begin{aligned} \upsilon_2 &= K_{p2} S_2 + K_{i2} \int_0^t S_2(\tau) d\tau \\ \upsilon_3 &= K_{p3} S_3 + K_{i3} \int_0^t S_3(\tau) d\tau \end{aligned} \tag{3.42}$$

  with S_2 and S_3 defined by (3.26).
- **Constant torque control.** As detailed previously, the generator torque is forced to its rated Γ_{g0}, *i.e.* $\Gamma_g^* = \Gamma_{g0}$. One gets

$$i_q^* = \frac{2\Gamma_{g0}}{3p\phi_f}$$

  Hence, similar PI controllers as (3.42) are used with S_2 defined as (3.26) and S_3 as

$$S_3 = i_q - \frac{2\Gamma_{g0}}{3p\phi_f} \tag{3.43}$$

3.5 Simulations and analysis

The simulations have been carried out assuming that the FAST 5MW OC3-Hywind floating wind turbine model is equipped with a permanent magnet synchronous generator. The parameters of the PMSG are displayed in Table 3.1 and the characteristics of the FWT have been detailed in Chapter 1. All simulations are made by co-simulation between all DOFs enabled FAST model and SIMULINK, the simulation time being 600 seconds. Euler integration algorithm is used with a fixed step of 0.0125 second. Four control strategies based on the control input defined by (3.39) are presented and compared in the sequel

- **GSPI1+PI:** rotor speed control GSPI (3.41) with *constant torque* strategy power/direct current PI control (3.42), S_2 and S_3 being defined by (3.26);

- **GSPI2+PI:** rotor speed control GSPI (3.41) with *constant power* strategy power/direct current control (3.42), S_2 being defined by (3.26) and S_3 by (3.43);

- **ASTW:** super-twisting algorithm (3.40) with gain adaptation law defined by (2.21);

- **SAST:** super-twisting algorithm (3.40) with gain adaptation law defined by (2.27).

Table 3.1 – PMSG parameters

Parameters	Value
Rated power P_0	5 MW
Rated generator speed	1173.7 rpm
Stator resistance R_s	1.06 Ω
Stator inductance L_d, L_q	14.29 mH
Flux linkage ϕ_f	8.6 Wb
No. of pole pairs p	5
Maximum generator torque	47,402.91 N·m
Maximum generator torque rate	15000 N·m/s

All the simulations are made under the same conditions (see Figure 3.2)

- $18m/s$ stochastic wind with 15% turbulence intensity;

- irregular wave with significant height of $3.25m$, peak spectral period of $9.7s$.

Recall that, a saturation on blade pitch angle and an associated rate limiter are introduced in order to ensure more accurate simulations versus real system. Furthermore, perturbations were added on i_d and i_q by a band-limited white noise block of SIMULINK with noise power equal to 20 and 30 respectively, both of them having a sampling time equal to 5 ms. Finally, as explained just after (3.34), parametric uncertainties are considered (Table 3.2) which introduce bias in the control law through the functions a_{2n}, b_{2n}, a_{3n} and b_{3n} (see (3.35)-(3.38)), so as to check the robustness of the closed-loop system. The controller gains of the two GSPI controllers are the same and composed

Table 3.2 – Parametric uncertainties of PMSG

Uncertain parameters	Uncertainty amplitudes (%)
Stator resistance R_s	-25
Stator inductance L_d	20
Flux linkage ϕ_f	-20

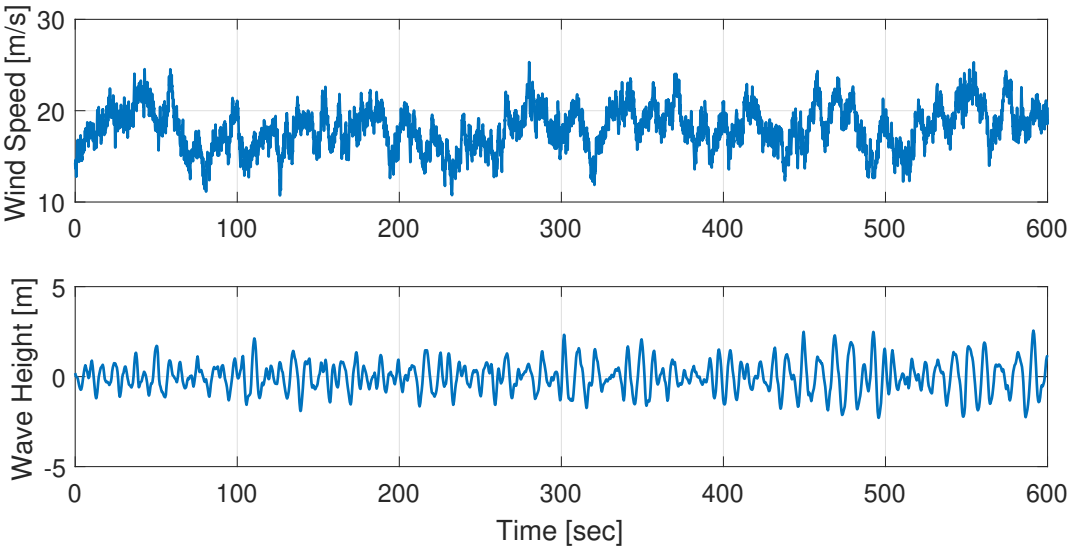

Figure 3.2 – Wind speed (**top**) and wave height (**bottom**) versus time (*sec.*).

by two parts: the controller gains for the rotor speed control loop K_p and K_i are the same as in (J. Jonkman 2008b). The gains for the electrical part are displayed in Table 3.3 whereas the controller gains of ASTW and SAST are shown in Table 3.4 and the parameter k of sliding variable S_1 in (3.26) is equal to 16.7. All these gains have been tuned in order to get the best performances.

Table 3.3 – Controller gains of PI

Controlled variables	Proportional gain	Integral gain
Direct current i_d	500	10^4
Quadratic currents i_q	200	10^4

Table 3.4 – Controller gains of ASTW and SAST

Gains	Parameters of ASTW	Parameters of SAST
k_{11}, k_{12}	$\alpha_m = 10^{-5}$, $\omega = 0.001$, $\chi = 2$, $\epsilon = 0.03$, $\mu = 0.05$, $\eta = 10^{-5}$	$l_m = 10^{-5}$, $\mu = 0.06$
k_{21}, k_{22}	$\alpha_m = 1$, $\omega = 200$, $\chi = 2$, $\epsilon = 200$, $\mu = 0.05$, $\eta = 10$	$l_m = 0.01$, $\mu = 0.05$
k_{31}, k_{32}	$\alpha_m = 100$, $\omega = 40$, $\chi = 2$, $\epsilon = 300$, $\mu = 0.1$, $\eta = 10$	$l_m = 0.01$, $\mu = 0.1$

Figure 3.3 shows the evolution of the main variables of the system; it gives a general view of the different controllers performances. These plots show that the four controllers are more or less efficient. In order to accurately analyzing the closed-loop system performances, recall the following performance indicators detailed in Chapter 1.

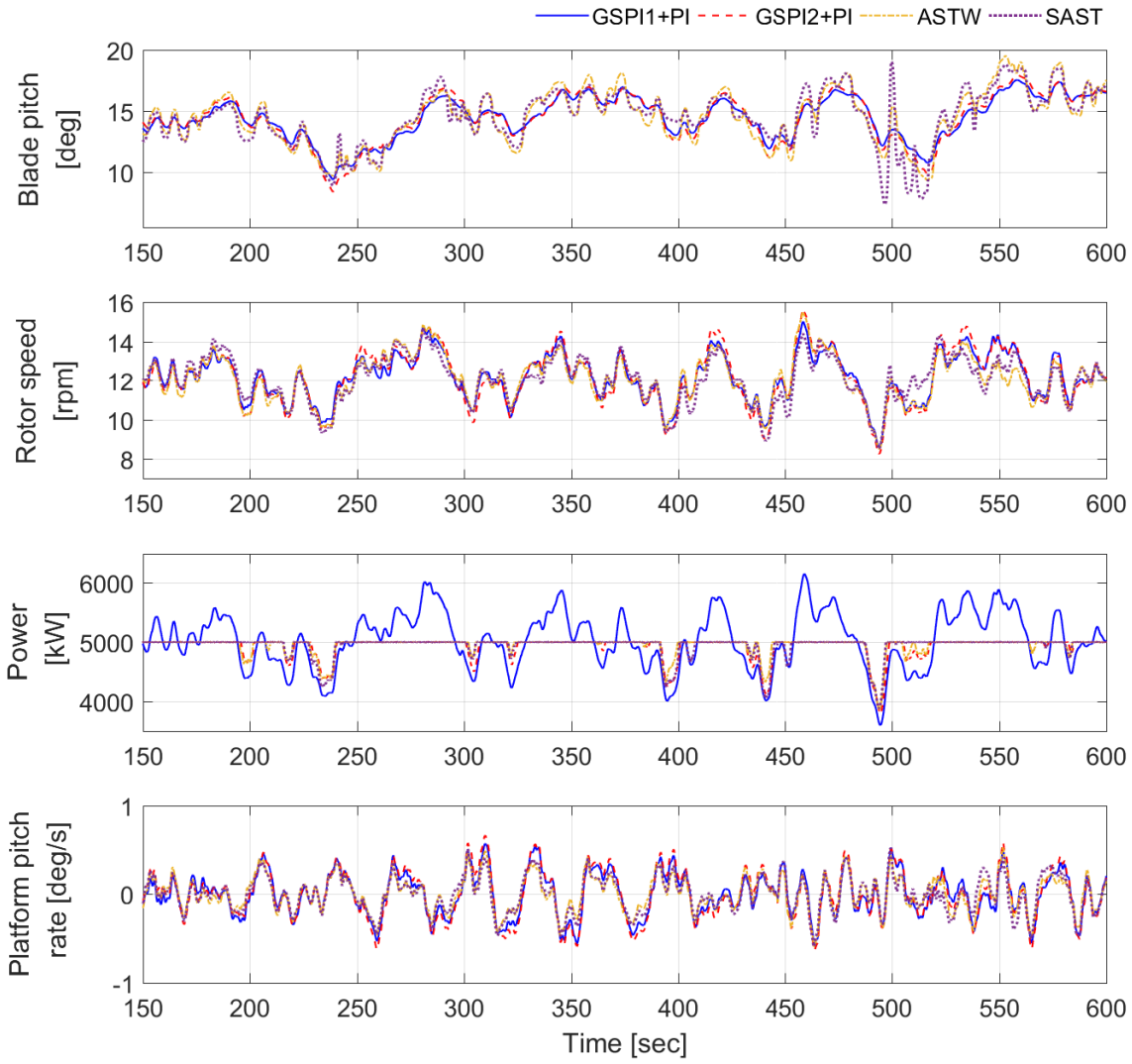

Figure 3.3 – Main variables of the FWT versus time (sec), obtained by GSPI1+PI (blue), GSPI2+PI (red), ASTW (yellow) and SAST (purple) controllers.

- root mean square (RMS) of the error between the actual and rated power, the RMS of platform roll, pitch, yaw and the RMS of platform pitch rate. For all these RMS values, the objective is to obtain the smallest values;

- variation (VAR) of the blade pitch angle; it indicates the level of blade pitch actuation: a high value implies its frequent use and is a key-indicator in order to detect chattering;

- damage equivalent load (DEL) of tower base (TB) moments in fore-aft, side-to-side and torsional directions, the DEL of blade root (BR) edge-wise and flap-wise moments, the DEL of fair-lead force (FF) and anchor force (AF) of 3 mooring lines. Such indicators evaluate the fatigue load of the structure, the objective being to obtain the smallest values.

All of these performance indicators are normalized with respect to GSPI1+PI controller such that, the normalized values for GSPI1+PI controller are equal to 1 as shown in Figures 3.4 and 3.5.

First-of-all, Figures 3.4 and 3.5 display that GSPI1+PI control (constant torque) reduces, versus GSPI2+PI solution, the platform pitch motion and turbine loads (such as tower base and blade flap-wise loads) but increases the power regulation error versus GSPI2+PI control (constant power). Notice that this latter point could damage the generator because the power can be over the rated one (see Figure 3.3). Such conclusions are in accordance with (H. Namik and K. Stol 2014). Furthermore, it is natural that the power tracking is better with constant power based control, than with constant torque based control. Concerning DEL of the three mooring lines, the results obtained by both the GSPI controllers are similar.

Concerning the nonlinear controllers, both of them reduce the power error (see Figure 3.4; -64% for ASTW, -60% for SAST) versus GSPI1+PI, without increasing platform pitch motion (see Figure 3.4: lower pitch rate, lower roll). Versus GSPI2+PI, ASTW and SAST allow getting a reduction of roll and pitch rate that is a key-point. From these two first remarks, one can conclude that both nonlinear controllers have the advantages of both GSPI controllers without their lacks.

Concerning DEL, the ASTW and SAST do not improve the tower base moments DEL (Figure 3.5-top) versus GSPI controllers, but they clearly improve the mooring lines DEL (Figure 3.5-bottom). That is also a key-point for the stability and the viability of the system.

To summarize, the ASTW and SAST are more efficient versus GSPI1+PI and GSPI2+PI, on the basis of power regulation and platform pitch motion reduction; improvement is also obtained for the mooring lines. However, the cost of such improvements is a more important use of the blade

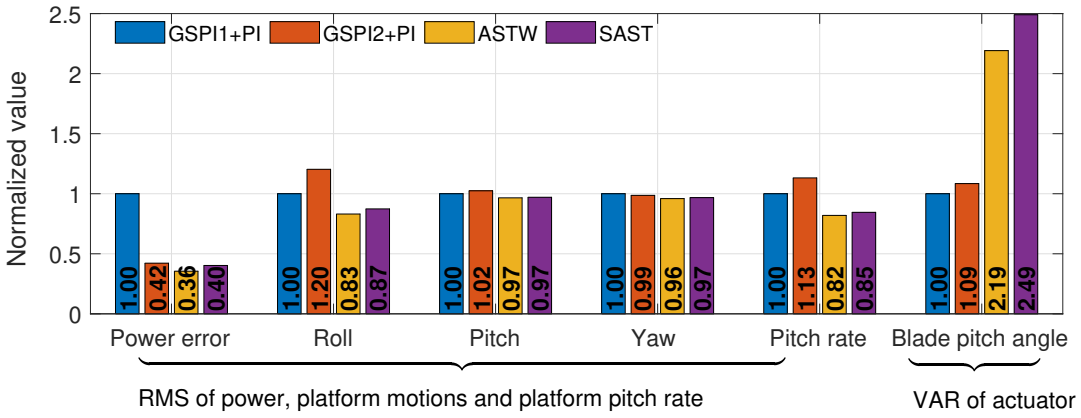

Figure 3.4 – Normalized RMS/VAR values of several performances indicators with GSPI1+PI (blue), GSPI2+PI (red), ASTW (yellow) and SAST (purple) controllers.

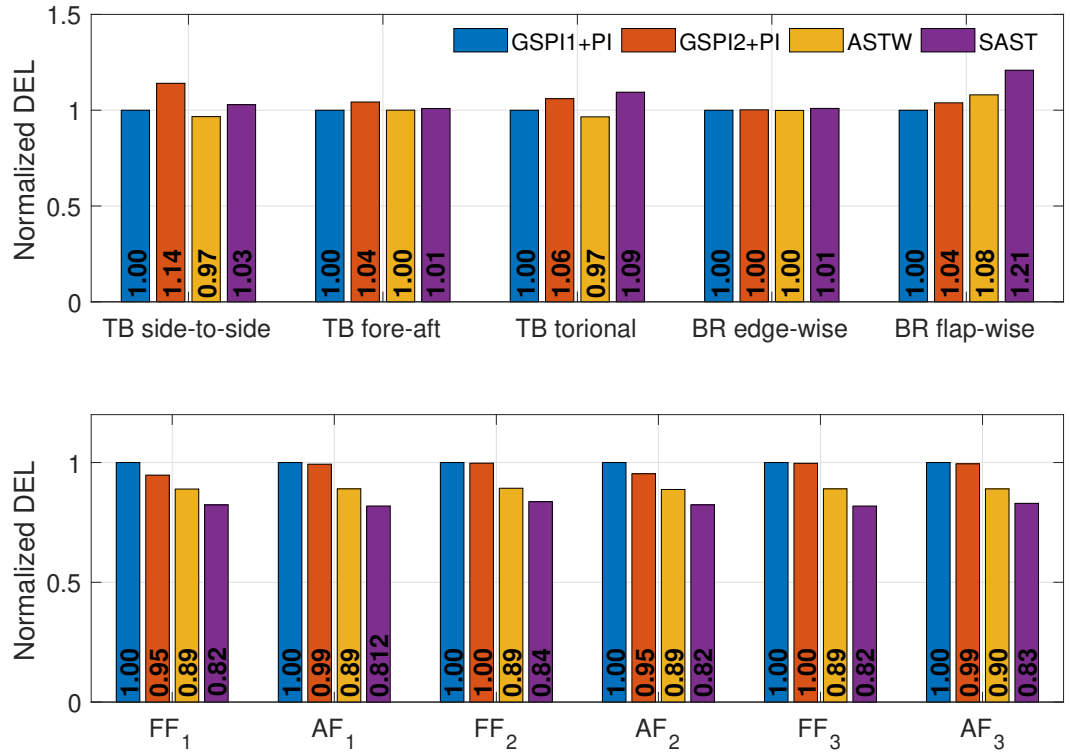

Figure 3.5 – Normalized DEL values of structure loads of GSPI1+PI (blue), GSPI2+PI (red), ASTW (yellow) and SAST (purple) controllers.

pitch actuator, *i.e.* the variations of ASTW and SAST versus GSPI are +119% and +149% respectively (see Figure 3.4). Nonetheless, since the blade pitch saturation and rate limiter are taken into consideration in the simulations, the controllers can be applied in practice.

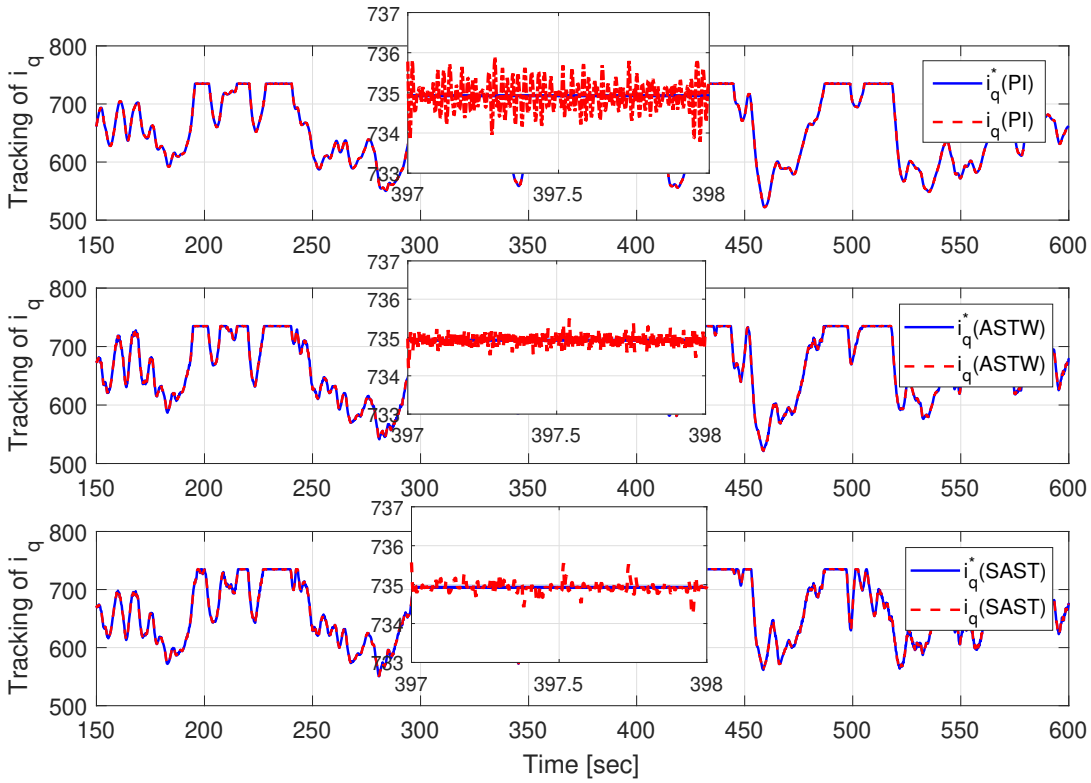

Figure 3.6 – Quadratic current i_q (A) and its reference versus time (sec.), obtained by PI (**top**), ASTW (**middle**) and SAST (**bottom**) controllers.

Concerning the electrical part, Figures 3.6- 3.7 show the tracking of i_q and i_d respectively. Since the generator torque is adjusted by the quadratic current i_q (see (3.9)), the tracking of i_q can be used to evaluate the performance of the torque control. Figures 3.7 and Table 3.5 display information on the tracking errors on both i_d and i_q. It appears that ASTW and SAST controllers allow to keep smaller the tracking error than both PI controllers. So, current (and torque) control is more efficient with super-twisting approach.

As shown by Figure 3.8, the gains of the ASTW and SAST controllers are dynamically adapted in order to keep accurate performances. It appears that all the gains, after a transient, converge towards a "steady state": they are evolving around an average value that is linked to the perturbations and uncertainties. Figure 3.9 shows the stator voltages and currents along the three phases frame

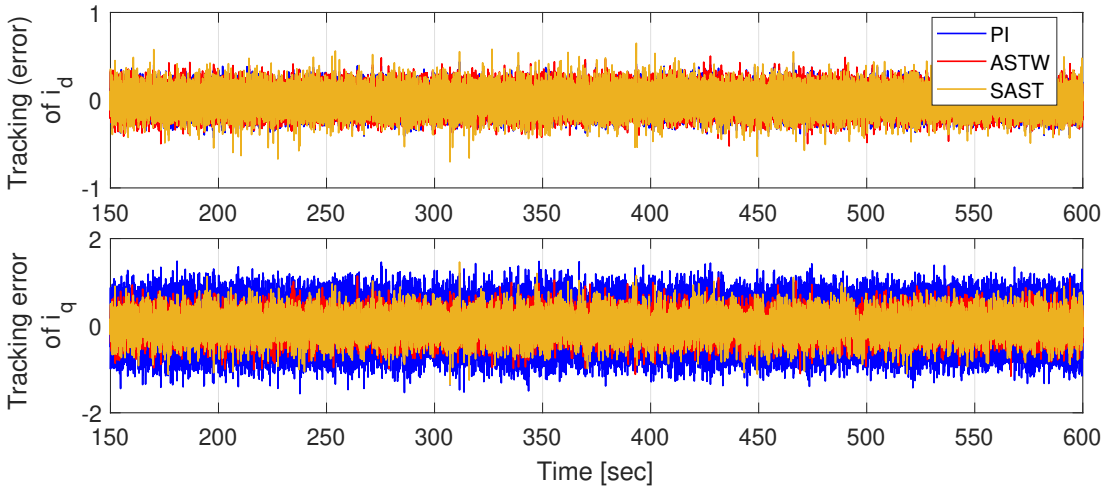

Figure 3.7 – Tracking error of currents i_d (A) and i_q (A) obtained by PI (blue), ASTW (red) and SAST (yellow) controllers versus time (sec.).

Table 3.5 – Mean tracking error of PMSG currents.

Controller	RMS of tracking error of $\boldsymbol{i_d}$	RMS of tracking error of $\boldsymbol{i_q}$
GSPI+PI1	0.0978	0.3596
GSPI+PI2	0.0978	0.3595
ASTW	0.0771	0.1535
SAST	0.0764	0.1512

obtained by both the super-twisting controllers. These signals appear to be realistic. Notice that the use of sliding mode controllers induce no high frequency oscillations (chattering) on these electrical variables.

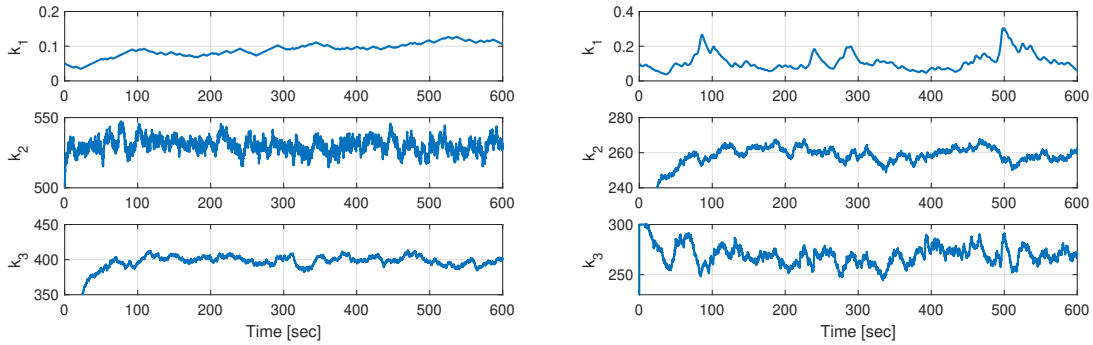

Figure 3.8 – Adaptive gains k_1, k_2 and k_3 of ASTW (**left**) and SAST (**right**) versus time (sec).

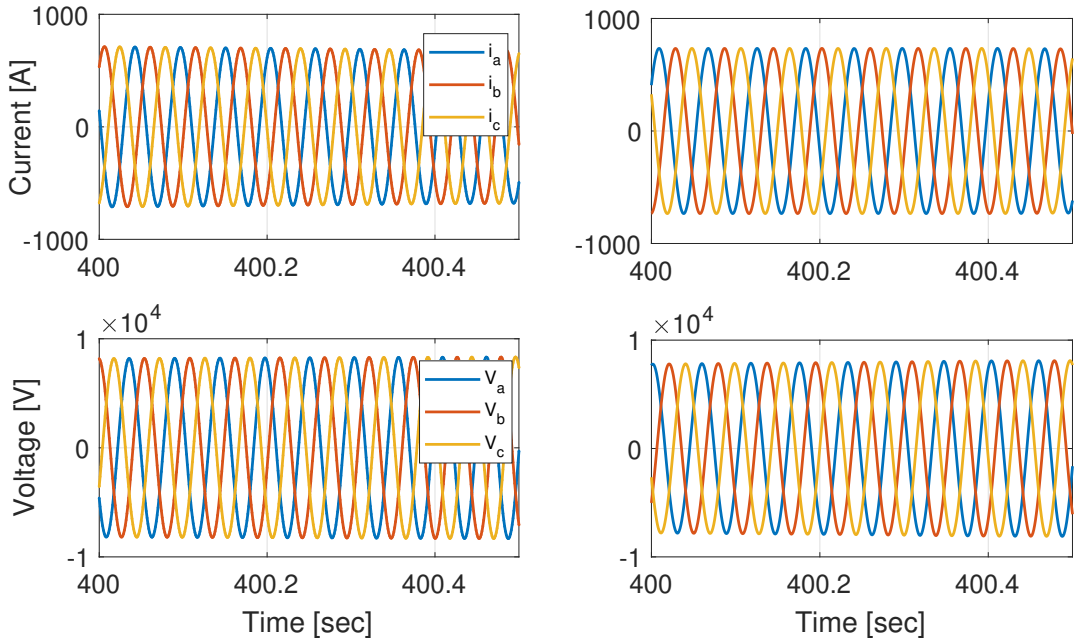

Figure 3.9 – Stator voltages (**top**) and currents (**bottom**) along the three phase frame versus time (sec.), by using ASTW (**left**) and SAST (**right**) controllers.

3.6 Conclusion

In this chapter, super-twisting based controllers with two kinds of gain adaptation algorithms have been for the first time applied to a floating wind turbine in above rated region, equipped by a per-

manent magnet synchronous machine. The control objectives are the regulation of the power output at its rated value and the reduction of the platform pitch motion, meanwhile, reducing the ripple effect of the generator. The two controllers are evaluated on a complete model including hydrodynamics, aerodynamics and electrical dynamics and allow to get better performances comparing with baseline controllers. Furthermore, the controller gains tuning effort is greatly reduced (especially with SAST) because these gains are dynamically adapted with uncertainties and perturbations.

Chapter 4

Individual blade pitch control of FWT

Contents

4.1 Introduction

In the previous chapters, the controllers based on nonlinear approaches (SAST, ASTW,...) have been designed based on the collective blade control technology. Generally, these controllers have better performances in term of control objectives, *i.e.* power regulation and platform pitch reduction than the baseline GSPI. Moreover, structure loads have been also compared with those obtained by the baseline controller and the controllers provide satisfying results. Notice that the load reduction is not a specific control objective; it is checked after the control design in order to make sure that the controllers do not excite large structure loads. In fact, the structure loads are become more and more important with the increasing capacity and flexibility of wind turbines; such loads are harmful to the system, reduce the service life and increase the costs of maintenance (Petrović, Jelavić, and Baotić 2015; Menezes Novaes, Araújo, and Bouchonneau Da Silva 2018). Floating wind turbines,

especially need to withstand wind, waves and complex marine environments as well as the motions excited by the floating structure. All of those factors induce much larger structure loads than conventional onshore wind turbines (Jason Mark Jonkman 2007). Therefore, reducing the fatigue loads is a key-point (E. A. Bossanyi 2003; Menezes Novaes, Araújo, and Bouchonneau Da Silva 2018) for wind turbines. The control strategy must provide an efficient solution for such problems and appears crucial for floating wind turbine systems.

Therefore, besides regulating the power and reducing the platform pitch motion, the controller proposed in this chapter takes the load reduction into consideration. Among the structure loads, the load of blade root, being the source of the loads for the rest of the structures, is one of the most important (Jelavić, Petrović, and Perić 2010). Hence, it is specifically considered as a control objective by introducing an additional control loop based on the IBP control approach. To this end, the CBP controller proposed in Chapter 2 an IBP controller will be used in combination. Part of the modeling presented in Chapter 1 is used for the CBP control, an IBP control model is proposed. Then, ASTW algorithm is used making it possible to meet expectations.

In summary, the main contributions of this chapter are

- modeling of the both CBP control loop and the IBP control loop;
- design of ASTW controllers based on both CBP and IBP approaches;
- analysis of the obtained performances according to FAST/SIMULINK co-simulations.

4.2 System modeling

The main purposes of the controllers designed in this chapter are the limitation of the power at its rated value, the reduction of the platform pitch motion and the attenuation of the blade flap-wise root moment. The two first objectives can be achieved by the CBP control while the third one is fulfilled by IBP control. Since the CBP and IBP controllers can be separately designed as two independent control loops (see details in the sequel), two models are introduced in this section: the first one is the reduced CBP control loop model, whereas the second one is the reduced IBP control loop model which is acting on the behaviour of the blades.

4.2.1 Reduced CBP control model

The CBP model used in this section is the model detailed in Section 1.3.1, that is focused on the platform pitch motion and the rotor speed. Concerning the control objectives of CBP controller,

only 2 DOFs, the rotor rotation and the platform pitch, are considered. Recall here the nonlinear form of the 2 DOFs model (1.13); for a sake of clarity, rewrite (1.13) with new notations as following

$$\dot{x}_C \quad = \quad f_C(x_C, t) + g_C(x_C, t)u_C \tag{4.1}$$

with $x_C = [\varphi \ \dot{\varphi} \ \Omega_r]^T$, φ being the platform pitch angle, $\dot{\varphi}$ the platform pitch velocity and Ω_r the rotor speed, the control input being defined as $u_C = \beta_{col}$. This value is applied at each of the three blades.

4.2.2 Reduced IBP control model

The IBP model is focused on the blade behavior. It is obtained by the FAST linearization process and the MBC transformation algorithm (detailed in the sequel). The control objective of the IBP control loop is to reduce the blade fatigue loads; so, the dynamics of each blade is required. Thus, a 3 DOFs model, including the 1st flap-wise bending mode of each blade, is used for the IBP control loop and reads as

$$\dot{x}_I \quad = \quad A_I(\psi) \cdot x_I + B_I(\psi) \cdot u_I + B_{dI}(\psi) \cdot \delta_{dI} \tag{4.2}$$

with the state vector $x_I = [q^T \ \dot{q}^T]^T$ (q being the enabled DOFs) and the input vector u_I respectively defined as

$$x_I = \begin{bmatrix} q_1 \\ q_2 \\ q_3 \\ \dot{q_1} \\ \dot{q_2} \\ \dot{q_3} \end{bmatrix}, u_I = \begin{bmatrix} \tilde{\beta}_1 \\ \tilde{\beta}_2 \\ \tilde{\beta}_3 \end{bmatrix} \tag{4.3}$$

with q_i (resp. $\dot{q}_i$) ($1 \leq i \leq 3$) being the flap-wise bending deflection (resp. deflection rate) of blade $\#i$. δ_{dI} is the wind disturbance input. Recalling the blade coordinates system in Figure 1.4-left, the flap-wise bending deflection is the deflection along the x_{bi}-axis relative to the pitch axis (see Figure 4.1).

Note that system (4.2) is periodic with respect to rotor azimuth angle ψ; therefore, analysis and control design could be not straightforward. In order to avoid a periodic control design, the solution displayed in Chapter 1 is to average the periodic matrices over ψ. However, in this case, due to the fact that the DOFs (q_1, q_2, q_3 and their derivatives) are in the rotating frame of reference located in each blade respectively, the periodic information in the rotating frame is lost while averaging. Therefore, the multi-blade coordinate (MBC) transformation (G. Bir 2008), also known as *Coleman transformation*, is applied. Such coordinate transformation allows to transform the rotating frame into the non-rotating one. Then, the average process can be performed after the transformation; as a consequence, the periodic information on the blade can be kept.

Figure 4.1 – Blade#1 flap-wise bending deflection.

As shown in Figure 4.2, the rotating blade coordinates system on the left (detailed in Chapter 1) can be transferred by MBC into the fixed coordinates system on the right. This fixed one also known as rotor coordinates, expresses the cumulative behaviour of all of the rotor blades (G. S. Bir 2010). The x_{nr}-axis pointing to the shaft axis, the y_{nr}-axis is horizontal and perpendicular to the x_{nr}-axis and the z_{nr}-axis is vertical upward.

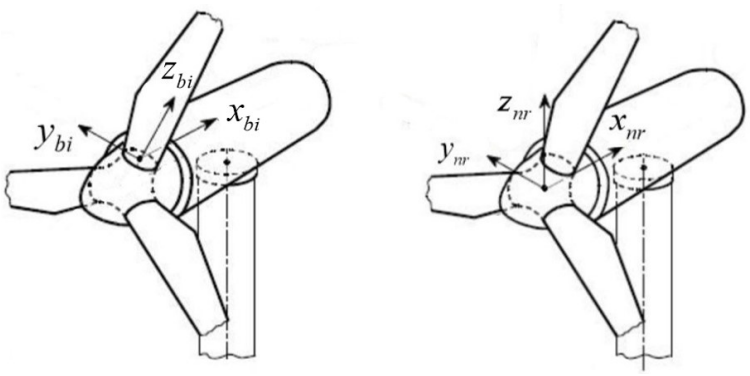

Figure 4.2 – Rotational blade root coordinates system (**left**) and fixed rotor coordinates system (**right**) ($i = \{1,\ 2,\ 3\}$ refers to the i^{th} blade) (Jelavić, Petrović, and Perić 2010).

Consider the following MBC transformation (G. Bir 2008)

$$\begin{aligned} q &= Tq_{nr} \\ u_I &= Tu_{nr} \end{aligned} \tag{4.4}$$

where the notation nr refers to the non-rotating frame; in the current case $q \in \mathbb{R}^3$, $q_{nr} \in \mathbb{R}^2$, $u_I \in \mathbb{R}^3$

and $u_{nr} \in \mathbb{R}^2$. T the transformation matrix reads as

$$T = \begin{bmatrix} cos(\psi) & sin(\psi) \\ cos(\psi + \frac{2\pi}{3}) & sin(\psi + \frac{2\pi}{3}) \\ cos(\psi + \frac{4\pi}{3}) & sin(\psi + \frac{4\pi}{3}) \end{bmatrix} \tag{4.5}$$

Remark 1. *The wind disturbance input vector is not in the rotating frame. Hence, δ_{dI} is not transformed by the MBC.* ■

According to (4.4), one has (G. Bir 2008)

$$\underbrace{\begin{bmatrix} q \\ \dot{q} \end{bmatrix}}_{x_I} = \begin{bmatrix} T & 0 \\ \Omega_r T_1 & T \end{bmatrix} \underbrace{\begin{bmatrix} q_{nr} \\ \dot{q}_{nr} \end{bmatrix}}_{x_{nr}} \tag{4.6}$$

with

$$T_1 = \begin{bmatrix} -sin(\psi) & cos(\psi) \\ -sin(\psi + \frac{2\pi}{3}) & cos(\psi + \frac{2\pi}{3}) \\ -sin(\psi + \frac{4\pi}{3}) & cos(\psi + \frac{4\pi}{3}) \end{bmatrix}. \tag{4.7}$$

Then, dynamics of x_I reads as

$$\underbrace{\begin{bmatrix} \dot{q} \\ \ddot{q} \end{bmatrix}}_{\dot{x}_I} = \begin{bmatrix} T & 0 \\ 0 & T \end{bmatrix} \underbrace{\begin{bmatrix} \dot{q}_{nr} \\ \ddot{q}_{nr} \end{bmatrix}}_{\dot{x}_{nr}} + \begin{bmatrix} \Omega_r T_1 & 0 \\ \Omega_r^2 T_2 + \dot{\Omega}_r T_1 & 2\Omega_r T_1 \end{bmatrix} \underbrace{\begin{bmatrix} q_{nr} \\ \dot{q}_{nr} \end{bmatrix}}_{x_{nr}} \tag{4.8}$$

with

$$T_2 = \begin{bmatrix} -cos(\psi) & -sin(\psi) \\ -cos(\psi + \frac{2\pi}{3}) & -sin(\psi + \frac{2\pi}{3}) \\ -cos(\psi + \frac{4\pi}{3}) & -sin(\psi + \frac{4\pi}{3}) \end{bmatrix} \tag{4.9}$$

Substituting (4.4), (4.6) and (4.8) into (4.2), the linearized model in the rotating frame is transformed into a non-rotating frame system. Then, one has (with $\dim(x_{nr}) = 4$)

$$\dot{x}_{nr} \;=\; A_{nr}(\psi) \cdot x_{nr} + B_{nr}(\psi) \cdot u_{nr} + B_{dnr}(\psi) \cdot \delta_{dI} \tag{4.10}$$

with the transformed matrices $A_{nr}(\psi)$, $B_{nr}(\psi)$ and $B_{dnr}(\psi)$ reading as

$$A_{nr}(\psi) = \begin{bmatrix} T^{-1} & 0 \\ 0 & T^{-1} \end{bmatrix} \left\{ A_I(\psi) \begin{bmatrix} T^{-1} & 0 \\ 0 & T^{-1} \end{bmatrix} - \begin{bmatrix} \Omega_r T_1 & 0 \\ \Omega_r^2 T_2 + \dot{\Omega}_r T_1 & 2\Omega_r T_1 \end{bmatrix} \right\} \tag{4.11}$$

$$B_{nr}(\psi) = \begin{bmatrix} T^{-1} & 0 \\ 0 & T^{-1} \end{bmatrix} B_I(\psi)T, \quad B_{dnr}(\psi) = \begin{bmatrix} T^{-1} & 0 \\ 0 & T^{-1} \end{bmatrix} B_d(\psi) \tag{4.12}$$

By applying the MBC transformation, the system (4.2) in the rotating frame is transformed into the non-rotating frame system (4.10). Therefore, the system metrics can be averaged after the MBC transformation without loss of the periodic information that depends on the rotor azimuth angle ψ. By this way, the controller can be designed in a straightforward way without considering the periodic dynamics. Then, the averaged state space model after MBC transformation reads as

$$\dot{x}_{NR} \quad = \quad A_{NR} \cdot x_{NR} + B_{NR} \cdot u_{NR} + B_{dNR} \cdot \delta_{dI} \tag{4.13}$$

with A_{NR}, B_{NR} and B_{dNR} the azimuth angle averaged state matrix, input matrix and wind input disturbance matrix respectively. For example, when the considered floating wind turbine is operating at a wind speed equal to $18m/s$ and rotor speed equal to its rated value $\Omega_{r0} = 12.1\ rpm$, one has

$$\begin{aligned} A_{NR} &= \begin{bmatrix} 0 & 0 & 1 & 0 \\ 0 & 0 & 0 & 1 \\ -18.7690 & -6.8117 & -5.3371 & -2.5478 \\ 6.8107 & -18.7620 & 2.5502 & -5.3487 \end{bmatrix}, \\ B_{NR} &= \begin{bmatrix} 0 & 0 \\ 0 & 0 \\ -636.8200 & -0.1149 \\ -0.1360 & -638.6200 \end{bmatrix}, B_{dNR} = \begin{bmatrix} 0 \\ 0 \\ -0.0671 \\ 0.17258 \end{bmatrix} \end{aligned} \tag{4.14}$$

As the modeling of Section 1.3.1, among a large operating domain, the model can be written as a class of nonlinear system

$$\dot{x}_{NR} \quad = \quad f_{NR}(x_{NR}, t) + g_{NR}(x_{NR}, t)u_{NR} \tag{4.15}$$

where

- $f_{NR}(x_{NR}, t)$ contains the term $A_{NR}(x_{NR}, t)$ and the term $B_{dNR}(x_{NR}, t) \cdot \delta_{dI}$, the uncertainties of the system and the perturbations introduced by wind, wave and other external environment;

- $g_{NR}(x_{NR}, t) = B_{NR}(x_{NR}, t)$ is the input function;

- $x_{NR} = [q_{tilt}\ q_{yaw}\ \dot{q}_{tilt}\ \dot{q}_{yaw}]^T$ with q_{tilt} and q_{yaw} the tilt (about the y_{nr}-axis) and yaw (about the z_{nr}-axis) components of blade flap-wise deflections respectively;

- β_{yaw} and β_{tilt} are the fictitious yaw and tilt component of blade pitch angles.

Note that the MBC transformation also allows to decouple the IBP control that is focused on load reduction, from the CBP control (Karl Stol et al. 2009). Furthermore, the control based on MBC transformation has almost same results as the periodic control (Karl Stol et al. 2009), but with reduced complexity.

4.3 Control problem statement

Recall that the control objectives in this chapter are to ensure the power output at rated meanwhile reducing the platform pitch motion and reducing the flap-wise load of blades. In the previous sections, both the first control objectives (power, platform pitch motion regulation) are achieved by collective blade pitch control. Here, the blade load (especially the blade flap-wise load) alleviation is also considered and can be ensured by separately adjusting the pitch angle of each blade, namely, by using the individual blade pitch control (E. A. Bossanyi 2003; Selvam et al. 2009; Van Engelen 2006).

The overall control scheme is shown in Figure 4.3. The IBP adjustment angles $\tilde{\beta}_1$, $\tilde{\beta}_2$ and $\tilde{\beta}_3$ are added to the CBP control input β_{col} but have a limited effect on the global behaviour of the power and platform pitch motion; in other words, there is a very reduced coupling between the CBP and IBP control (E. A. Bossanyi 2003; Jelavić, Petrović, and Perić 2010). Hence, these latter can be separately designed as two independent control loops while achieving their own control objectives.

4.3.1 Collective blade pitch control

The task of CBP control loop is to regulate power at rated P_0 meanwhile reducing the platform pitch motion. In this chapter, the generator torque is supposed to be fixed at its rated value Γ_{g0}, the objective being to focus the attention on the control of the hydrodynamic part of the wind turbine. As detailed in Section 2.2, define the desired rotor speed Ω_r^* as a function of platform pitch velocity

$$\Omega_r^* \quad = \quad \Omega_{r0} - k\dot{\varphi},\ k > 0 \tag{4.16}$$

Therefore, the controlled output associated to the system (4.1) is defined as

$$y_C \quad = \quad \Omega_r - \Omega_r^* \tag{4.17}$$

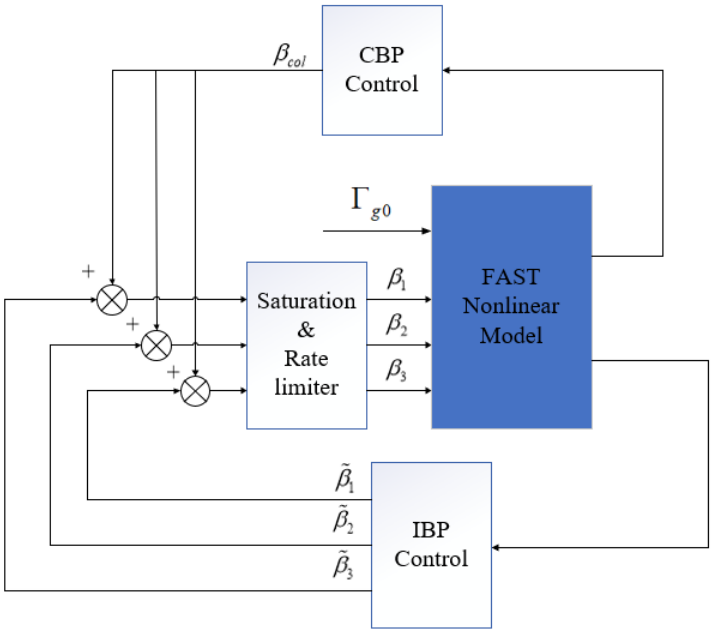

Figure 4.3 – Control scheme of the whole closed-loop system.

4.3.2 Individual blade pitch control

The rotor of wind turbine transforms the wind power into aerodynamic torque that drives the generator; at the same time, partial wind energy is transformed into thrust on the rotor that induces *load*. Due to the wind shear, tower shadow and turbulence, the wind speed and direction are varying across the rotor plane; these factors cause additional loads on the blades. These loads are related with the frequency of the rotor speed and can be decomposed along different modes, the main one being at the rotor speed frequency - this mode is denoted the *1p*-mode (*once-per-revolution*-see Figure 4.7). Other modes are existing at multiples of rotor speed and are denoted $2p$, $3p$ ... (E. A. Bossanyi 2003). The reduction of the $1p$-mode for each blade appears being a main objective of IBP control.

In this regard, the flap-wise bending moments (the moments about y_{bi}-axis see Figure 4.2) of each blade M_1, M_2 and M_3 are considered as the outputs of IBP control loop. Since the these moments are in the rotating blade coordinates system, MBC transformation is used. As detailed previously, the outputs M_1, M_2 and M_3 in the rotating frame can be transformed into the non-rotating frame. Then, one gets an output vector $y_{NR} = [M_{tilt}\ M_{yaw}]^T$, M_{tilt} (about the y_{nr}-axis see Figure 4.2) and M_{yaw} (about the z_{nr}-axis see Figure 4.2) respectively the tilt and yaw component of blade root flap-wise moment. As shown in (N. Wang, Wright, and Johnson 2016; Xiao, Yang, and Geng 2013),

among a large operating domain, this output can be written as

$$y_{NR} = h_{NR}(x_{NR}, t) + l_{NR}(x_{NR}, t)u_{NR}. \tag{4.18}$$

Remark 2. *Notice that the output y_{NR} depends on the control input vector u_{NR}; in this case, the relative degree of system* (4.15) *with output y_{NR} equals to 0.* ■

The main idea of IBP control is to force the magnitudes of M_{yaw} and M_{tilt} close to *zero* that reduces the blade flap-wise loads. MBC approach allows the decoupling between the IBP control that is responsible for load reduction, and the CBP control. Furthermore, it has been shown (E. A. Bossanyi 2003) that M_{yaw} and M_{tilt} can be treated independently by β_{yaw} and β_{tilt} respectively, *i.e.* it is possible to use two controllers for M_{yaw} and M_{tilt} alleviation, respectively.

Note that the following inverse MBC transformation should be applied after the controllers design in order to generate IBP control inputs $\tilde{\beta}_1$, $\tilde{\beta}_2$ and $\tilde{\beta}_3$ (see Figure 4.4)

$$\underbrace{\begin{bmatrix} \tilde{\beta}_1 \\ \tilde{\beta}_2 \\ \tilde{\beta}_3 \end{bmatrix}}_{u_I} = T \underbrace{\begin{bmatrix} \beta_{yaw} \\ \beta_{tilt} \end{bmatrix}}_{u_{NR}} \tag{4.19}$$

4.3.3 Overall control scheme

By a structural point-of-view, the overall control scheme is the combination of CBP and IBP control strategies (see Figure 4.3). Then, the overall control system design process can be summarized as follows

- design the CBP control for regulation of the power and reduction of the platform pitch motion;
- transform the three flap-wise blade flap-wise bending moments M_1, M_2 and M_3 into the fictitious ones M_{yaw} and M_{tilt}, design the control loop that provides β_{yaw} and β_{tilt} respectively, and obtain the components $\tilde{\beta}_1$, $\tilde{\beta}_2$ and $\tilde{\beta}_3$ thanks to the inverse MBC transformation;
- the *real* blade pitch angles β_1, β_2 and β_3, that are the "real" control inputs are equal to the sum of β_{col} with $\tilde{\beta}_1$, $\tilde{\beta}_2$ and $\tilde{\beta}_3$ respectively.

4.4 Control design

As detailed in the previous Section, the control scheme includes two control loops

- the first one is the CBP control loop focusing on the control of rotor speed and platform pitch motion;
- the second one is the IBP control loop producing an additional term to each blade pitch angle in order to reduce the variation of blade root flap-wise bending moments.

These two control loops can be independently designed (Jelavić, Petrović, and Perić 2010; E. A. Bossanyi 2003) as following.

CBP control loop

Recall that the relative degree of system (4.1) with y_C (4.17) is equal to 1. Therefore, according to Assumption 1, the sliding variable of CBP control can be defined as

$$S_1 = y_C \;=\; \Omega - \Omega^* \;=\; \Omega - (\Omega_r - k\dot{\varphi}) \tag{4.20}$$

IBP control loop

As recalled in Remark 2, the relative degree of system (4.15) with output y_{NR}, is equal to 0. Given that ASTW algorithm must be applied to systems with relative degree equal to 1, consider again the system (4.15)

$$\dot{x}_{NR} \;=\; f_{NR}(x_{NR}, t) + g_{NR}(x_{NR}, t)u_{NR}$$

with

$$y_{NR} \;=\; \begin{bmatrix} M_{tilt} \\ M_{yaw} \end{bmatrix} = h_{NR}(x_{NR}, t) + l_{NR}(x_{NR}, t)u_{NR}$$

A solution consists in defining a dynamic control law by increasing the relative degree of the system. Defining

$$\bar{x}_{NR} \;=\; u_{NR} \tag{4.21}$$

and $v_{NR} = \dot{u}_{NR}$ the *new* control input, system (4.15) can be reformulated as

$$\begin{aligned} \dot{x}_{NR} &= f_{NR}(x_{NR}, t) + g_{NR}(x_{NR}, t)\bar{x}_{NR} \\ \dot{\bar{x}}_{NR} &= v_{NR} \\ y_{NR} &= h_{NR}(x_{NR}, t) + l_{NR}(x_{NR}, t)\bar{x}_{NR} \end{aligned} \tag{4.22}$$

with $v_{NR} = [\dot{\beta}_{tilt}\ \dot{\beta}_{yaw}]^T$ the *new* control input.

Then, the relative degree of (4.22) with respect to $[\dot{\beta}_{tilt}\ \dot{\beta}_{yaw}]^T$ is equal to 1. Therefore, ASTW algorithm can be applied: the sliding variables of IBP loop are defined as $[S_2\ S_3]^T = [M_{tilt}\ M_{yaw}]^T$. Figure 4.4 depicts the IBP control scheme.

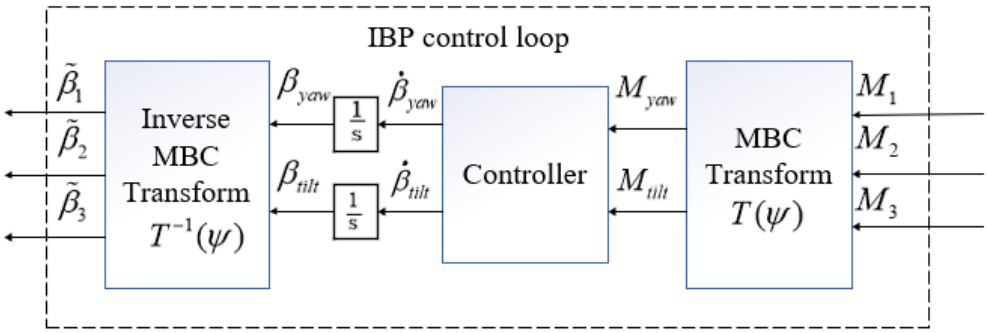

Figure 4.4 – Control scheme of IBP control loop.

Then, one has the sliding variable vector

$$S = \begin{bmatrix} S_1 \\ S_2 \\ S_3 \end{bmatrix} = \begin{bmatrix} \Omega - \Omega_r + k\dot{\varphi} \\ M_{tilt} \\ M_{yaw} \end{bmatrix} \tag{4.23}$$

and its dynamics reads as

$$\dot{S} \ = \ a(\cdot) + b(\cdot)v \tag{4.24}$$

with $a(\cdot)$ and $b(\cdot)$ unknown but bounded functions obtained from (4.1)-(4.22). The control input v is defined as

$$v \ = \ [\beta_{col}\ \dot{\beta}_{tilt}\ \dot{\beta}_{yaw}]^T \ = \ [v_1\ v_2\ v_3]^T \tag{4.25}$$

with

$$\begin{bmatrix} v_1 \\ v_2 \\ v_3 \end{bmatrix} = \begin{bmatrix} -k_{11}|S_1|^{\frac{1}{2}}\text{sign}(S_1) - \int_0^t k_{12}\text{sign}(S_1)d\tau \\ -k_{21}|S_2|^{\frac{1}{2}}\text{sign}(S_2) - \int_0^t k_{22}\text{sign}(S_2)d\tau \\ -k_{31}|S_3|^{\frac{1}{2}}\text{sign}(S_3) - \int_0^t k_{32}\text{sign}(S_3)d\tau \end{bmatrix} \tag{4.26}$$

The gains k_{i1} and k_{i2} ($i = \{1,\ 2,\ 3\}$) are evolving according to adaptation law (2.21) [1].

1. Notice that the main objective of this chapter is to verify that an adaptive super-twisting approach is efficient for the IBP control of FWT. In order to clearly analyze the results of adaptive controller, only the traditional ASTW controller is used.

4.5 Simulations and analysis

As previously, the nonlinear OC3-Hywind 5MW floating wind turbine model from NREL is simulated in this section; such nonlinear model is built in FAST software and is regarded as a benchmark in many of wind turbines studies. Recall that the parameters of this wind turbine are shown in the Table 1.1. In addition, the control is developed in the SIMULINK environment and linked with the FAST model by an s-function. Finally, the co-simulations between FAST and SIMULINK are made on the full DOFs FAST nonlinear model while the control is designed based on the reduced DOFs model as detailed previously. Three controllers are used in the following simulations

- **GSPI-CBP**: the baseline GSPI controller with collective blade pitch control (J. Jonkman 2008b);

- **ASTW-CBP**: the adaptive super-twisting controller with collective blade pitch control; only υ_1 is used of (4.26) (see Chapter 2) given that there is a single control input β_{col};

- **ASTW-CIBP**: The adaptive super-twisting controller that combines collective blade pitch control and individual blade pitch control (4.26). The controller parameters used for this controller being shown in Table 4.1 and the parameter k of sliding variable S_1 in (4.23) is equal to 16.7.

Table 4.1 – ASTW-CIBP controller parameters

Gains	Parameters
k_{11}, k_{12}	$k_{1m} = 10^{-4}$, $\epsilon = 0.03$, $\omega = 1$, $\chi = 0.001$, $\mu = 0.05$, $k = 10^{-4}$
k_{21}, k_{22}	$k_{1m} = 10^{-6}$, $\epsilon = 0.05$, $\omega = 1$, $\chi = 0.003$, $\mu = 0.4$, $k = 0.01$
k_{31}, k_{32}	$k_{1m} = 10^{-6}$, $\epsilon = 0.05$, $\omega = 1$, $\chi = 0.003$, $\mu = 0.2$, $k = 0.01$

The use of these controllers has several objectives: comparison between standard (GSPI) and advanced controllers (ASTW), and comparison between CBP and CBP/IBP control structures. In addition, two cases of wind and wave conditions are simulated in the sequel

- **Scenario 1**. 18 m/s constant wind with still water (*i.e.* no wave);

- **Scenario 2**. 18 m/s stochastic wind with 15% turbulence intensity; irregular wave with significant height of 3.25 m and peak spectral period of 9.7 s (see Figure 3.2).

Note that the wind speed of both scenarios is in above rated region, and all the simulations are

made in 600 seconds and Euler integration with sample time fixed at 0.0125 seconds. Moreover, since there is no blade pitch actuator in the FAST nonlinear model, and in order to be as close as possible from the real system, the blade pitch angle is saturated between [0°, 90°] and the maximum blade pitch rated is limited at $8°/s$ (see Table 1.1).

4.5.1 Scenario 1. Constant wind and still water condition

In this scenario, ASTW-CBP and ASTW-CIBP control strategies are compared, the objective being to check the interest to include a IBP control loop. Firstly, Figure 4.5 displays that both the CBP and CIBP controllers ensure the rotor speed around its rated value 12.1 rpm and limited the platform pitch motion (*i.e.* reduced the platform pitch angle variation). Furthermore, Figure 4.6 shows that the tilt and yaw moment are forced around zero thanks to the CIBP controller; as a consequence, the blade root flap-wise moment are strongly reduced compared to the CBP controller (see Figure 4.6-right).

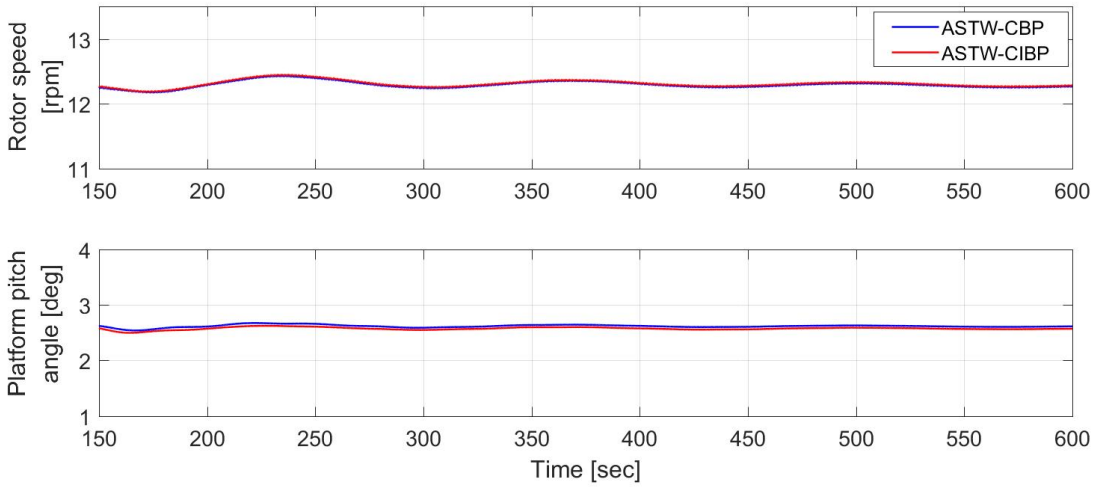

Figure 4.5 – **Scenario 1.** Rotor speed Ω_r and platform pitch angle φ versus time (sec).

Specifically, from the power spectral density (PSD) of blade #1 root flap-wise moment displayed by Figure 4.7, one can find that the load reduction of CIBP control is strongly acting on the $1p$ component of the blade load. Meantime, the rotor speed and platform pitch motion are not affected as shown in Figure 4.5 (the trajectories of CBP and CIBP control are highly coincidence): as mentioned in previous section, the collective pitch control and the individual pitch control are decoupled. Figure 4.8 shows the blade #1 pitch angle obtained with the two controllers. It is clear that CIBP controller is acting much more on the blade pitch angles.

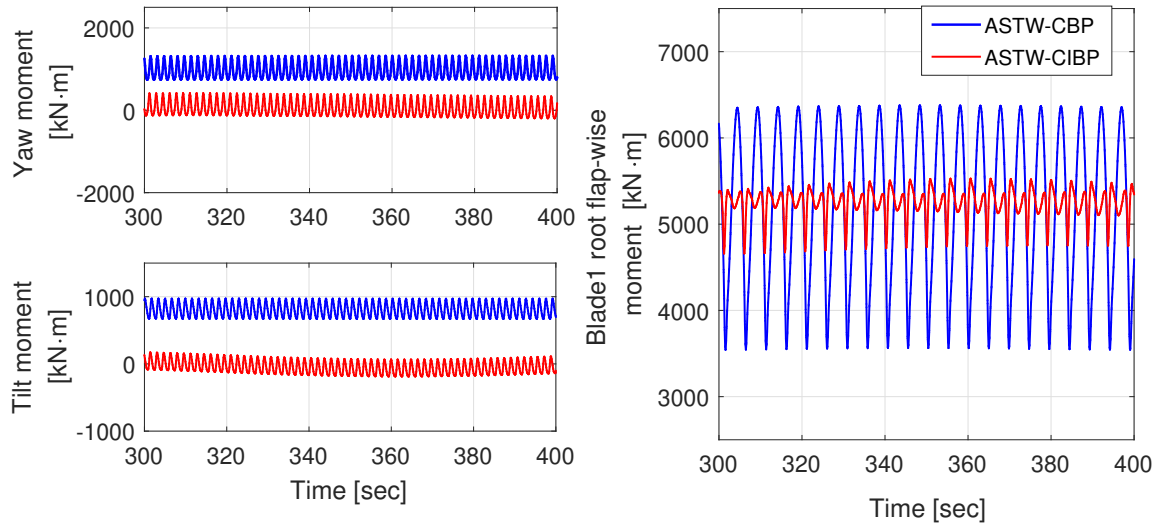

Figure 4.6 – **Scenario 1.** Transformed yaw moment M_{yaw} (**left-top**), tilt moment M_{tilt} (**left-bottom**) and blade #1 root flap-wise moment (**right**) versus time (*sec*).

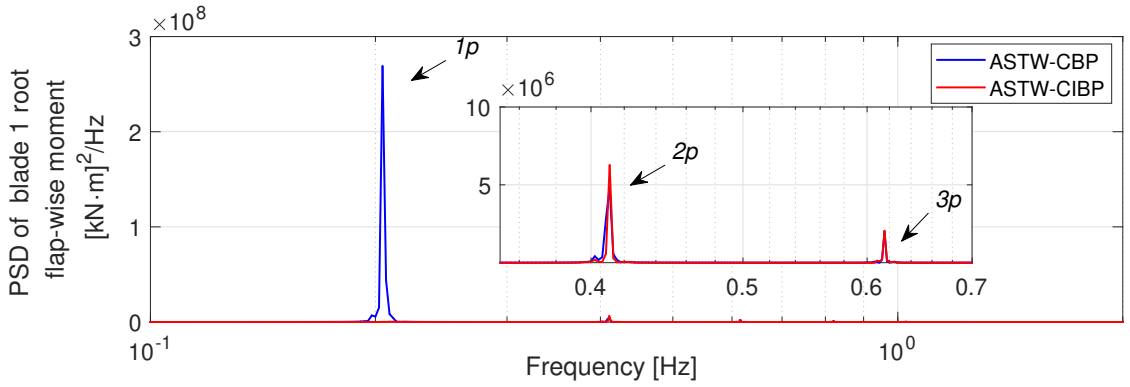

Figure 4.7 – **Scenario 1.** Power spectral density of blade #1 root flap-wise moment.

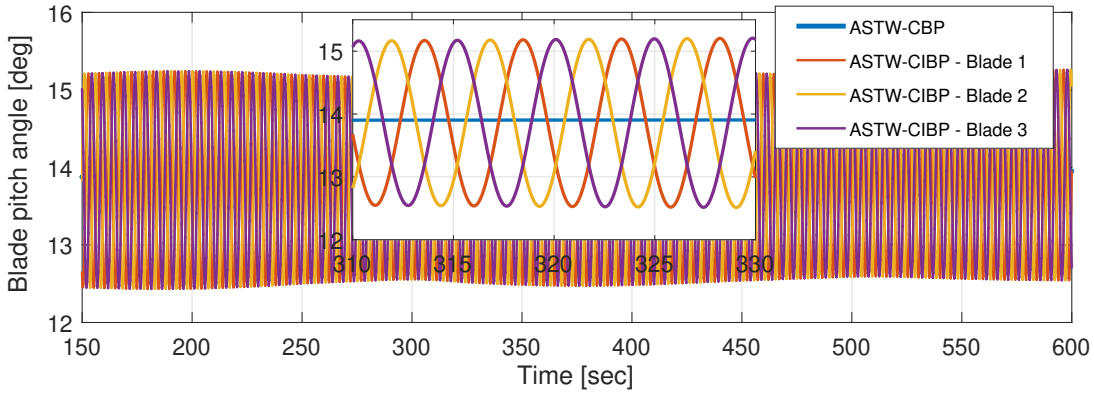

Figure 4.8 – **Scenario 1.** Blade pitch angles versus time (*sec*).

4.5.2 Scenario 2. Stochastic wind and irregular wave condition

Previous scenario shows that both the ASTW controllers allow to achieve all the control objectives in ideal conditions and shows the interest to introduce an IBP control loop. In Scenario 2, a more realistic situation is considered with the 3 following controllers: GSPI-CBP, ASTW-CBP and ASTW-CIBP. By a similar way as previous chapters, the performances of the 3 controllers are compered by using the indices as follows:

- root mean square (RMS) of rotor speed error, power error, platform rotations (roll, yaw and pitch), and platform pitch rate;
- variation (VAR) of the blade pitch angle that is an image of the pitch actuator use;
- damage equivalent load (DEL) of the tower base fore-aft, side-to-side and torsional moments, DEL of averaged blade root flap-wise and edge-wise bending moments of the three blades, and DEL of mooring lines.

As previously, all of these performance indicators are normalized with respect to GSPI-CBP controller (see the red line in Figures 4.9 and 4.10 that represents the normalized values for GSPI-CBP controller). If the value of a normalized indicator is smaller than 1, it means that the performance is better than GSPI-CBP; on the contrary, if the value of a normalized indicator is larger than 1, it means that the performance is worse than GSPI-CBP.

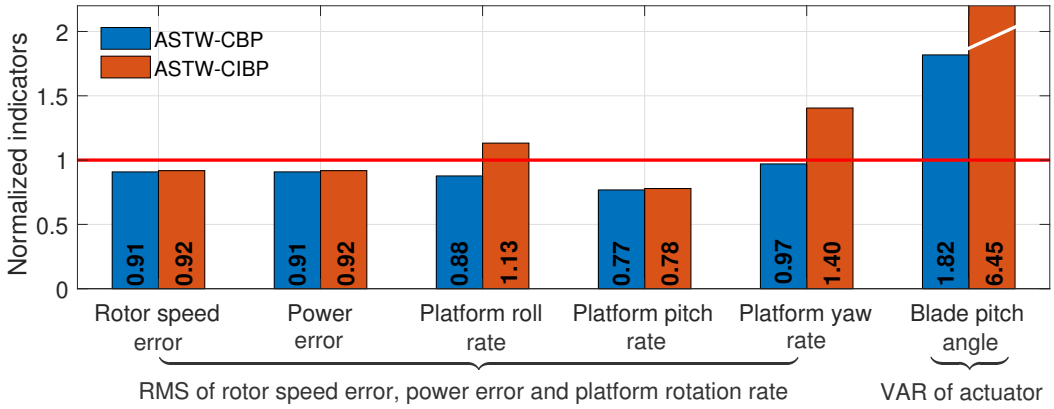

Figure 4.9 – **Scenario 2.** Normalized RMS and VAR values of the 3 controllers.

Figure 4.9 shows that, for two of the main control objectives (rotor speed/ power regulation and platform pitch motion reduction), ASTW-CBP and ASTW-CIBP controllers have similar perfor-

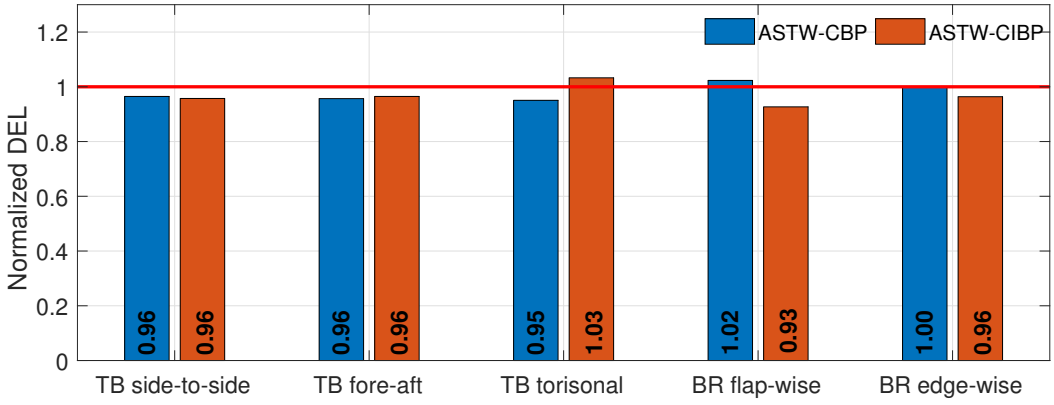

Figure 4.10 – **Scenario 2.** Normalized tower base (TB) and blade root (BR) DEL of the 3 controllers.

mances allowing reduction of rotor speed error (by 8-9%) and platform pitch rate (by 22-23%), versus GSPI-CBP. As previously mentioned, there is no coupling between CBP and IBP control loops; hence, ASTW-CBP and ASTW-CIBP have similar performances on rotor speed and platform pitch rate. As shown by Figure 4.11, the time series of ASTW-CBP and ASTW-CIBP in terms of rotor speed (power) and platform pitch angle are almost identical.

Furthermore, ASTW-CBP controller has also reduced the platform roll and yaw rates; on the contrary, ASTW-CIBP controller induces more important platform roll and yaw rates due to a greatly increased blade pitch actuation (H. Namik and K. Stol 2014). However, given that the magnitudes of platform roll and yaw are relatively small (see Figure 4.11), they have a very limited influence on the stability of the whole system.

Figure 4.10 shows the DEL results: it is clear that ASTW-CBP control law reduces the platform base loads but increases the blade root flap-wise load. For the ASTW-CIBP, the tower base side-to-side and fore-aft loads have similar reductions than ASTW-CBP, while the torsional load increases by 3%. Nonetheless, Figure 4.11 shows that the torsional load is very reduced comparing to the side-to-side and fore-aft loads of tower base: then, an increasing of 3% is meaningless for the load of tower. Furthermore, ASTW-CIBP reduces the blade root flap-wise load ($1p$ load - see Figure 4.12).

Generally, ASTW-CIBP control strategy has not only better performances on the rotor speed (power) regulation and platform pitch motion reduction than GSPI-CBP as ASTW-CBP, but also can reduce the fatigue load of blades, all of which being crucial problems of the floating wind turbine control. Moreover, this controller requires very few knowledge of system model and the controller

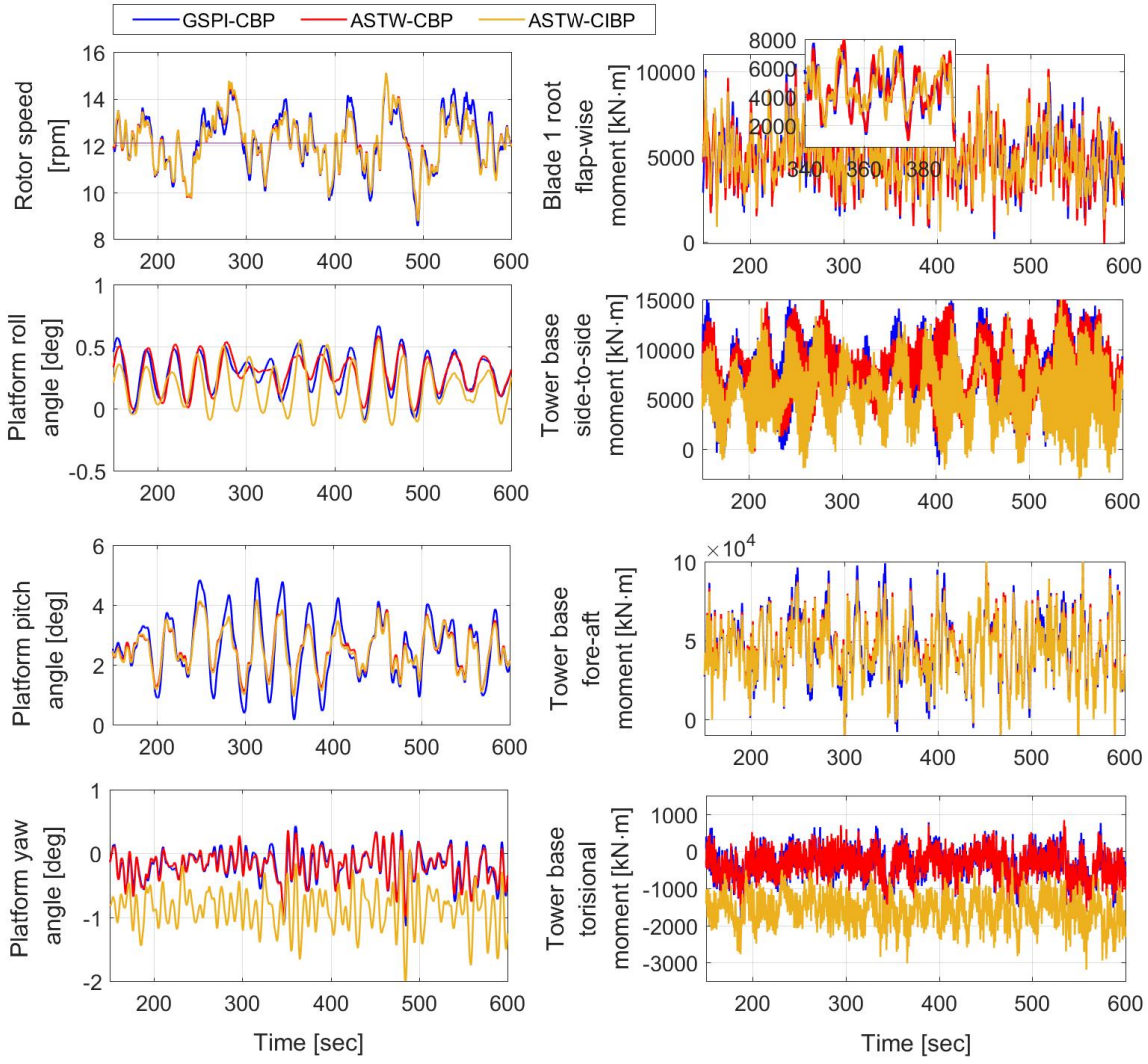

Figure 4.11 – **Scenario 2.** System variables of versus time (*sec*).

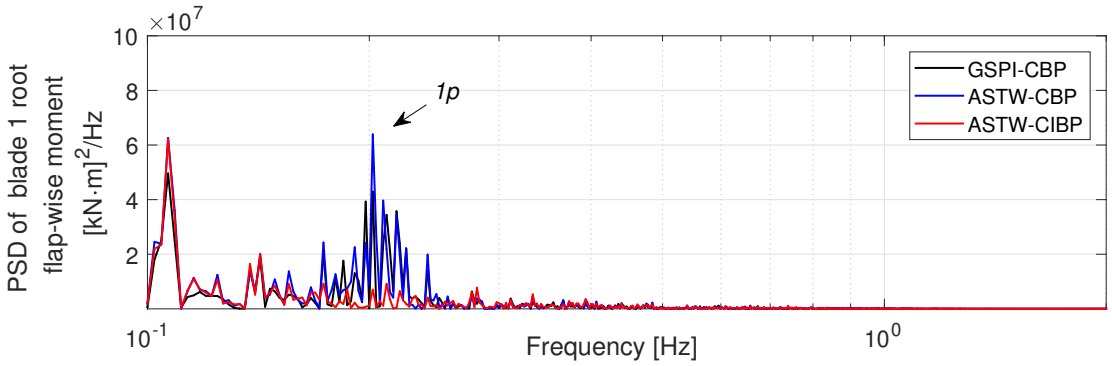

Figure 4.12 – **Scenario 2.** PSD of blade #1 root flap-wise moment.

gains can be dynamically adapted with the uncertainties and perturbations (see Figure 4.13) that largely reduces the parameters tuning effort.

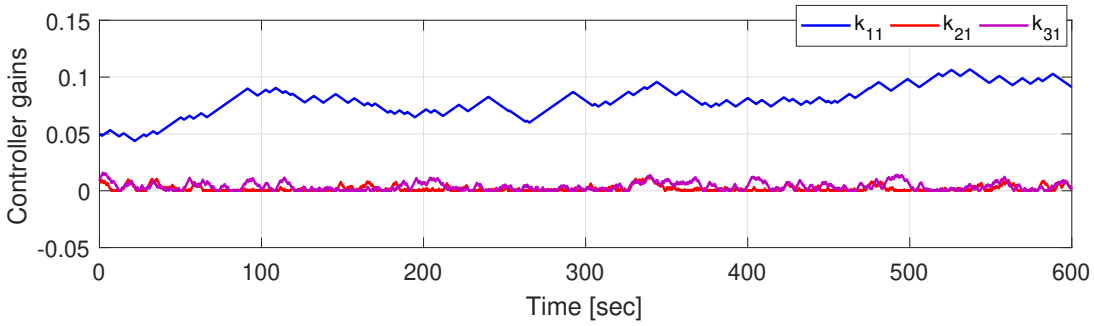

Figure 4.13 – **Scenario 2.** Controller gains of ASTW-CIBP algorithm (4.26) versus time (*sec*).

However, such improvement has a cost that is a more aggressive actuator use, as shown by Figures 4.9 (VAR of actuator) and 4.14: the variation of ASTW-CBP increases by 82% versus CBP-GSPI whereas it is worst with ASTW-CIBP controller. Notice that, given that the dynamics of blade pitch actuators is taken into account in the simulations, such intensive use of theses actuators is practically acceptable.

4.6 Conclusions

Super-twisting algorithms with gain adaptation laws, based on collective/individual blade pitch approach, have been applied to the floating wind turbines control problem in Region III. Such control algorithms strongly reduce the workload of parameters tuning: only few knowledge of system model is required that makes such control strategies well-adapted to the floating wind turbine systems.

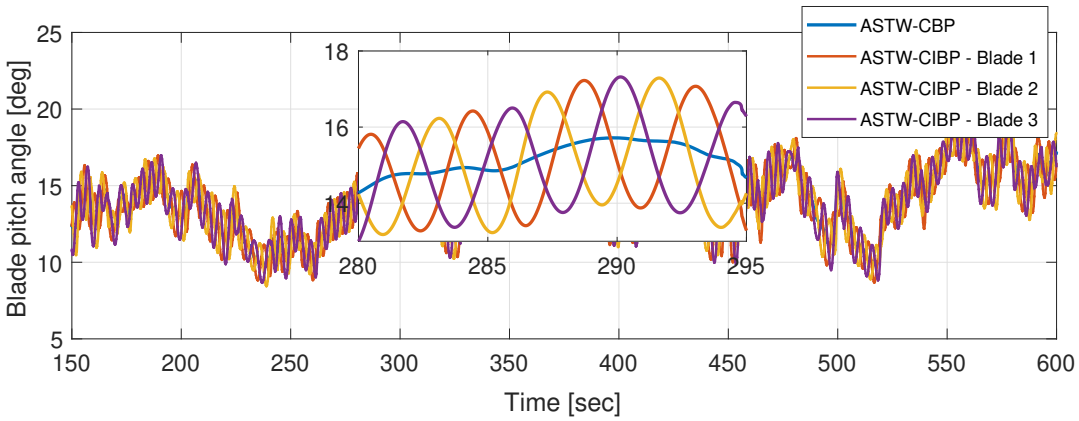

Figure 4.14 – **Scenario 2.** Blade pitch angle of ASTW-CBP and ASTW-CIBP versus time (*sec*).

The control goals are the regulation of the rotor speed, the reduction of the platform pitch motion and the reduction of the fatigue load of the blades. The simulations made on FAST software show that the collective control loop and individual blade pitch control loop are well decoupled by the MBC transformation. Then, the CIBP based ASTW algorithm gives not only better performances on the power regulation and platform pitch motion reduction than CBP controllers, but also provides better performances on the blade load reduction.

Chapter 5

Experiments on reduced scale FWT

Contents

5.1 Introduction

In the previous chapters, high order sliding mode control with gain adaptation algorithms has been applied to floating wind turbine systems. Different control strategies, such as collective blade pitch control, individual blade pitch control and control combined with electric machine have been designed, all of those controllers being evaluated thanks to the co-simulations made by SIMULINK and FAST. Indeed, FAST provides a precise numerical model of FWT that makes it possible to get accurate numerical simulations with time-saving, low cost and easy for control implementation. The numerical based simulation is widely used in FWT researches (see General introduction). Nevertheless, it is still necessary to make experiments in a controlled and repeatable environment before its using control solutions in practical applications (scale 1).

In this chapter, experiments are made on a reduced scaled model of spar-buoy floating wind turbine, on which different controllers are applied. The main contributions of this chapter are therefore

- description of the experimental set-up;
- application of the controllers to the experimental set-up;
- performance comparison and analysis for a set of tuning parameters in specific scenarios.

5.2 Experimental set-up

Comparing with the traditional on-shore wind turbine, the design of an experimental set-up of floating one is much more complex due to the coupling between the hydrodynamics of the platform and the aerodynamics of the rotor. This coupling problem presents several challenges for FWT experimental set-up.

- first-of-all, the scaling issue between hydrodynamic phenomena and aerodynamic phenomena is regarded as the most important one. Different scale schemes should be used for the aerodynamics of rotor and the hydrodynamics of floater. However, these scale schemes cannot be simultaneously used for the FWT experimental set-up since they introduce difficulty in reproducing the coupling between aero-hydro dynamic forces (Jamieson and Hassan 2011; Martin et al. 2012; Bayati et al. 2017);
- then, with the increasing size of the turbines rotor, due to the constraints on the rotor of wind tunnel tests, it is not acceptable to model the rotor with a limited scale ratio.

Hence, in order to deal with the modeling difficulties caused by the coupling aerodynamic forces and hydrodynamic forces, real-time hybrid modeling approach (Arnal 2020; P. Chen, J. Chen, and Hu 2020; Urbán and Guanche 2019) is adopted.

5.2.1 Real-time hybrid method

The hybrid methodology (Carrion and Spencer Jr 2007) reproduces the behaviour of large-scale structure through numerical simulation and physical experiment simultaneously, and has been applied to the FWT system in recent years (Hall and A. J. Goupee 2018; Hall, A. Goupee, and J. Jonkman 2018; Vittori et al. 2018; Arnal 2020). In this work, the experiments are carried out in a wave tank. Then, the hybrid model is composed by a scaled floating structure and a numerical rotor model (modeled by FAST software). The whole system can be defined as a combination of basin experimental set-up and software-in-the-loop (SIL). While the experimental system is scaled in the wave tank, and its dynamics captured by sensors, the numerical model in SIL simulation is

used for the aerodynamic forces calculation in real-time. Then, the calculated aerodynamic forces are applied on the reduced scale system by an actuator [1]. The illustrative drawing of this hybrid method is depicted Figure 5.1.

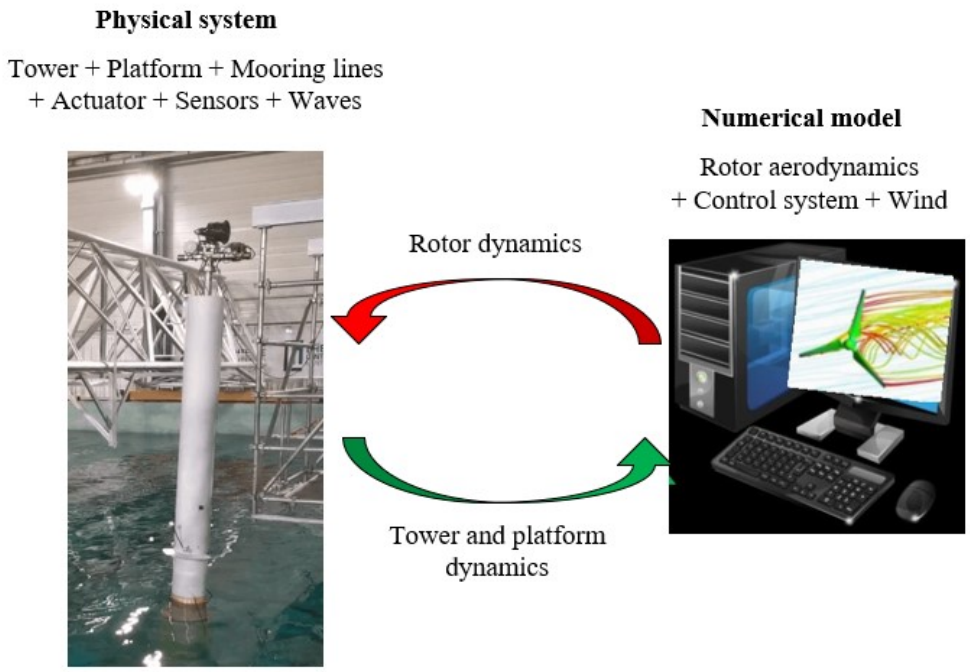

Figure 5.1 – The scheme of software-in-the-loop system, adapted from (Arnal 2020).

The whole experimental system consists of 3 parts

- the physical part in a wave tank, including the floating platform, the mooring lines, the tower, the different sensors and the actuator;
- the numerical part which is used for the calculation of aerodynamics and internal loads acting on the rotor in real-time;
- the real-time data acquisition system and control environment, collecting the measured signals from the physical part, controlling the actuator through the numerical part. It acts as a bridge between physical and numerical parts of data communication.

1. Notice that the actuator of the physical system is used to generate the aerodynamic forces calculated by the numerical model.

5.2.2 Reduced scale system

Experiments are made in the Ecole Centrale de Nantes (ECN) wave tank (see Figure 5.2). The wave tank experiments make it possible to test the response of the FWT hybrid system with different controllers under a repeatable environment. The physical system used in the experiments (Figure 5.2) is a 1/40 scale 10 MW spar floating wind turbine developed by (Arnal 2020) in the SOFTWIND project. This system is carried out for the purpose of developing innovative experimental test bench dedicated to the wave tank testing of floating wind turbines.

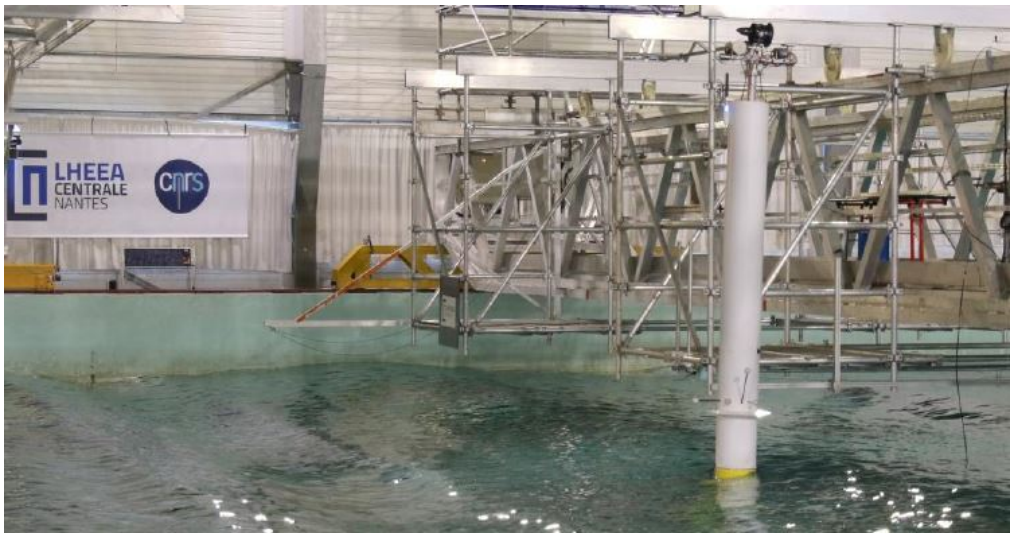

Figure 5.2 – Reduced scale floating wind turbine systen in ECN wave tank (Arnal 2020).

The experimental system is scaled and based on the Technical University of Denmark (DTU) 10 MW onshore wind turbine (C. Bak et al. 2013) and the OC3 5 MW Hywind floating wind turbine (J. Jonkman 2010). The rotor nacelle assembly (RNA) and the tower are based on the full-scale DTU 10 MW wind turbine; the corresponding characteristics of the experimental model such as RNA mass, inertial, dimensions, ... are scaled. A spar-buoy floating structure is considered, and its main properties are based on the OC3 5 MW Hywind floating wind turbine.

The description of the experimental set-up is displayed in Figure 5.3. The tower consists of a flexible mast that is surrounded by an external casing. This casing is rigidly connected to the floater. Three mooring lines are connected between the floater and the bottom of the wave tank in order to limit the motions of the floater. At the top of the model is the RNA that is composed by the actuator and sensors, and the WIFI system that interacting with the real-time numerical model. As recalled in Footnote 1, the actuator allows to generate the aerodynamic forces calculated by the numerical simulations. The main properties of the experimental set-up, the target FWT and the estimated

uncertainties for each features are given in Table 5.1. More detailed descriptions can be found in (Arnal 2020).

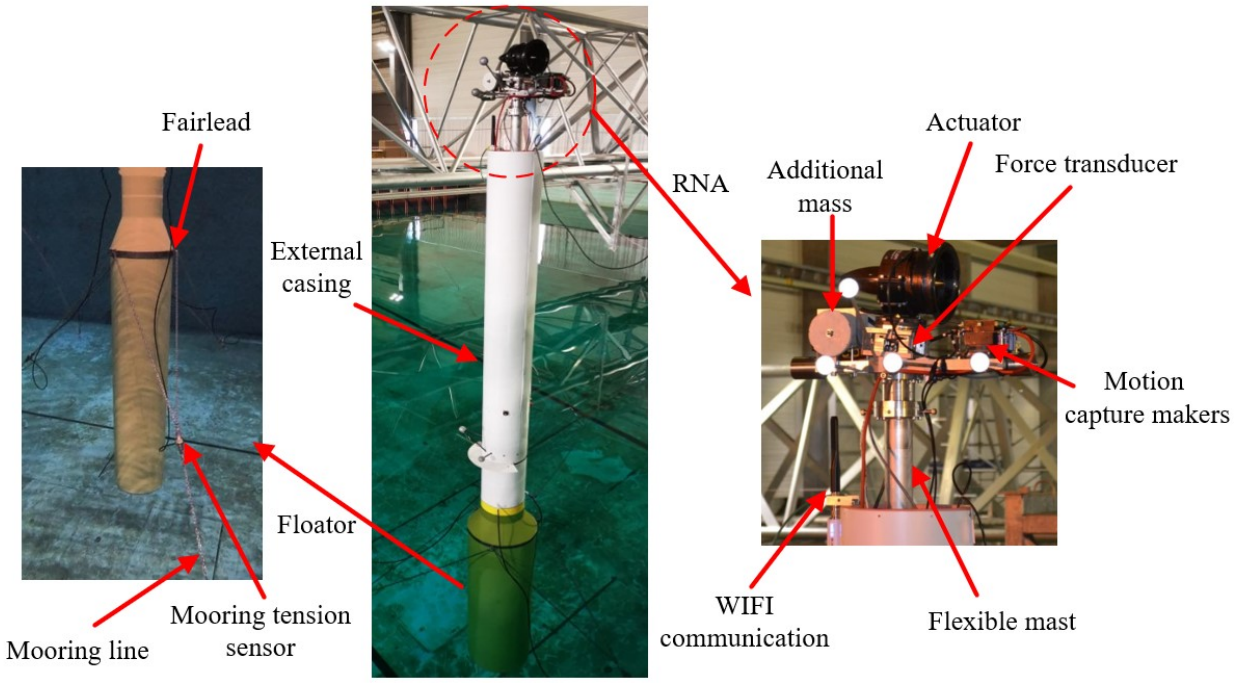

Figure 5.3 – Description of the FWT experimental set-up (Arnal 2020).

5.2.3 Numerical model

While the dynamics of tower, floater and mooring lines are scaled in the wave tank, the aerodynamics are computed numerically and reproduced thanks to the actuator. Considering the numerical computation, it is carried out in real-time by FAST software (see in Chapter 1).

5.3 Controller design

Recall once again that the control objectives of FWT in Region III are to regulate the power at its rated value meanwhile reducing the platform pitch motion. For all the controllers considered in the sequel, constant torque strategy is used, *i.e.* the generator torque Γ_g is fixed at its rated value Γ_{g0}, the power P regulation being regarded through the rotor speed Ω_r regulation according to

$$P = n_g \Gamma_{g0} \Omega_r. \tag{5.1}$$

2*Descriptions	Values		Uncertainties	
	Scale 1:40	Scale 1:1	Scale 1:40	Scale 1:1
RNA mass [kg]	12.45	7.97E+05	0.15	9.6E+03
Hub height above SWL [m]	3.03	121.2	0.01	0.4
Tower height [m]	2.666	106.6	0.005	0.2
Tower mass [kg]	13.48	8.63E+05	0.05	3E+03
Floater mass [kg]	303.8	1.94E+07	0.1	6.4E+03
Anchor depth [m]	5	200	0.01	0.4
Mooring line diameter [mm]	3.7	148	0.05	2
Fairleads depth [m]	-0.335	-13.4	0.005	0.2

Table 5.1 – Main properties of the experimental set-up (Arnal 2020).

Therefore, the control objectives are:

- regulation of the rotor speed Ω_r to its rated value Ω_{r0};
- reduction of the platform pitch motion, *i.e.* forcing the platform pitch rate to zero.

Three controllers will be implemented on the basin experiments:

- a GSPI controller based on the basic DTU (Hansen and Henriksen 2013) approach with re-tuned controller gains;
- a linear–quadratic regulator (LQR) developed by D-ICE company;
- the SAST controller proposed in Chapter 2.

A brief introduction of the GSPI and LQR control as well as some recalls of SAST control are given in the following subsections.

5.3.1 GSPI control

The reduced scale system in the wave tank is based on the DTU 10 MW wind turbine that is installed on a spar-buoy floating platform. In Region III, the DTU Wind Energy controller (Hansen and Henriksen 2013) is selected and applied. This controller is similar as the 5 MW reference wind turbine controller (J. Jonkman, Butterfield, et al. 2009), in which PI control and gain scheduling approaches are combined in order to regulate the power at its rated value. The collective blade pitch control β_{col} is obtained from the generator speed error $e(t)$ with proper tuned controller gains K_p

and K_i and reads as

$$\beta_{col} = K_p e(t) + K_i \int_0^t e(\tau)\mathrm{d}\tau \tag{5.2}$$

with $e(t)$ defined as (with Ω_g the generator speed, and its rated value Ω_{g0}) [2]

$$e(t) = \Omega_g - \Omega_{g0} \tag{5.3}$$

Notice that the control gain setting of the DTU 10 MW controller is efficient for an onshore wind turbines. Those gains have to be re-tuned to avoid negative damping excited by the floating platform. In fact, the onshore gain setting has been tested on the set-up, resulting in a large platform pitch motion and forcing to stop the test (Arnal 2020). Therefore, for the experimental set-up, controller gains tuned for the FWT are considered; a set of gains developed by Olav Olsen 10 MW FWT (Oo-Star) (Yu et al. 2018) is used so as to reduce the platform pitch motion. Furthermore, since the platform pitch natural frequency of Oo-star and the experimental spar-buoy floater are close, the controller gains selection are reasonable.

5.3.2 LQR control

A LQR controller implemented by D-ICE company is tested. Such optimal controller is based on the linear control methodology and has been already applied to the FWT (Hazim Namik, Karl Stol, and J. a. Jonkman 2008; Lemmer, Schlipf, and Cheng 2016). As detailed in Chapter 1, consider the 2 DOFs perturbed state-space linear model around the operating point (x_{op}, u_{op})

$$\dot{x} = A_{Avg} \cdot x + B_{Avg} \cdot u \tag{5.4}$$

with state vector $x = [\varphi\ \dot{\varphi}\ \Omega_r]^T$. $\Delta\varphi$, $\dot{\varphi}$ and Ω_r are the platform pitch angle variation, the platform pitch velocity variation and the rotor speed variation around the values at operating point (denoted by the subscript *op*) respectively. The operating point for rotor speed correspond to a rated rotor speed ($\Omega_{op} = \Omega_{r0}$) whereas the operating point for platform pitch velocity is equal to 0. The control input u of the system is the variation of the blade pitch angle with respect to β_{op}, its value at the operating point. Since all the states can be obtained in experiments, considering the following state feedback control law

$$u = -k_{LQR} \cdot x \tag{5.5}$$

with k_{LQR} the optimal control gain matrix. For the LQR controller, k_{LQR} is calculated such that the quadratic cost function J

$$J = \lim_{t\to\infty} \int_0^T [x^T Q x + u^T R u] dt \tag{5.6}$$

2. Recall that $\Omega_g = n_g \Omega_r$ and $\Omega_{g0} = n_g \Omega_{g0}$. As a consequence, this controller also regulates the rotor speed.

is minimized with Q and R the weighting matrices on the state vector x and input u respectively.

Once the controller gain k_{LQR} are optimally calculated, the control (5.5) forces the state vector x to the operating point. However, notice that the control (5.5) is carried out based on the linearized model that obtained around a single operating point, and such operating point depends on the wind speed and rotor speed (see Chapter 1). As a linear controller, the LQR control will lose its efficiency once the wind turbine is running away from the operating point. As a consequence, the controller gain k_{QR} need to be re-tuned under different wind speeds in order to keep high performances. Namely, in Region III, the LQR control reads as

$$u(t) \quad = \quad -k_{LQR}(t) \cdot x(t) \tag{5.7}$$

with $k_{LQR}(t)$ varying with the wind speed. As far as authors' knowledge, hundreds of controller gains have been tuned by D-ICE company in order to have targeted performances.

5.3.3 SAST control

In order to evaluate the performances of adaptive high order sliding mode algorithms on the experimental set-up, the simplified version of adaptive super-twisting (SAST) control displayed in Chapter 2 is selected; the main reason of this choice is that this control law is much easier for implementation. Notice that the adaptive super-twisting (ASTW) controller is also used in the experiment; however, the performances are not satisfied since the parameters are not well tuned, the results of ASTW being not shown in this work [3].

Recalling Chapter 2, the rotor speed regulation and the platform pitch reduction are achieved by taking the advantage of the physical characteristics of the FWT, defining the desired rotor speed Ω_r^* as a function of platform pitch velocity $\dot{\varphi}$

$$\Omega_r^* \quad = \quad \Omega_{r0} - k\dot{\varphi} \tag{5.8}$$

Then, the control output y reads as

$$\begin{array}{rcl} y & = & \Omega - \Omega_r^* \\ & = & \Omega_r - \Omega_{r0} + k\dot{\varphi} \end{array} \tag{5.9}$$

with k a positive constant. From (1.9)-(1.13), the relative degree of the output y with respect to

3. The current work had very limited time to test different controllers with different parameter tuning. Finally, no suitable ASTW parameters have been found.

β_{col} equals 1. Consequently, the sliding variable S is defined as

$$S = y \tag{5.10}$$

Therefore, according to the SAST algorithm detailed in Chapter 2, the control input reads as

$$\beta_{col} = -2L|S|^{\frac{1}{2}} \cdot \text{sign}(S) - \int_0^T \frac{L^2}{2} \cdot \text{sign}(S)dt \tag{5.11}$$

with L derived from the following dynamics ($L(0) > L_m$)

$$\dot{L} = \begin{cases} L\left(|S| - \mu\right), & \text{if } L > L_m \\ L_m, & \text{if } L \leq L_m \end{cases} \tag{5.12}$$

with μ the accuracy and L_m a small positive value making the controller gains smoothly and slightly increasing.

5.4 Experimental results and analysis

Before making basin experiments, the full scale experimental FWT is modeled thanks to the FAST code, and the numerical simulations are validated on FAST/SIMULINK environment. Such simulations are made in order to find an appropriate parameters tuning for the basin experiments. Table 5.2 shows the features of the FWT model. The SAST is tuned as $\mu = 0.1,\ L_m = 0.0001$ and the parameter k in (5.9) is equal to 10.

Description	Value
Rated rotor speed Ω_{r0}	9.6 rpm
Cut-in, rated, cut-out wind speed	4 m/s, 11.4 m/s, 25 m/s
Gear box ratio n_g	50
Maximum blade pitch rate	$\pm 8°$/s

Table 5.2 – Properties of the FAST FWT model.

All the controllers have been implemented by D-ICE engineering on an industrial PC. In the following subsection, two scenarios of experiments are made under different wind and wave conditions

- **Scenario 1:** SAST controller is used. The purpose of this scenario of test is to ensure that the proposed SAST controller can be successfully applied to the experimental set-up. Thus, the experiments are made under very simple wind and wave conditions: step wind and still water;

- **Scenario 2:** GSPI, LQR and SAST controllers are used. All these controllers are applied on the set-up under stochastic wind and irregular wave in order to evaluate their control performances in "real" conditions.

Notice that, all the comments are made in the sequel on the results obtained with tuning parameters and specific scenarios. Conclusions can not be generalized to all the possible conditions.

5.4.1 Scenario 1. Step wind and still water conditions

Figure 5.4 shows of the wind speed profile used during the experiments: the wind speed varies within Region III from 12 m/s to 25 m/s.

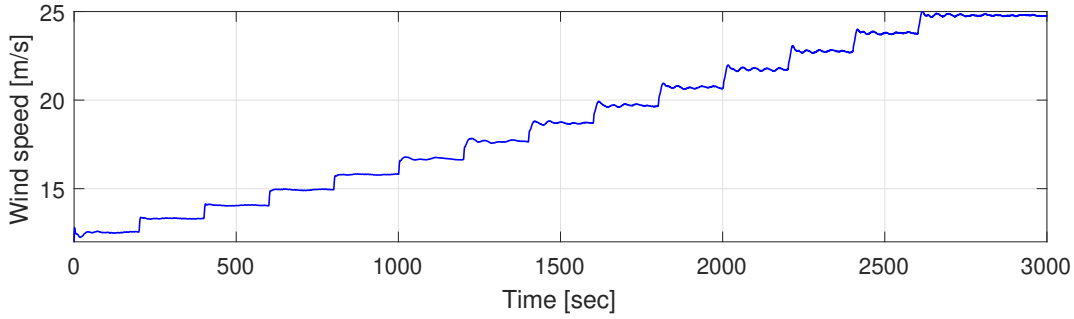

Figure 5.4 – **Scenario 1.** Wind profile (m/s) versus time (sec).

Figure 5.5 shows the evolution of rotor speed, platform pitch angle and its velocity and blade pitch angle. It is clear that the SAST controller allows to regulate the rotor speed at a value close to the rated one (9.6 rpm). The platform pitch rate is maintained around zero and has small variations, namely, the platform pitch motion is reduced. When the wind speed changes (Figure 5.4), some fluctuations in the rotor speed appears but after a transient time, the response of rotor speed converges close to the desired value. Moreover, since the platform pitch motion is limited, the platform pitch angle converges to a certain value at each wind speed with small fluctuations. In summary, under step wind condition and still water, the controller is able to achieve the control objectives among the whole Region III.

5.4.2 Scenario 2. Stochastic wind and irregular wave condition

In this scenario, the three controller, GSPI (DTU developed controller with FWT tuning), LQR (developed by D-ICE company) and SAST, are tested in the same stochastic wind and irregular wave conditions as shown in Figure 5.6. The wind and wave features are as following

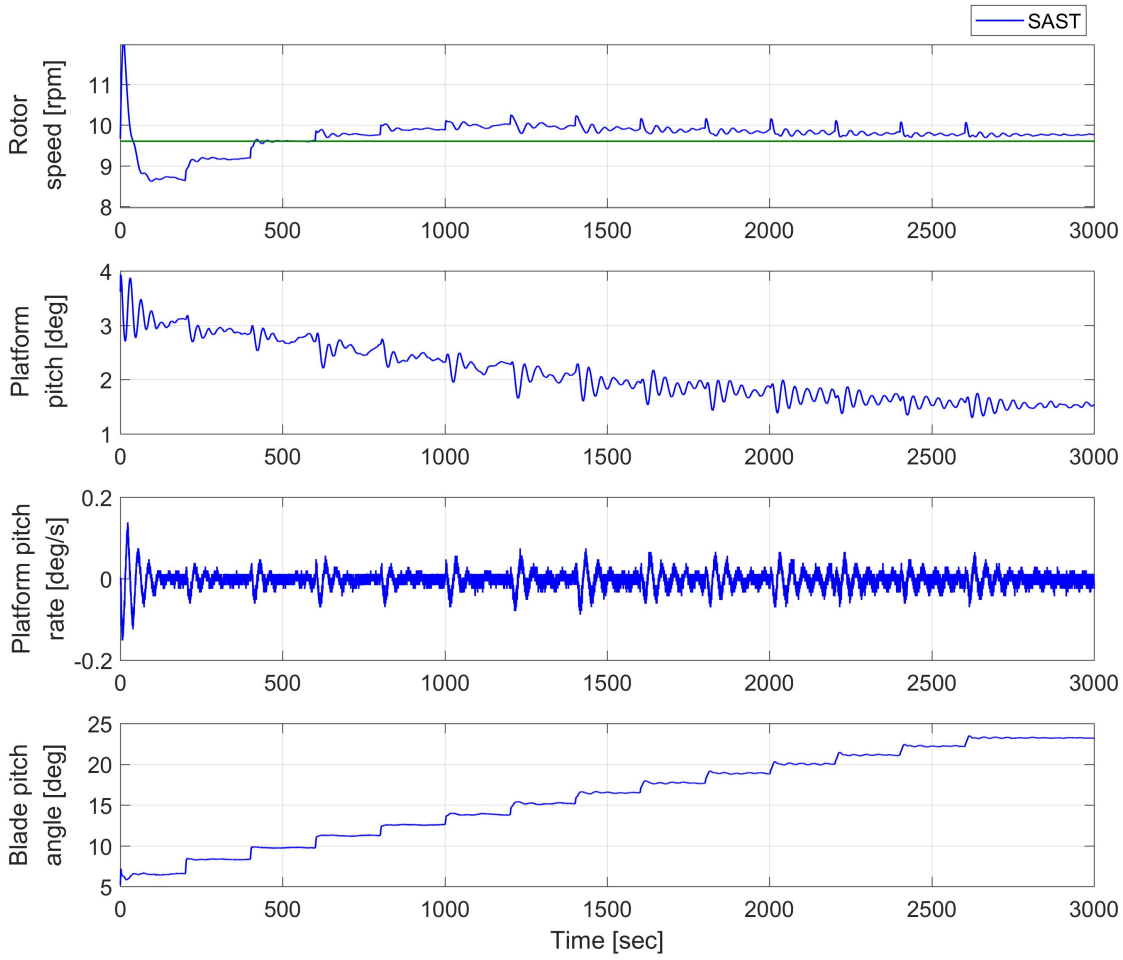

Figure 5.5 – **Scenario 1.** Measured variables of the FWT versus time (*sec*), obtained by SAST control. The green line in the first sub-figure indicates the rated rotor speed (9.6 *rpm*).

- $14m/s$ stochastic wind with 9% turbulence intensity;
- irregular wave with significant height of $3m$, peak spectral period of $12s$.

Recall that the tests have been made with a set of tuning parameters for each controller, and in some specific conditions.

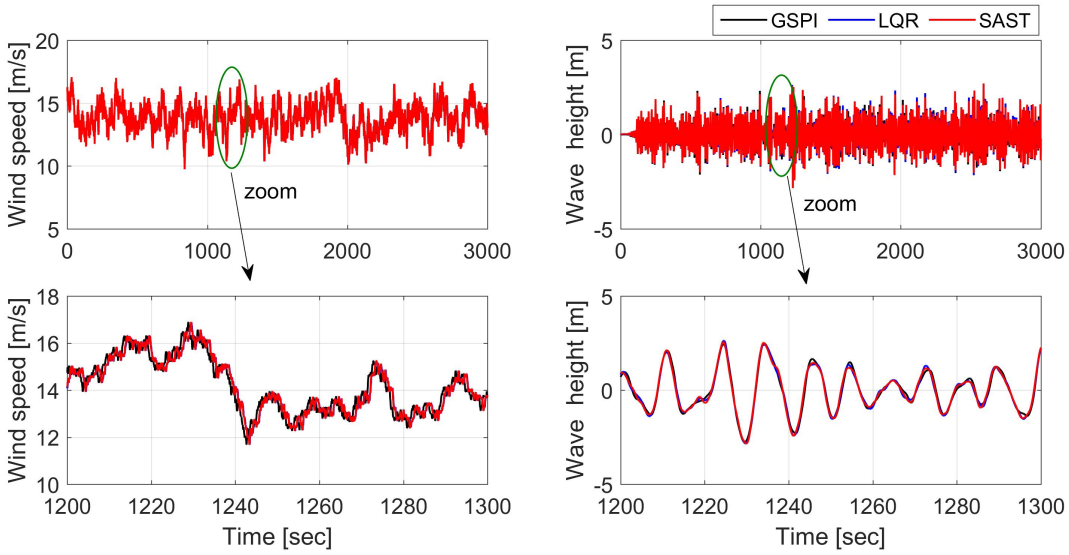

Figure 5.6 – **Scenario 2.** Wind speed (**left**-m/s) wave height (**right**-m) versus time (sec).

Figures 5.7 and 5.8 display rotor speed, blade pitch angle, platform motions and their rates for the three controllers. It is clear from these two figures that, firstly, the rotor speed responses obtained by LQR and SAST controllers have smaller fluctuations around the rated speed than the GSPI control. LQR and SAST controllers maintain the platform roll around a smaller value comparing with GSPI. For the platform roll and pitch angles, LQR and SAST controllers have smaller fluctuations than GSPI. Furthermore, they allow to get smaller roll and pitch rates. However, considering the blade pitch angle, the LQR control has much larger oscillations than the GSPI and SAST controllers [4].

In order to have more precise and straightforward results comparison, the performances of the controllers are evaluated through the indicators

- root mean square (RMS) of rotor speed error from its rated value;

4. Notice that LQR controller has been tested by D-ICE in other conditions with other tuning parameters, and has allowed to get better results.

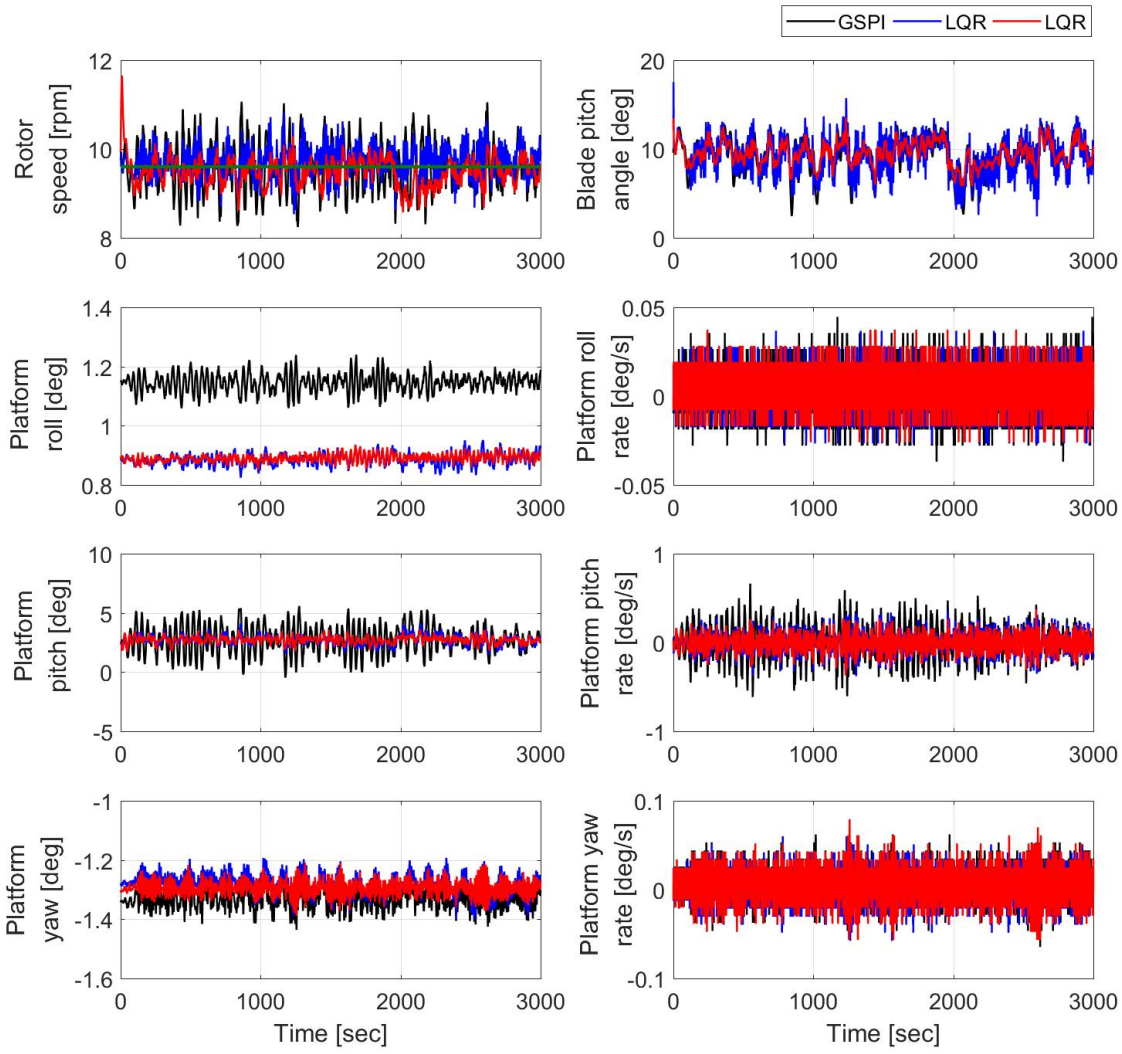

Figure 5.7 – **Scenario 2.** Measured variables of the experimental set-up versus time (*sec*), obtained by GSPI (black), LQR (blue) and SAST (red). The green line in the first sub-figure indicates the rated rotor speed (9.6 *rpm*).

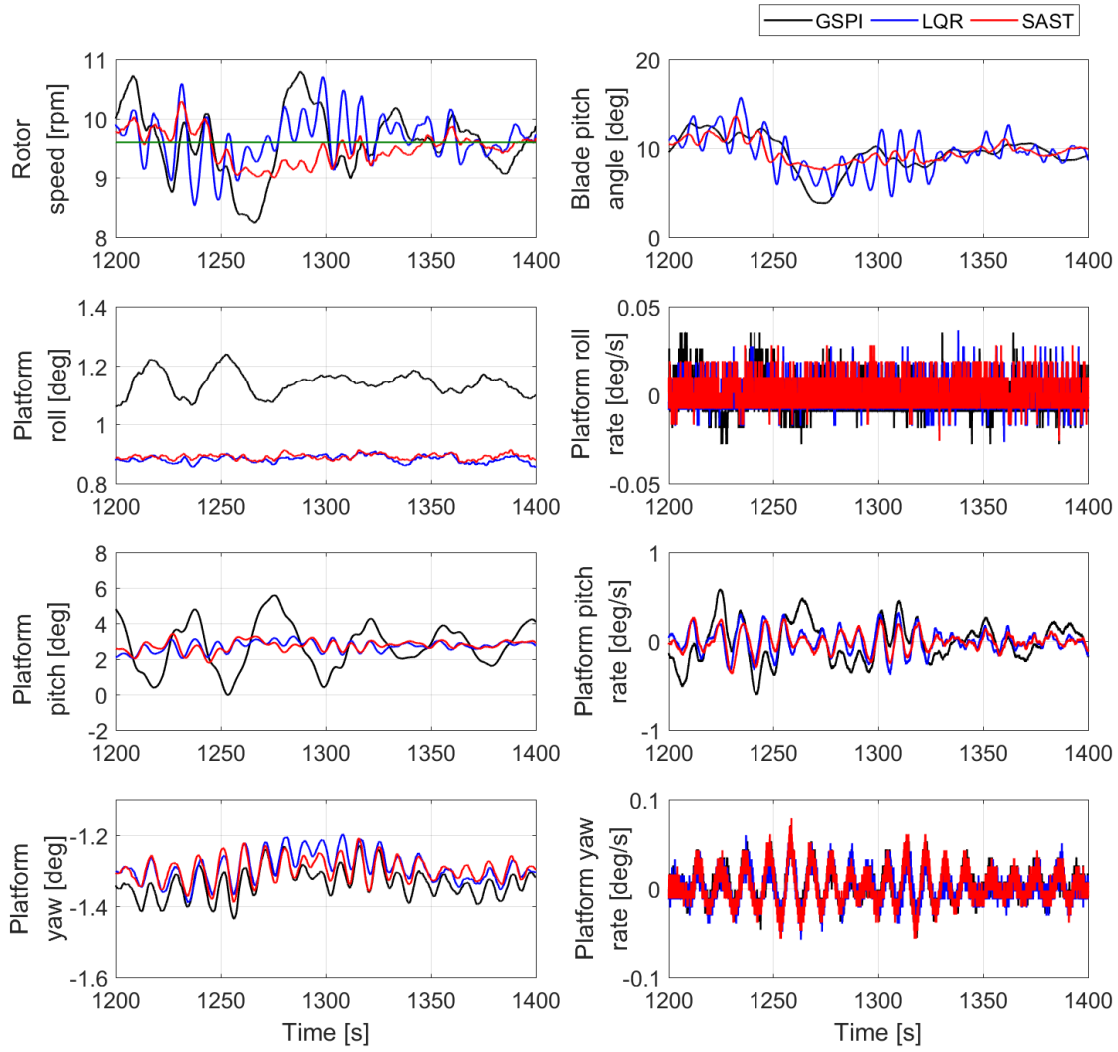

Figure 5.8 – **Scenario 2.** Zoom on measured variables of the experimental set-up displayed in Figure 5.7.

- RMS of platform motions and their rates;
- variation (VAR) of blade pitch angle.

All of those performance indicators are normalized with respect to the performances of GSPI control: the performance indicators of the GSPI controller are equal to 1. If the value of a normalized indicator is smaller than 1, it means the performance is better than GSPI; on the contrary, if the value of a normalized indicator is larger than 1, it means the performance is worse than GSPI. As shown in Figure 5.9, comparing with GSPI control, SAST and LQR strategies have better performances on the main control objectives: LQR control reduces the rotor speed error and platform pitch rate by 38% and 43% respectively versus GSPI, while the SAST control reduces rotor speed error by 37% and has a more platform pitch rate reduction, by 52%. For the rest of platform rotations and their rates, SAST and LQR controllers have similar performances. However, the variation of the blade pitch angle of LQR controller with the used tuning is much larger than SAST and GSPI controllers. It implies higher oscillations of the blade pitch angle and a higher request of the actuation system. Furthermore, notice that the controller gains of SAST can be adapted online whereas the LQR control needs large amount of parameters tuning around different operating points. Thus, SAST greatly reduces the tuning work load while getting globally the best performances of the three controllers.

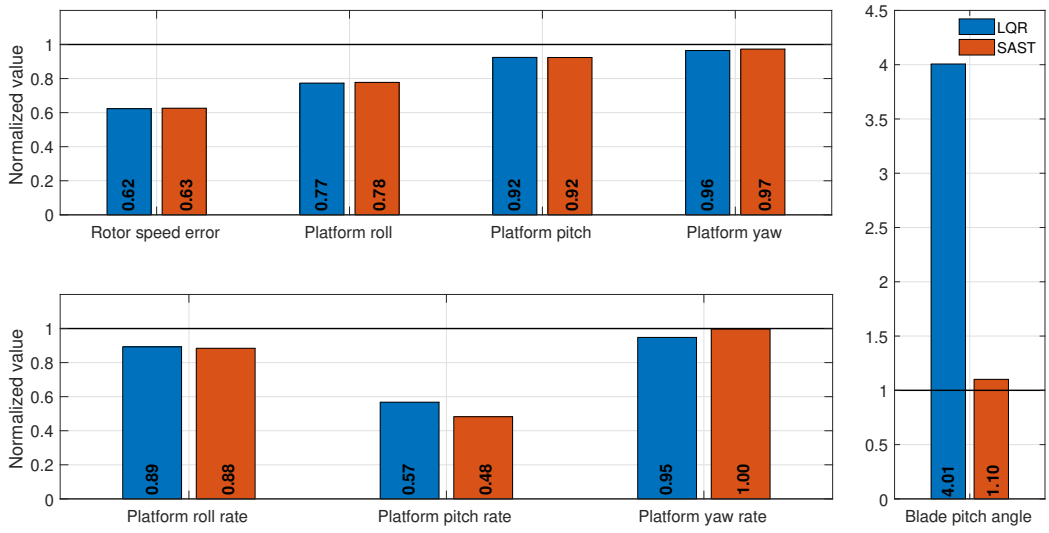

Figure 5.9 – **Scenario 2.** Normalized RMS (**left**)/VAR (**right**) values of performances indicators obtained by LQR (blue) and SAST (red) controllers.

Concerning fatigue load of the physical components of the experimental system, it is evaluated by

calculating the standard deviation (STD) of the tower base (TB) moments and the mooring line (ML) tensions. Such moments and tensions are measured by the sensors on the tower and on each of mooring lines. Similarly, the STD values are normalized versus GSPI as shown in Figure 5.10. SAST controller reduces the TB side-to-side and for-aft loads by 12% and 6% respectively with respect to GSPI; for the TB moment load and the tensions of each mooring line, all the three controllers have similar performances.

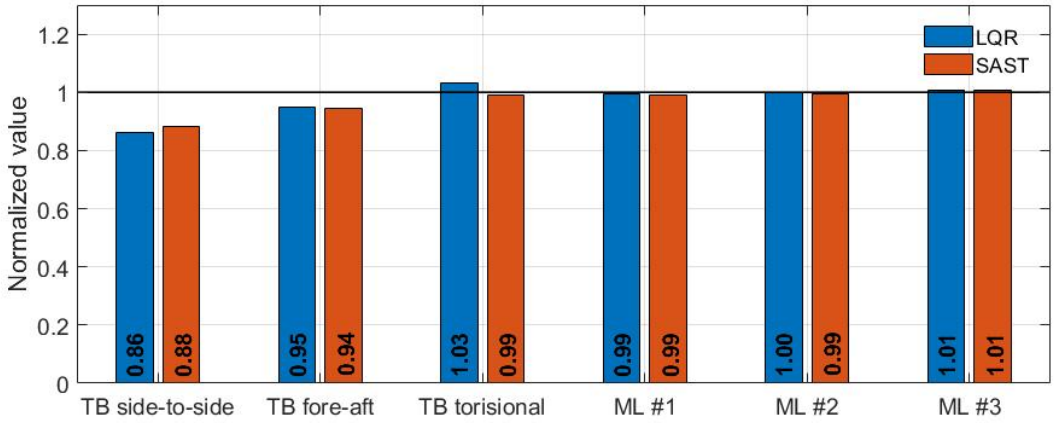

Figure 5.10 – **Scenario 2.** Normalized STD values of TB moments and ML tensions obtained by LQR (blue) and SAST (red) controllers.

Numerical replayed results

Recall that the rotor nacelle assembly is modeled by the FAST software and the aerodynamic forces are reproduced by the actuator. So, the moments of the blades cannot be physically measured. A numerical model of the experimental system has been built by FAST code. This numerical model is established at a full scale, from the measurements of the physical model. The experiments can be numerically replayed by FAST software. Such methodology provides a possibility to obtain the system variables that cannot be measured in the experiments as the blades moments. As detailed previously, the fatigue loads of the blade are crucial especially for the large scale FWT. The blade root (BR) moments of the three controllers are obtained by the FAST replayed simulations, as the damage equivalent loads (DEL).

Figure 5.11 displays the measured experimental data and the FAST replayed data. One can find that the FAST data is almost similar with the experimental data, expect a slight delay. By this way, FAST can accurately replay the experiments. To summarize, the numerical data can be used to evaluate the controller performances.

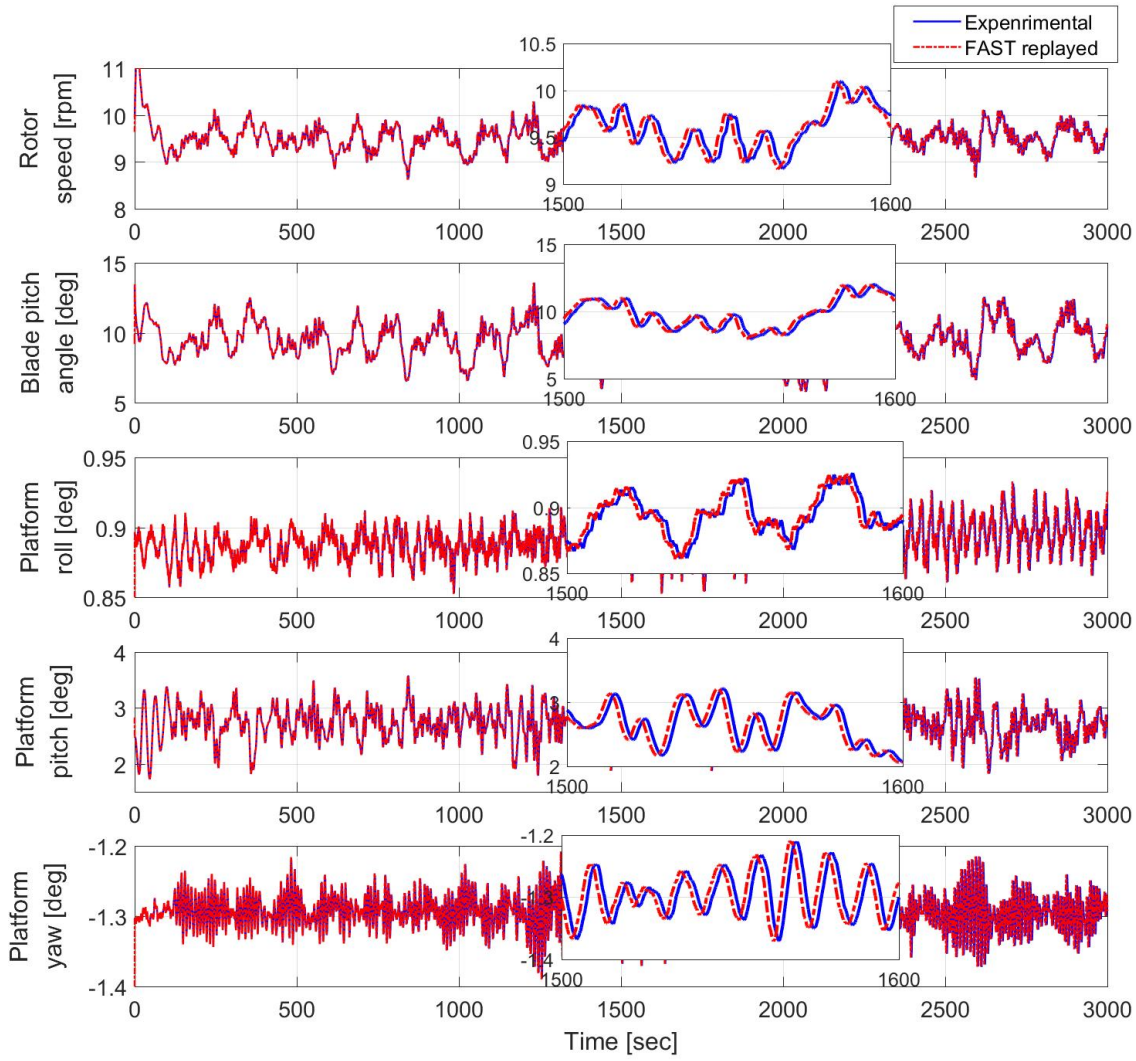

Figure 5.11 – **Scenario 2.** Measured experimental data (blue) and FAST replayed data (red) versus time (*sec*).

Figure 5.12 displayed the normalized DEL of BR moments obtained by the three controllers. Similarly, all the data are normalized such that, for GSPI controller, the quantity equals 1. Comparing with GSPI controller, SAST controller greatly reduces the DEL of BR flap-wise and pitch moments by 20% and 13% respectively whereas LQR tremendously increases those moments. Namely, SAST control could enlarge the lift-time of blades and thereby reduces maintenance cost and increases economic benefit.

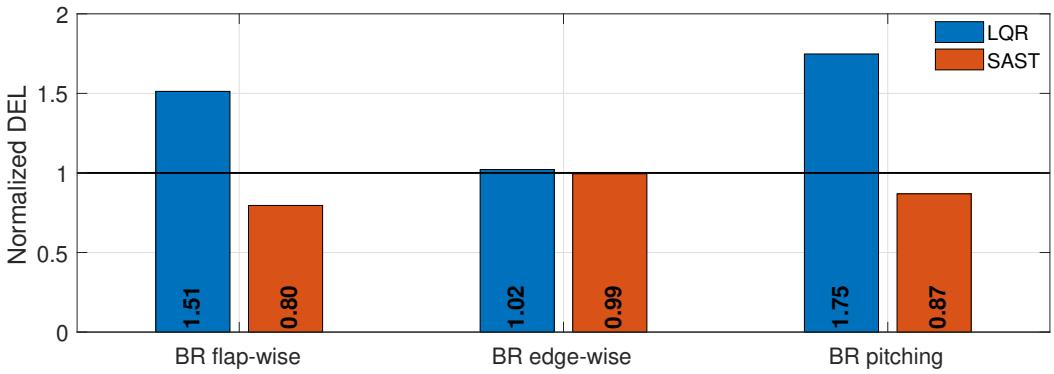

Figure 5.12 – **Scenario 2.** Normalized DEL values of BR loads obtained by LQR (blue) and SAST (red) controllers.

In summary, SAST and LQR controllers have greatly reduced the rotor speed error and platform pitch motion. However, the LQR control has high requirements for the blade pitch actuator. Concerning the fatigue load of the FWT components, the SAST control has best performances among the three controllers: it allows getting particularly much smaller DEL of blade root moments than LQR control. Moreover, such good performances of SAST are obtained thanks to a very reduced parameters tuning work load and system modeling information, making the implementation easier.

5.5 Conclusions

In this chapter, the proposed simplified adaptive super-twisting controller is applied to an experimental floating wind turbine set-up in the ECN wave tank. The experimental set-up has been designed by an hybrid method, and is composed by a reduced scale experimental set-up in the wave tank and a numerical one modeled by FAST. The SAST, LQR and GSPI controllers are briefly introduced and implemented on the scaled model.

Firstly, the SAST controller is checked under wind steps (among the whole Region III) and still water condition, that ensures the applicability of the controller. Then, all the three controllers are tested under stochastic wind and irregular wave conditions. Experimental results show that the

SAST controller greatly reduces the rotor speed error and platform pitch motion, allows to have small variations of blade pitch angle and structure fatigue loads. Given that the SAST controller needs a very reduced parameters tuning work load and system modeling information, it appears to be a very efficient and promising solution for the control of FWT.

CONCLUSION AND PERSPECTIVES

Conclusions

The work carried out in this thesis is focused on the robust nonlinear control of FWTs in Region III. Versus the onshore wind turbine that has a fixed bottom, FWT has extra motions introduced by the floating platform, especially the platform pitching. If this latter is not taken into consideration, it results large resonant platform motions, namely, negative damping. Therefore, the control objectives of FWTs in Region III are the regulation of the power at its rated value to protect the generator and the mechanical structure, the reduction of the platform pitch motion, ensuring the stability of the platform and the reduction of structure loads in order to extend the service life of the system. The motivations of this work are to design robust nonlinear controllers that can achieve these control objectives. Since the majority of the current controllers are designed based on linear approaches that require large effort of tuning effort, another motivation lies in design adaptive nonlinear controller laws that could largely reduce the tuning work load meanwhile ensure robustness versus uncertainties and perturbations (wind and wave variations, modeling errors, ...). At last, the controllers in this work require very limit knowledge of the system model and can be easily implemented in practice. The results of this thesis have been presented in five chapters.

Chapter 1 has described the modeling of a FWT system, simulation set-up and analysis of performances. Firstly, the coordinates system have been established. Physical models of power capture and drive train system are introduced. Then, a brief explanation of hydrodynamics of the floating structure is given. By a control design point of view, the linearized model of FWT is introduced and compared with the FAST nonlinear model. Finally, FAST software that is used in this work for the simulations of a 5 MW spar-buoy FWT is introduced, and performance indicators are defined.

In Chapter 2, adaptive high order sliding mode control is applied to the FWT based on the CBP control. The control objectives are the regulation of the rotor speed at its rated value (assuming that the generator torque at its rated value) and the reduction of the platform pitch motion. High order sliding model with different adaptation algorithms are used, including the adaptive super-twisting (ASTW) proposed by (Yuri Shtessel, Taleb, and Plestan 2012) and a recent developed homogeneity based controller with varying exponent parameter (HCVP) (Tahoumi, Plestan, et al. 2019). A novel simplified adaptive super-twisting (SAST) algorithm with very few tuning parameters (only 2 parameters are need to be tuned) has been proposed and applied to the FWT. All of those algo-

rithms are implemented to FWT in the FAST/SIMULINK environment and the performances are compared with the GSPI (J. Jonkman 2008a) control in different scenarios. Finally, the simulation results show that these adaptive algorithms allow to control the FWTs in Region III with very reduced parameters tuning and knowledge of system modeling, resulting in better performances versus standard GSPI. Moreover, the proposed SAST control has much less tuning parameters than the ASTW while keeping similar performances

In Chapter 3, a permanent magnet synchronous generator is supposed to equip the FWT. The control is not only acting on the aero/hydrodynamic part, but also considers the control of electrical part. The control objectives are turns into regulation of the power at its rated value, the reduction of the platform pitch motion, and the elimination of the ripple effect of the generator. Unlike the previous chapter (in which the generator torque was fixed at its rated value), the power regulation is achieved by the combination of torque control and rotor speed control. Both ASTW and SAST controllers are used in this chapter; the simulation results show the two adaptive controllers have better performances on power regulation, platform pitch reduction and have lower structure loads than the both GSPI controllers.

In Chapter 4, the IBP approach is combined with CBP control. Therefore, besides regulating the power and reducing the platform pitch motion, the controller proposed in this chapter takes the structural load reduction into consideration. The overall control scheme consists in two parts: the CBP control loop for the rotor speed regulation and platform pitch reduction, and the IBP control loop for the blade load reduction. The ASTW approach is applied in this chapter; simulation results show that the CBP and IBP based ASTW algorithm gives not only better performances on the power regulation and platform pitch motion reduction than CBP controllers, but also provides better performances on the blade load reduction.

In Chapter 5, the proposed SAST controller is applied to an experimental floating wind turbine set-up in the ECN wave tank. The experimental set-up has been designed by an hybrid method, and is composed by a reduced scale experimental set-up in the wave tank and a numerical part developed with FAST. During the experiments, SAST, LQR and GSPI controllers have been implemented on the set-up. Experimental results show that the SAST controller greatly reduces the rotor speed error and platform pitch motion. Furthermore, SAST controller allows to have small variations of blade pitch angle and structure fatigue loads. Given that the SAST controller needs very reduced parameters tuning work load and limited system modeling information, this control solution appears to be a very efficient and promising solution for the control of FWT.

Perspectives

Several points can be considered for further works of control of FWTs:

- Simulation and experimentation in numerous different scenarios, in order to qualify more precisely the performances of ASTW and SAST controllers.

- Design of nonlinear control of FWTs in Region II. The works done in this thesis have been focused on the control of FWTs in Region III. However, the control problem in Region II is not considered. Future work could design robust nonlinear controllers to deal with the FWT control in Region II (maximum point power tracking).

- In addition, the transition between Region II and III is also important for wind turbines to ensure a smoothness transition in order to improve the power generation. Then, for the FWT, the nonlinear controllers are also needed to be designed for this transition region.

- In this work, the stability of the proposed controllers for the FWT is not formally proved on the full DOFs of the FWT. Thus, it is absolutely necessary to propose a method to prove the stability of the controllers, and then to validate them. It is a key-step to go ahead towards a real implementation.

Bibliography

Abo-Khalil, Ahmed G et al. (2019), « Dynamic modeling of wind turbines based on estimated wind speed under turbulent conditions », *in*: *Energies* 12.*10*, p. 1907.

Arnal, Vincent (2020), « Modélisation expérimentale d'une éolienne flottante par une approche « software-in-the-loop » », PhD thesis, École Centrale de Nantes, Nantes, France.

Bagherieh, Omid and Ryozo Nagamune (2015), « Gain-scheduling control of a floating offshore wind turbine above rated wind speed », *in*: *Control Theory and Technology* 13.*2*, pp. 160–172.

Bak, Christian et al. (2013), « The DTU 10-MW reference wind turbine », *in*: *Danish Wind Power Research 2013*.

Bakka, Tore and Hamid Reza Karimi (2012), « Robust H_∞ dynamic output feedback control synthesis with pole placement constraints for offshore wind turbine systems », *in*: *Mathematical Problems in Engineering* 2012, DOI: 10.1155/2012/616507.

Bayati, Ilmas et al. (2017), « Scale model technology for floating offshore wind turbines », *in*: *IET Renewable Power Generation* 11.*9*, pp. 1120–1126.

Beltran, Brice (2010), « Contribution à la commande robuste des éoliennes à base de génératrices asynchrones double alimentation: du mode glissant classique au mode glissant d'ordre supérieur », PhD thesis, Université de Bretagne Occidentale, Brest, France.

Beltran, Brice, Tarek Ahmed-Ali, and Mohamed El Hachemi Benbouzid (2008), « High-order sliding-mode control of variable-speed wind turbines », *in*: *IEEE Transactions on Industrial electronics* 56.*9*, pp. 3314–3321.

Benelghali, Seifeddine, Mohamed El Hachemi Benbouzid, and Jean Frédéric Charpentier (2012), « Generator systems for marine current turbine applications: A comparative study », *in*: *IEEE Journal of Oceanic Engineering* 37.*3*, pp. 554–563.

Betti, Giulio et al. (2013), « Development of a control-oriented model of floating wind turbines », *in*: *IEEE Transactions on Control Systems Technology* 22.*1*, pp. 69–82.

Bianchi, Fernando D, Hernan De Battista, and Ricardo J Mantz (2006), *Wind turbine control systems: principles, modelling and gain scheduling design*, London, UK: Springer Science & Business Media.

Bir, Gunjit (2008), « Multi-blade coordinate transformation and its application to wind turbine analysis », *in*: *46th AIAA aerospace sciences meeting and exhibit*, Reno, Nevada, USA.

Bir, Gunjit S (2010), *User's guide to MBC3: Multi-blade coordinate transformation code for 3-bladed wind turbine*, tech. rep., National Renewable Energy Lab.(NREL), Golden, CO, USA.

Bossanyi, Ervin A (2000), « The design of closed loop controllers for wind turbines », *in*: *Wind energy* 3.*3*, pp. 149–163.

— (2003), « Individual blade pitch control for load reduction », *in*: *Wind Energy* 6.*2*, pp. 119–128.

Brown, David K (2006), *The way of a ship in the midst of the sea: the life and work of William Froude*, Penzance, UK: Periscope Publishing Ltd.

Burton, Tony, David Sharpe, and Nick Jenkins (2001), *Handbook of wind energy*, Chichester, UK: John Wiley & Sons.

Burton, Tony, David Sharpe, Nick Jenkins, and Ervin Bossanyi (2001), *Wind energy handbook*, New York, USA: Wiley.

Carrion, Juan E and Billie F Spencer Jr (2007), *Model-based strategies for real-time hybrid testing*, tech. rep., Newmark Structural Engineering Laboratory. University of Illinois at Urbana-Champaign, Champaign, USA.

Chen, Peng, Jiahao Chen, and Zhiqiang Hu (2020), « Review of Experimental-Numerical Methodologies and Challenges for Floating Offshore Wind Turbines », *in*: *Journal of Marine Science and Application* 19, pp. 339–361.

Chen, Z (2013), *An overview of power electronic converter technology for renewable energy systems*, in Electrical Drives for Direct Drive Renewable Energy Systems, Eds. M. Mueller and H. Polinder, Cambridge, UK: Woodhead, pp. 80–105.

Cheon, Jongmin et al. (2019), « Development of Hardware-in-the-Loop-Simulation Testbed for Pitch Control System Performance Test », *in*: *Energies* 12.*10*, p. 2031.

Cho, Seongpil (2020), « Model-based Fault Detection and Diagnosis of a Blade Pitch System in Floating Wind Turbines », PhD thesis, Norwegian University of Science and Technology, Trondheim, Norway.

Christiansen, Søren, Torben Knudsen, and Thomas Bak (2011), « Optimal control of a ballast-stabilized floating wind turbine », *in*: *IEEE international symposium on computer-aided control system design*, Denver, CO, USA.

— (2014), « Extended onshore control of a floating wind turbine with wave disturbance reduction », *in*: *Journal of Physics: Conference Series*, vol. 555, 1, IOP Publishing, p. 012018.

Cruz-Zavala, Emmanuel and Jaime Moreno (2016), « Lyapunov approach to higher-order sliding mode design », *in*: *Recent trends in sliding mode control*, ed. by Leonid Fridman, Jean-Pierre Barbot, and Franck Plestan, The Institution of Engineering and Technology, London, UK.

Cunha, A et al. (2014), « Reducing blade fatigue and damping platform motions of floating wind turbines using model predictive control », *in*: *International Conference on Structural Dynamics*, Porto, Portugal.

Fischer, Boris and Peter Loepelmann (2016), « Balancing rotor speed regulation and drive train loads of floating wind turbines », *in*: *Journal of Physics: Conference Series*, vol. 753, p. 052016.

G, Betti et al. (2012), « Modeling and control of a floating wind turbine with spar buoy platform », *in*: *IEEE International Energy Conference and Exhibition*, Florence, Italy.

Gerber, H and M Buhl Jr (2012), *MLife User's Guide*, tech. rep., National Renewable Energy Lab.(NREL), Golden, CO, USA.

Glumineau, Alain and Jesus De León-Morales (2015), *Sensorless AC Motor Control: Robust Advanced Design Techniques and Applications*, Berlin, Germany: Springer.

Guenoune, Ibrahim (2018), « Commandes non linéaires robustes de systèmes éoliens », PhD thesis, École Centrale de Nantes, Nantes, France.

Guenoune, Ibrahim et al. (2017), « Modeling and robust control of a twin wind turbines structure », *in*: *Control Engineering Practice* 69, pp. 23–35.

Gutierrez, S.V. et al. (2020), « A simplified version of adaptive supertwisting for control of floating wind turbine », *in*: *submitted to Control Engineering Practice, available at https://box.ec-nantes.fr:443/index.php/s/CSiTBJFD9bd6HK3*.

Gutierrez, Susana V et al. (2019), « A simplified version of adaptive super-twisting control », *in*: *International Journal of Robust and Nonlinear Control* 29.*16*, pp. 5704–5719.

GWEC (2019), *Global wind report*, tech. rep., Global Wind Energy Council.

— (2020), *Global offshore wind report*, tech. rep., Global Wind Energy Council.

Hall, Matthew and Andrew J Goupee (2018), « Validation of a hybrid modeling approach to floating wind turbine basin testing », *in*: *Wind Energy* 21.*6*, pp. 391–408.

Hall, Matthew, Andrew Goupee, and Jason Jonkman (2018), « Development of performance specifications for hybrid modeling of floating wind turbines in wave basin tests », *in*: *Journal of Ocean Engineering and Marine Energy* 4.*1*, pp. 1–23.

Hand, M Maureen and Mark J Balas (2000), « Systematic controller design methodology for variable-speed wind turbines », *in*: *Wind Engineering* 24.*3*, pp. 169–187.

Hansen, Morten Hartvig and Lars Christian Henriksen (2013), *Basic DTU wind energy controller*, Roskilde, Denmark: DTU Wind Energy.

Haque, Md E, Michael Negnevitsky, and Kashem M Muttaqi (2010), « A novel control strategy for a variable speed wind turbine with a permanent magnet synchronous generator », *in*: *IEEE Transactions on Industry Applications* 46.*1*, pp. 331–339.

Hara, Naoyuki et al. (2017), « Blade pitch control for floating wind turbines: Design and experiments using a scale model », *in*: *IEEE Conference on Control Technology and Applications*, Kohala Coast, Hawai'i, USA.

Heronemus, William E (1972), « Pollution-free energy from offshore winds », *in*: *8th Annual Conference and Exposition, Marine Technology Society*, Washington, DC, USA.

Homer, Jeffrey R and Ryozo Nagamune (2018), « Physics-based 3-D control-oriented modeling of floating wind turbines », *in*: *IEEE Transactions on Control Systems Technology* 26.*1*, pp. 14–26.

Huang, Can, Fangxing Li, and Zhiqiang Jin (2015), « Maximum power point tracking strategy for large-scale wind generation systems considering wind turbine dynamics », *in*: *IEEE Transactions on Industrial Electronics* 62.*4*, pp. 2530–2539.

IEA (2019a), *Global Energy CO2 Status Report 2019*, URL: `https://www.iea.org/reports/global-energy-co2-status-report-2019`.

— (2019b), *Offshore Wind Outlook 2019*, URL: `https://www.iea.org/reports/offshore-wind-outlook-2019`.

Jamieson, Peter and Garrad Hassan (2011), *Innovation in wind turbine design*, Hoboken, New Jersey, USA: Wiley Online Library.

Jelavić, Mate, Vlaho Petrović, and Nedjeljko Perić (2010), « Estimation based individual pitch control of wind turbine », *in*: *Automatika* 51.*2*, pp. 181–192.

Jonkman, Bonnie and Jason Jonkman (2016), *FAST v8. 16.00 a-bjj*, tech. rep., National Renewable Energy Lab.(NREL), Golden, CO, USA.

Jonkman, Jason (2008a), « Influence of control on the pitch damping of a floating wind turbine », *in*: *46th AIAA Aerospace Sciences Meeting and Exhibit*, Reno, Nevada, USA.

— (2008b), « Influence of control on the pitch damping of a floating wind turbine », *in*: *AIAA Aerospace Sciences Meeting and Exhibit*, Reno, USA.

— (2010), *Definition of the Floating System for Phase IV of OC3*, tech. rep., National Renewable Energy Lab.(NREL), Golden, CO, USA.

— (2019), URL: `https://wind.nrel.gov/forum/wind/viewtopic.php?f=4&t=1903&p=9924`.

Jonkman, Jason M, Marshall L Buhl Jr, et al. (2005), *FAST user's guide*, tech. rep., National Renewable Energy Lab.(NREL), Golden, CO, USA.

Jonkman, Jason Mark (2007), « Dynamics modeling and loads analysis of an offshore floating wind turbine », PhD thesis, National Renewable Energy Lab.(NREL), Golden, CO, USA.

Jonkman, Jason, Sandy Butterfield, et al. (2009), *Definition of a 5-MW reference wind turbine for offshore system development*, tech. rep., National Renewable Energy Lab.(NREL), Golden, CO, USA.

Jonkman, Jason and Paul Sclavounos (2006), « Development of fully coupled aeroelastic and hydrodynamic models for offshore wind turbines », *in*: *44th AIAA Aerospace Sciences Meeting and Exhibit*, Reno, Nevada, USA.

Karimirad, Madjid (2014), *Offshore energy structures: for wind power, wave energy and hybrid marine platforms*, New York, USA: Springer.

Keysan, Ozan, Alasdair S McDonald, and Markus Mueller (2011), « A direct drive permanent magnet generator design for a tidal current turbine (SeaGen) », *in*: *2011 IEEE International Electric Machines & Drives Conference*, Niagara Falls, ON, Canada.

Lackner, Matthew A (2009), « Controlling platform motions and reducing blade loads for floating wind turbines », *in*: *Wind Engineering* 33.*6*, pp. 541–553.

— (2013), « An investigation of variable power collective pitch control for load mitigation of floating offshore wind turbines », *in*: *Wind Energy* 16.*3*, pp. 435–444.

Larsen, Torben J and Tor D Hanson (2007), « A method to avoid negative damped low frequent tower vibrations for a floating, pitch controlled wind turbine », *in*: *Journal of Physics: Conference Series*, vol. 75, 1, IOP Publishing, p. 012073.

Lemmer, Frank, Steffen Raach, et al. (2015), « Prospects of linear model predictive control on a 10 MW floating wind turbine », *in*: *34th International Conference on Offshore Mechanics and Arctic Engineering*, Newfoundland, Canada.

Lemmer, Frank, David Schlipf, and Po Wen Cheng (2016), « Control design methods for floating wind turbines for optimal disturbance rejection », *in*: *Journal of Physics: Conference Series*, vol. 753, 9, pp. 1–14.

Levant, Arie (1993), « Sliding order and sliding accuracy in sliding mode control », *in*: *International journal of control* 58.*6*, pp. 1247–1263.

Li, Xianwei and Huijun Gao (2015), « Load Mitigation for a Floating Wind Turbine via Generalized H_∞ Structural Control », *in*: *IEEE transactions on industrial electronics* 63.*1*, pp. 332–342.

Ma, Yu et al. (2018), « Wave forecast and its application to the optimal control of offshore floating wind turbine for load mitigation », *in*: *Renewable Energy* 128, pp. 163–176.

Martin, HR et al. (2012), « Methodology for wind/wave basin testing of offshore floating wind turbines », *in*: *31st International Conference on Ocean, Offshore and Arctic Engineering*, Rio de Janeiro, Brazil.

McFadden, S and B Basu (2016), « Wind turbine gearbox design with drivetrain dynamic analysis », *in*: *Offshore Wind Farms*, Elsevier, pp. 137–158.

Menezes Novaes, Eduardo José, Alex Maurıcio Araújo, and Nadège Sophie Bouchonneau Da Silva (2018), « A review on wind turbine control and its associated methods », *in*: *Journal of Cleaner Production* 174, pp. 945–953.

Moreno, Jaime A (2009), « A linear framework for the robust stability analysis of a generalized super-twisting algorithm », *in*: *Int. Conf. Elec. Eng., Computing Sc. and Automatic Control*, Toluca, Mexico.

Musial, Walter, Sandy Butterfield, and Andrew Boone (2004), « Feasibility of floating platform systems for wind turbines », *in*: *42nd AIAA aerospace sciences meeting and exhibit*, Reno, Nevada, USA.

Muyeen, SM et al. (2007), « Comparative study on transient stability analysis of wind turbine generator system using different drive train models », *in*: *IET Renewable Power Generation* 1.*2*, pp. 131–141.

Namik, H. and K. Stol (2013), « A Review of Floating Wind Turbine Controllers », *in*: *Handbook of Wind Power Systems*, Berlin Heidelberg, Germany: Springer.

— (2014), « Individual Blade Pitch Control of a Spar-Buoy Floating Wind Turbine », *in*: *IEEE Transactions on Control Systems Technology* 22.*1*, pp. 214–223.

Namik, H and Karl Stol (2011), « Performance analysis of individual blade pitch control of offshore wind turbines on two floating platforms », *in*: *Mechatronics* 21.*4*, pp. 691–703.

Namik, Hazim (2012), « Individual blade pitch and disturbance accommodating control of floating offshore wind turbines », PhD thesis, The University of Auckland, Auckland, New Zealand.

Namik, Hazim and Karl Stol (2010), « Individual blade pitch control of floating offshore wind turbines », *in*: *Wind Energy* 13.*1*, pp. 74–85.

Namik, Hazim, Karl Stol, and Jason and Jonkman (2008), « State-space control of tower motion for deep water floating offshore wind turbines », *in*: *AIAA Aerospace Sciences Meeting and Exhibit*, Reno, USA.

Njiri, Jackson G and Dirk Söffker (2016), « State-of-the-art in wind turbine control: Trends and challenges », *in*: *Renewable and Sustainable Energy Reviews* 60, pp. 377–393.

Novak, Peter, Inge Jovik, and Bengt Schmidtbauer (1994), « Modeling and identification of drive-system dynamics in a variable-speed wind turbine », *in*: *IEEE International Conference on Control and Applications*, Glasgow, UK.

Obeid, Hussein et al. (2018), « Barrier function-based adaptive twisting controller », *in*: *15th International Workshop on Variable Structure Systems (VSS)*, Graz, Austria.

Odgaard, Peter Fogh, Jakob Stoustrup, and Michel Kinnaert (2013), « Fault-tolerant control of wind turbines: A benchmark model », *in*: *IEEE Transactions on Control Systems Technology* 21.*4*, pp. 1168–1182.

Olondriz Erdozain, Joannes (2019), « Advanced control for floating offshore wind turbines. », *in*:

Ossmann, Daniel, Julian Theis, and Peter Seiler (2017), « Load reduction on a clipper liberty wind turbine with linear parameter-varying individual blade pitch control », *in*: *Wind Energy* 20.*10*, pp. 1771–1786.

Park, Robert H (1929), « Two-reaction theory of synchronous machines generalized method of analysis-part I », *in*: *Transactions of the American Institute of Electrical Engineers* 48.*3*, pp. 716–727.

Passon, Patrik et al. (2007), « OC3—Benchmark exercise of aero-elastic offshore wind turbine codes », *in*: *Journal of Physics: Conference Series*, vol. 75, 1, p. 012071.

Perruquetti, Wilfrid and Jean-Pierre Barbot (2002), *Sliding mode control in engineering*, Boca Raton, FL, USA: CRC press.

Petrović, Vlaho, Mate Jelavić, and Mato Baotić (2015), « Advanced control algorithms for reduction of wind turbine structural loads », *in*: *Renewable Energy* 76, pp. 418–431.

Plestan, Franck et al. (2010), « New methodologies for adaptive sliding mode control », *in*: *Int. J. Control* 83.*9*, pp. 1907–1919.

Pöschke, Florian, Jens Fortmann, and Horst Schulte (2017), « Nonlinear wind turbine controller for variable power generation in full load region », *in*: *2017 American Control Conference*, Seattle, WA, USA, pp. 1395–1400.

Raach, Steffen et al. (2014), « Nonlinear model predictive control of floating wind turbines with individual pitch control », *in*: *American Control Conference*, Portland, USA.

Sandner, Frank et al. (2012), « Reduced nonlinear model of a spar-mounted floating wind turbine », *in*: *German Wind Energy Conference*, Bremen, Germany.

Sarkar, Saptarshi, Breiffni Fitzgerald, and Biswajit Basu (2020), « Individual Blade Pitch Control of Floating Offshore Wind Turbines for Load Mitigation and Power Regulation », *in*: *IEEE Transactions on Control Systems Technology*, pp. 1–11, DOI: 10.1109/TCST.2020.2975148.

Scheu, Matti et al. (2018), « Human exposure to motion during maintenance on floating offshore wind turbines », *in*: *Ocean Engineering* 165, pp. 293–306.

Schlipf, David, Lucy Y Pao, and Po Wen Cheng (2012), « Comparison of feedforward and model predictive control of wind turbines using LIDAR », *in*: *Conference on Decision and Control*, Hawaii, USA.

Schlipf, David, Frank Sandner, et al. (2013), « Nonlinear model predictive control of floating wind turbines », *in*: *23th International Offshore and Polar Engineering*, Anchorage, Alaska, USA.

Schlipf, David, Eric Simley, et al. (2015), « Collective Pitch Feedforward Control of Floating Wind Turbines Using Lidar », *in*: *Journal of Ocean and Wind Energy* 2.*4*, pp. 223–230.

Selvam, Kausihan et al. (2009), « Feedback–feedforward individual pitch control for wind turbine load reduction », *in*: *International Journal of Robust and Nonlinear Control* 19.*1*, pp. 72–91.

Shi, Yang et al. (2017), « Advanced control in marine mechatronic systems: A survey », *in*: *IEEE/ASME Transactions on Mechatronics* 22.*3*, pp. 1121–1131.

Shtessel, Y. et al. (2014), *Sliding Mode Control and Observation*, Springer, New York, USA.

Shtessel, Yuri, Christopher Edwards, et al. (2014), *Sliding mode control and observation*, New York, USA: Springer.

Shtessel, Yuri, Mohammed Taleb, and Franck Plestan (2012), « A novel adaptive-gain supertwisting sliding mode controller: Methodology and application », *in*: *Automatica* 48.*5*, pp. 759–769.

Si, Yulin (2015), « Structural Control Strategies for Load Reduction of Floating Wind Turbines », PhD thesis, University of Agder, Kristiansand, Norway.

Skaare, Bjørn et al. (2007), « Integrated dynamic analysis of floating offshore wind turbines », *in*: *European wind energy conference and exhibition*, Milan, Italy.

Soliman, Mahmoud A et al. (2018), « An adaptive fuzzy logic control strategy for performance enhancement of a grid-connected PMSG-based wind turbine », *in*: *IEEE Transactions on Industrial Informatics* 15.*6*, pp. 3163–3173.

Stol, Karl et al. (2009), « A comparison of multi-blade coordinate transformation and direct periodic techniques for wind turbine control design », *in*: *47th AIAA Aerospace Sciences Meeting including the New Horizons Forum and Aerospace Exposition*, Orlando, Florida, USA.

Suemoto, H, Naoyuki Hara, and Keiji Konishi (2017), « Model-based design of individual blade pitch and generator torque controllers for floating offshore wind turbines », *in*: *Asian Control Conference*, Gold Coast, Australia.

Tahoumi, Elias, Malek Ghanes, et al. (2018), « A new controller switching between linear and twisting algorithms », *in*: *American Control Conference*, Milwaukee, USA.

Tahoumi, Elias, Franck Plestan, et al. (2018a), « A Controller Switching between Twisting and Linear Algorithms for an Electropneumatic Actuator », *in*: *European Control Conference*, Limassol, Cyprus.

— (2018b), « Adaptive Exponent Parameter: a Robust Control Solution Balancing Between Linear and Twisting Controllers », *in*: *International Workshop on Variable Structure Systems*, Graz, Austria.

— (2019), « Robust and energy efficient control schemes based on higher order sliding mode », *in*: *European Control Conference*, Naples, Italy.

Thiery, Flavien, Naoyuki Hara, and Keiji Konishi (2015), « Model predictive control for floating offshore wind turbines with failure compensation using individual blade pitch control », *in*: *15th International Conference on Control, Automation and Systems*, Busan, Korea, pp. 1469–1473.

Tiwari, Ramji and N Ramesh Babu (2016), « Recent developments of control strategies for wind energy conversion system », *in*: *Renewable and Sustainable Energy Reviews* 66, pp. 268–285.

Tong, Wei (2010), *Wind power generation and wind turbine design*, Boston, USA: WIT press.

Tran, Thanh-Toan and Dong-Hyun Kim (2015), « The platform pitching motion of floating offshore wind turbine: A preliminary unsteady aerodynamic analysis », *in*: *Journal of Wind Engineering and Industrial Aerodynamics* 142, pp. 65–81.

Tran, Thanhtoan, Donghyun Kim, and Jinseop Song (2014), « Computational fluid dynamic analysis of a floating offshore wind turbine experiencing platform pitching motion », *in*: *Energies* 7.*8*, pp. 5011–5026.

Urbán, Albert M and Raúl Guanche (2019), « Wind turbine aerodynamics scale-modeling for floating offshore wind platform testing », *in*: *Journal of Wind Engineering and Industrial Aerodynamics* 186, pp. 49–57.

Utkin, Vadim (1977), « Variable structure systems with sliding modes », *in*: *IEEE Transactions on Automatic control* 22.*2*, pp. 212–222.

Utkin, Vadim I (1992), *Sliding modes in control and optimization*, Berlin Heidelberg, Germany: Springer.

Utkin, Vadim, Jürgen Guldner, and Jingxin Shi (1999), *Sliding mode control in electro-mechanical systems*, New York, USA: Taylor Francis.

Van Engelen, TG (2006), « Design model and load reduction assessment for multi-rotational mode individual pitch control (higher harmonics control) », *in*: *European wind energy conference*, Athens, Greece.

Vas, Peter (1998), *Sensorless vector and direct torque control*, Oxford Univ. Press.

Vittori, Felipe et al. (2018), « Hybrid scaled testing of a 5MW floating wind turbine using the SIL method compared with numerical models », *in*: *37th International Conference on Offshore Mechanics and Arctic Engineering*, Madrid, Spain.

Wakui, Tetsuya, Motoki Yoshimura, and Ryohei Yokoyama (2017), « Novel parameter settings for gain-scheduled feedback control of rotational speed in a floating offshore wind turbine–generator system », *in*: *Wind Engineering* 41.*1*, pp. 26–42.

Wang, Bin et al. (2014), « Experimental comparisons between implicit and explicit implementations of discrete-time sliding mode controllers: Towards chattering suppression in output and input signals », *in*: *International Workshop on Variable Structure Systems*, Nantes, France.

Wang, Na, Alan D Wright, and Kathryn E Johnson (2016), « Independent blade pitch controller design for a three-bladed turbine using disturbance accommodating control », *in*: *2016 American Control Conference*, Boston, MA, USA.

Ward, Dawn, Maurizio Collu, and Joy Sumner (2019), « Reducing Tower Fatigue through Blade Back Twist and Active Pitch-to-Stall Control Strategy for a Semi-Submersible Floating Offshore Wind Turbine », *in*: *Energies* 12.*10*, p. 1897.

Wind Energy International (2020), URL: `https://library.wwindea.org/global-statistics/`.

WindEurope (2017), *Floating offshore wind vision statement*, URL: `https://windeurope.org/wp-content/uploads/files/about-wind/reports/Floating-offshore-statement.pdf`.

— (2018), *Floating offshore wind energy: a policy blueprint for Europe*, URL: `https://windeurope.org/wp-content/uploads/files/policy/position-papers/Floating-offshore-wind-energy-a-policy-blueprint-for-Europe.pdf`.

Xiao, Shuai, Geng Yang, and Hua Geng (2013), « Individual pitch control design of wind turbines for load reduction using », *in*: *2013 IEEE ECCE Asia Downunder*, Melbourne, Australia.

Yenduri, Kalyan and Parthasarathi Sensarma (2016), « Maximum power point tracking of variable speed wind turbines with flexible shaft », *in*: *IEEE Transactions on sustainable energy* 7.*3*, pp. 956–965.

Yin, Ming et al. (2007), « Modeling of the wind turbine with a permanent magnet synchronous generator for integration », *in*: *2007 IEEE Power Engineering Society General Meeting*, Tampa, FL, USA.

Yu, W et al. (2018), « LIFES50+ D4. 2: Public definition of the two LIFES50+ 10 MW floater concepts », *in*: *University of Stuttgart*.

Titre : Une contribution à la commande non linéaire d'éoliennes flottantes

Mot clés : Éolienne flottante, commande adaptative, modes glissants d'ordre supérieur, contrôle du pas des pales

Résumé : Les éoliennes flottantes permettent d'utiliser l'abondante ressource en vent présente au large des côtes, et sont considérées comme une source prometteuse d'énergie renouvelable. Cependant, en raison de dynamiques supplémentaires introduites par la plateforme flottante (notamment, le tangage), le contrôle d'une éolienne flottante doit être pensée afin de stabiliser le système tout en optimisant la production d'énergie.

Ce travail est consacré à la commande non linéaire d'éoliennes flottantes dans la région III, la classe de lois de commande proposée nécessitant une connaissance réduite en terme de modélisation du système. Les objectifs de la commande sont de maintenir la puissance produite à sa valeur nominale, tout en limitant le mouvement de tangage de la plateforme et les charges de fatigue sur la structure. Tout d'abord, une loi de commande adaptative basée sur le super-twisting est proposée, avec notamment une loi d'adaptation du gain très simple. Ensuite, en utilisant un contrôle collectif du pas des pales, ce nouvel algorithme de commande est appliqué sur un modèle d'éolienne flottante non linéaire et comparé à d'autres commandes adaptatives par modes glissants d'ordre 2. Dans un second temps, une machine synchrone à aimants permanents est supposée être installée dans l'éolienne flottante. L'utilisation du pas des pales (approche collective) et du couple du générateur permet d'atteindre les objectifs, à partir de lois de commande basées sur une approche adaptative par mode de glissement d'ordre 2. Une troisième partie est consacrée à l'étude d'une commande individuelle du pas des pales combinée à une commande collective. Il est montré qu'un tel algorithme limite la charge de fatigue des pales. Enfin, des lois de commande sont appliquées et comparées sur un système expérimental d'éolienne flottante placé dans un bassin à houle. Les performances des lois de commande basées sur les modes glissants sont évaluées par rapport à des approches de commande linéaire telles qu'un PI à gain variable, et une commande linéaire quadratique.

Title: A contribution to the nonlinear control of floating wind turbines

Keywords: Floating wind turbine, adaptive control, high-order sliding mode, blade pitch control

Abstract: Floating wind turbines allow the use of the abundant wind resource in ocean area and are considered as a promising solution of renewable energy. However, due to the additional dynamics (especially the platform pitch motion) introduced by the floating platform, the control of a floating wind turbine must take such pitch motion into consideration to stabilize the system meanwhile optimizing the power output.

This work is dedicated to the nonlinear control of floating wind turbines in region III, this class of controllers requiring reduced knowledge of system modeling and parameter. The control objectives are to maintain the power output at its rated value, to reduce the platform pitch motion and to limit the fatigue load. Firstly, a simplified adaptive super-twisting is proposed. Then, by using collective blade pitch control, this algorithm and other adaptive high order sliding model algorithms are applied on a nonlinear floating wind turbine model. Secondly, a permanent magnet synchronous generator is supposed to be installed in the floating wind turbine. Both collective blade pitch control and generator torque control based on adaptive high-order sliding mode control are used to achieve the control objectives. Thirdly, individual blade pitch control combined with collective blade pitch control is employed. Such algorithm further reduces the fatigue load of blades. Finally, the proposed simplified adaptive super-twisting algorithm is validated on an experimental floating wind turbine set-up (with a spar-buoy platform) in a wave tank, and the control performances are evaluated versus linear control approaches such as gain-scheduled PI and linear–quadratic regulators.